Helicopter Rotor Lift Distributions for Minimum Induced Power Loss

by

Kyle Yi-Ling Yang

B.S. Cornell University (1991)

Submitted to the Department of Aeronautics and Astronautics
in partial fulfillment of the requirements
for the degree of

Master of Science

at the

MASSACHUSETTS INSTITUTE OF TECHNOLOGY

September, 1993

Author_____
Department of Aeronautics and Astronautics
August 23, 1993

Certified by_____
Professor Steven R. Hall
Department of Aeronautics and Astronautics
Thesis Supervisor

Accepted by_____
Professor Harold Y. Wachmann
Chairman, Departmental Graduate Committee

Helicopter Rotor Lift Distributions for Minimum Induced Power Loss

by

Kyle Yi-Ling Yang

Submitted to the Department of Aeronautics and Astronautics
on August 23, 1993, in partial fulfillment of the
requirements for the degree of
Master of Science

Abstract

A method is derived to generate the minimum induced loss lift distribution for a lightly loaded helicopter rotor in forward flight. Finding the optimal distribution requires the minimization of the induced power with respect to variations in the bound circulation, subject to the requirement that the rotor be in trim. The analysis examines the flow in the far wake of the rotor, and, as such, is shown to be an extension of the minimum induced loss theory known for propellers and fixed wings. The far wake minimization results in lift distributions that a real rotor could not achieve, because the lift is too high on the retreating blade side. The theory is therefore extended to include constraints on the maximum allowable local lift at any point on the rotor disk. The rotor theory yields a set of necessary conditions which are solved numerically. A finite element method is used to solve the necessary conditions, since the minimization derives from a variational principle. The extension to include the constraints on the maximum allowable local lift is done using augmented Lagrangians.

Results are presented which show that an optimal lift distribution, with constraints on the maximum local lift, requires between 11% and 16% less induced power than a typical rotor lift distribution. A static aeroelastic analysis is performed to assess the capability of a rotor to achieve the optimal lift distribution. The lift distribution of a typical rotor is augmented by multicyclic inputs to the swashplate and trailing-edge servoflaps distributed along the blades. It is shown that the augmented rotor should be able to achieve approximately a 4% reduction in induced power over a typical rotor.

Thesis Supervisor: Steven R. Hall, Sc. D.
Title: Associate Professor of Aeronautics and Astronautics

Acknowledgments

First and foremost, I would like to thank Professor Steven Hall for his insight and guidance. I would also like to thank Professor Mark Drela for introducing us to Munro's work on propellers. Prof. Drela provided the code to generate Goldstein's optimal propeller solution and took the time to answer all of my questions. Furthermore, it has been my pleasure to work with Professor Kenneth Hall, of Duke University. Prof. Hall saved us valuable time both by providing a finite element potential solver and by providing us with his expertise in fluid mechanics.

This project was sponsored by a grant from NASA, NAG1-1299, with Dr. John Berry, of the Aeroperformance Division of the US Army Aeroflightdynamics Directorate, serving as technical monitor. I would like to thank Dr. Berry for being a gracious host during our visits to the Langley Research Center.

I am grateful to the National Science Foundation for providing me with a Graduate Research Fellowship during my time at MIT.

Most calculations for this project were performed on the MIT Cray X-MP.

I would also like to thank the other members of my research group, Eric Prechtl, Matt Fox, and James Garcia, for their support during my tenure as a spinhead. Mr. Garcia very generously performed the C-60 computer runs needed to analyze servoflap effectiveness.

Finally, I should acknowledge those who make my time at MIT an enjoyable experience. I am truly lucky to have friends such as Steven Lee; Paul van Deventer; and my fellow transplants from the Hill: Sarah Stock and Emily Sun. Last, but not least, I am grateful for the never ending support of my parents.

Contents

List of Figures

List of Tables

Nomenclature

Listed below, in alphabetical order, are the variable names used throughout this document. The list is separated into Latin characters, Greek characters, and also a section for subscripts and superscripts.

Latin

a	Blade section lift curve slope
A	Rotor disk area, πR^2
A_j	Average wake surface area of elements around node j
$\boldsymbol{A}$	Diagonal matrix whose entries are A_j
B	Number of blades
$\boldsymbol{B}$	Matrix relating nodal potential values to the potential gradient inside an element
$\boldsymbol{B}_m$	Matrix relating global vector of nodal potential values to the potential gradient inside element m
c	Blade chord
$\mathcal{C}$	Scalar constant, $\rho B\Omega/(2\pi)$
C_a	Set of nodes previously in the constraint set and scheduled to remain in the set
C_b	Set of nodes being added to the constraint set
C_l	Sectional lift coefficient
C_P	Coefficient of power, $P/\rho A(\Omega R)^3$
C_T	Thrust coefficient, $T/\rho A(\Omega R)^2$
$\boldsymbol{D}$	Matrix relating harmonic control input to lift
$\boldsymbol{E}$	Matrix relating harmonic control input to bound circulation
$\boldsymbol{F}$	Rotor force vector
g	Scalar penalty weight
$\boldsymbol{G}$	Matrix relating nodal potential values to the circulation inside an element

$\boldsymbol{G}_m$	Matrix relating global vector of nodal potential values to the circulation inside element m
H	Aft in-plane rotor force
$\boldsymbol{H}$	Matrix relating nodal potential values to the potential inside an element
$\boldsymbol{H}_m$	Matrix relating global vector of nodal potential values to the potential inside element m
$\hat{\boldsymbol{i}}$, $\hat{\boldsymbol{j}}$, $\hat{\boldsymbol{k}}$	Unit vectors corresponding to the x, y, and z coordinate axes
$\boldsymbol{K}$	Finite element stiffness matrix
KE	Kinetic energy in wake
l	Lift on a blade section
$\boldsymbol{M}$	Vector of rotor moments
M_x	Rotor hub rolling moment
M_y	Rotor hub pitching moment
$\hat{\boldsymbol{n}}$	Unit vector normal to a surface
N	Number nodes in the finite element model
P_{i}	Induced Power
P_2	Penalty function for nodes in C_a
P_3	Penalty function for nodes in C_b
Q	Rotor shaft torque
r	Blade radial station
$\bar{r}$	Non-dimenional blade radial station, r/R
$\boldsymbol{r}$	Vector from hub center to blade station r
$\hat{\boldsymbol{r}}$	Unit vector along $\boldsymbol{r}$
$\bar{r}_{\mathrm{c}}$	Non-dimensional root cutout
R	Rotor radius
R_∞	Radius of finite element domain
$\boldsymbol{R}$	Right hand side vector in finite element calculations
$\mathcal{S}$	Surface of control volume $\mathcal{V}$
T	Rotor thrust

U_T	component of velocity incident to a blade in the direction tangent to the blade rotational velocity
U_R	component of velocity incident to a blade in the radial direction
U_P	component of velocity incident to a blade, perpendicular to the plane of the disk
$\boldsymbol{U}$	Velocity vector incident to a blade
$\boldsymbol{v}$	Induced velocity in the far wake
$\boldsymbol{V}$	Helicopter velocity vector
$\mathcal{V}$	Control volume
$\boldsymbol{w}$	Induced velocity at rotor disk
$\boldsymbol{W}$	Matrix of discrete influence coefficients, from circulation to wash at rotor
$\mathcal{W}$	Wake sheet surface
x	Coordinate axis, positive aft
y	Coordinate axis, positive to right
Y	Rotor in-plane side force
z	Coordinate axis, positive up

Greek

α	Airfoil angle of attack
α_r	Angle of tilt of rotor tip path plane into the direction of travel
β_j	Augmented lagrangian on node j
$\boldsymbol{\beta}$	Vector of Augmented lagrangians
γ	Circulation strength per unit length
Γ	Circulation
$\boldsymbol{\Gamma}$	Vector of nodal circulation values
δ	Variational operator
η	Angular control input schedule, function of time or azimuth
$\boldsymbol{\eta}$	Vector of input schedules for each control device

$\boldsymbol{\eta}_{\mathrm{h}}$	Vector of harmonic coefficients corresponding to each control degree of freedom
θ_{tw}	Linear blade twist
ϑ	Lagrange multiplier on bound circulation
κ	Rotor induced loss factor
λ	Vertical advance ratio, $-V_z/\Omega R$
μ	Forward advance ratio, $V_x/\Omega R$
ν_T	Thrust Lagrange multiplier
$\boldsymbol{\nu}$	Vector of force Lagrange multipliers
$\boldsymbol{\xi}$	Linear impulse
Π	Induced power functional
ϖ	Lagrange multiplier for flap and swashplate deflection
ρ	Density of air
σ	Rotor solidity, $Nc/\pi R$
$\hat{\boldsymbol{\tau}}$	Unit vector in wake translation direction
ϕ	Velocity potential
Φ_j	Velocity potential at a node labelled j
$\boldsymbol{\Phi}$	Vector of nodal velocity potential values
ψ	Azimuthal position on rotor disk
$\hat{\boldsymbol{\psi}}$	Unit vector in azimuthal direction
ω_x	Rolling moment Lagrange multiplier
ω_y	Pitching moment Lagrange multiplier
$\boldsymbol{\omega}$	Vector of moment Lagrange multipliers
Ω	Rotor rotational speed
$\boldsymbol{\Omega}$	Rotor rotation vector, $\Omega\hat{\boldsymbol{k}}$

Subscripts and Superscripts

$(\cdot)_{\mathrm{aug}}$	pertaining to augmented Lagrangians
$(\cdot)_{\mathrm{d}}$	discretized approximation of a continuous quantity

$(\cdot)_{\mathrm{i}}$	induced
$(\cdot)_{\mathrm{h}}$	pertaining to harmonic variables
$(\cdot)_m$	of the element labelled m
$(\cdot)_{\mathrm{max}}$	local maximum
$(\cdot)_{\mathrm{ref}}$	of the reference case
$(\cdot)_{\mathrm{req}}$	required value
$(\cdot)_T$	pertaining to thrust in the z direction
$(\cdot)^{\mathrm{u}}$	pertaining to the unconstrained optimization problem
$(\cdot)_x$	pertaining to rolling moment
$(\cdot)_y$	pertaining to pitching moment

Chapter 1

Introduction

The power required by the main rotor of a helicopter characterizes the craft's forward flight performance. For instance, a helicopter's maximum forward speed and its range at cruising speed are both limited by the efficiency of the rotor. The goal of this research is to determine methods of reducing the power required by a rotor in forward flight. For steady, level flight, the power required by the rotor can be subdivided into three components: profile power, parasite power, and induced power. The relative importance of each of these components to the total power varies with the flight speed. The profile power is the power required by the blades to overcome the viscous (*i.e.*, profile) drag on the blades. The parasite power accounts for the drag on the helicopter fuselage. Reducing these two components of the total power requires fairing the shape of the object which produced the drag, either the blade planform or the fuselage. The third power component, the induced power, is the power required to accelerate the airflow around the helicopter and produce thrust. As such, all lifting systems, even those idealized to be in a non-viscous flow, necessarily require induced power. The induced efficiency of the lifting system can be improved by tailoring the lift distribution. For instance, it is known that an elliptical lift distribution has the minimum induced drag for a fixed wing. The purpose of this thesis is to produce lift distributions for helicopter rotors that require the minimum induced power, for any given flight condition.

To produce a set of necessary conditions which characterize the optimal rotor

lift distribution, the rotor is assumed to operate in an inviscid flow. Also, the rotor is lightly loaded. A minimization is performed on the induced power, subject to constraints that the rotor remain in trim and that the maximum local lift on a blade be physically realizable. This leads to necessary conditions which are solved using a finite element model and augmented Lagrangians. The optimal rotor lift distributions are shown to offer considerable reductions in induced power compared to typical rotor lift distributions. For this reason, the optimal solution is used as a guide for the design of a rotor. Forward flight performance is analyzed for several designs of a smart rotor system, consisting of a blade augmented by trailing edge servoflaps and controlled by multicyclic inputs. It appears that such systems could achieve some of the characteristics of an optimal lift distribution, and, thus, offer considerable benefits.

The next section of this chapter surveys the current body of knowledge concerning helicopter and propeller performance improvement. Then, the general contributions of this research are explained and an overview of the chapters that follow is given.

1.1 Prior Work

1.1.1 Helicopters

Previous research has focused on overall helicopter performance rather than just the induced component of the total power. Nevertheless, performance research often implicitly includes the reduction of induced power as a goal. Two broad design philosophies characterize most previous research. The first philosophy dictates that one should optimize *standard* rotor technology for performance, since the technology is already proven. A second philosophy allows one to augment the rotor with additional *control authority*, which may or may not involve hardware changes to the system. Then, the augmented rotor system is optimized for performance enhancement.

A technique known as integrated multidisciplinary design optimization (MDO) [2] follows the first design philosophy. MDO makes use of sophisticated, comprehensive,

rotor simulations. The computer programs must account for the coupling between aerodynamic forces and the resulting dynamic responses. The optimization process minimizes a cost function consisting of horsepower, vibration, and hub loads, by adjusting design variables such as blade dimensions and shape. These parameters are constrained by physical limitations on the natural frequencies and inertias of the blade [7].

One example of the second philosophy is the use of multicyclic inputs to the swashplate. Today, higher harmonic control (HHC) is widely recognized as a potential means of reducing hub vibrations [44]. However, the possibility for its use in reducing power requirements has also been investigated. In the 1950s, Stewart [38] and Payne [26] used blade element analysis with uniform inflow to predict the authority of 2/rev and N/rev swashplate control, respectively. Stewart predicted that 2/rev tailoring of the lift distribution would increase a helicopter's forward advance ratio by as much as 0.1. Concerning performance, he predicted that any reduction in induced power would be offset by increased drag forces. Using computerized aerodynamic programs, Arcidiacono [3] predicted similar forward speed increases with 2 and 3/rev control but also took the significant step of attempting to identify the characteristics of the "ideal" lift distribution for reducing retreating blade stall. His proposed ideal consisted of an azimuthally-discontinuous lift distribution with a slightly negative lift on the advancing blade side to counter moment imbalances. This effectively required greater lift toward the fore and aft regions of the lift distribution.

In a more recent study, Shaw *et al.* [36] conducted wind tunnel tests which affirmed the performance benefits of 2/rev swashplate control. Using two degrees of control input, phased pitch up on the advancing and retreating blade areas, the power required was reduced by 6% at 135 knots and 4% at 160 knots on a CH-47D rotor.

The effect of 2/rev swashplate control on performance was further demonstrated in an analytical study conducted by Nguyen and Chopra [25]. Using comprehensive rotor simulation codes, they minimized a quadratic cost function based on shaft torque and pitch inputs. It was determined that two degrees of pitch input could reduce the torque by up to 3.8% for the rotor under study. Unlike Shaw's investigation, this

study found that the best results were achieved with nose down pitch inputs in the advancing and retreating blade regions and nose up pitch inputs in the fore and aft regions. The lift is effectively pushed to the fore and aft regions, as in the study by Arcidiacono.

The use of a HHC swashplate gives the system more control authority, but it does not involve any changes to the rotor blades. In contrast, a circulation control rotor (CCR) [43] requires the design of a wholly different rotor blade to gain greater control authority. A CCR blade is extremely stiff; air is blown from valves lining the trailing edge, which reduces separation and modifies the local circulation of the blade. Tests of a CCR demonstrated that the rotor can significantly reduce profile drag [16]. However, the mechanical complexity of these systems limits their utility.

Another example of improving performance by modifying standard rotor equipment is the controllable-twist rotor (CTR) [22]. In this system, blade root pitch was controlled by a conventional swashplate, but additional pitch control was obtained by placing a large, outboard, mechanically actuated flap near the blade tip. The servoflap was controlled by an independent, second swashplate, and the blades were given a low torsional rigidity to enhance twisting authority. The CTR design was multidisciplinary; a cost function based on factors such as total power, blade bending moments, blade angles of attack, and hub forces was minimized to determine the rotor's physical characteristics [42]. Wind tunnel tests of such a rotor and a conventional H-34 rotor suggested that the CTR could produce up to 20% more lift at some flight conditions by delaying blade stall, with negligible effects on the total power required [21]

Modern advances in materials such as piezoelectrics or shape memory allows have made research into *smart rotors* possible. Current investigations indicate that it should be possible to place piezoelectric-actuated, trailing-edge servoflaps on rotor blades [8]. The piezoelectric actuator is placed entirely inside the blade and the flap is faired, thus avoiding the drag due to a bulky, outboard flap. Also, this actuator allows for the implementation of modern control methods in an electronic control system. Spangler and Hall [37] demonstrated the feasibility of such a piezo servoflap

in scale-model wind tunnel tests. The piezo servoflaps could be distributed along a blade and, when coupled to a HHC control system, could produce both radial and azimuthal variations in the lift distribution. This would allow more accurate tailoring of the lift distribution than pure HHC swashplate control. Rather than serving as primary control devices, the piezo servoflaps would be used to augment the helicopter's normal cyclic and collective controls.

1.1.2 Propellers

Prior work concerning propellers is used extensively in this thesis and is discussed in detail in Chapter 3. Only a brief summary of significant works is mentioned here.

Unlike rotor research, propeller research has focused on investigating the induced drag. Early this century, theories developed by Betz [6], Prandtl, and Goldstein [12] predicted the minimum induced power for a lightly loaded propeller. Later, Munro [24] discussed extending this theory to rotors in forward flight. Other researchers have attempted to extend the Betz-Prandtl theories to heavily loaded propellers [40],[31],[45],[32].

1.2 Contributions of this Thesis

The main goal of this thesis is to find an aerodynamic optimal limit for the performance of a rotor in forward flight. The optimum is developed with as few blade characteristics being specified as possible. In fact, the the only parameters specified *a priori* are the number of blades, the root cutout size, maximum and minimum lift coefficients, and the flight conditions. The exact nature of the blades which produce the aerodynamic optimum is not directly sought. The final output of the optimization is a lift distribution which varies both azimuthally and radially.

This approach to performance improvement is fundamentally different from either a MDO philosophy or a control authority augmentation philosophy. MDO computer programs can greatly aid practical blade design, leading to more efficient blade profiles. However, the programs are inherently bound by their assumptions on existing,

available technology, rather than being bound by the fundamental fluid mechanics of the problem alone. Thus, a given set of design variables may lead to a conclusion about performance limitations which could be changed if different blade parameters where chosen as variables. Also, given the large number of blade parameters and the complexity of aerodynamic phenomena, it can be difficult to determine the factors which most strongly influence the induced power. A similar handicap limits the conclusions that can be drawn from research into rotor systems with additional control authority. Available performance improvement is again dictated by the choice of specific hardware. The potential benefits of any such system are further limited by the particular electro-mechanical and control system design used for the experimental setup.

The advantages of the approach presented here are twofold. First, eliminating the specification of blade aerodynamics allows the investigation to concentrate on the fluid mechanics of the problem. This provides more insight into physical limitations on helicopter performance, rather than technological limitations. Second, finding an aerodynamic optimum is a considerably simpler problem to solve than a complete MDO, since the design variables do not include blade parameters.

The utility of the optimal rotor solution is clear. The solution can be used to aid rotor design, because it prescribes what the lift distribution across the blade should be at any azimuthal position. Blade designs and rotor technology can then be selected based on their ability to achieve the optimal lift conditions. Of course, it is doubtful that any real rotor system could exactly achieve the optimal lift distribution. However, given that the solution is an optimum, an off-design lift distribution should still provide significant benefits.

1.3 Overview

The thesis is organized as follows: Chapter 2 provides an overview of helicopter performance analysis methods. Also presented is a performance metric which may be used to compare lift distributions.

Chapter 3 contains the theory underlying the aerodynamic optimum. The theory is an extension of the optimal condition for wings and propellers, which are presented in detail. The optimal conditions for a rotor are then derived based on energy principles and the assumption of light loading. Because of aerodynamic limitations, these conditions are shown to be inadequate for generating physically realizable lift distributions. Therefore, restrictions are placed on the maximum local lift that can be generated by a blade.

Chapter 4 describes the computer program, CORC, that was developed to calculate the optimal conditions for a rotor. The program contains an augmented Lagrangian optimization routine wrapped around a finite element solver. Also presented are some measures of computational cost.

Chapter 5 presents the results of several representative optimizations. The CORC routine is first validated by examining an axial flight case. Then, forward flight, optimal, lift distributions are compared to the lift distribution of a typical helicopter. The induced power is computed for each distribution, allowing quantitative comparisons. The effects of changing the number of blades and varying the maximum local lift coefficient are investigated.

Chapter 6 offers a preliminary analysis of how a rotor could achieve the optimal rotor conditions. Specifically, the use of a rotor augmented by faired servoflaps is investigated.

Chapter 7 presents the conclusions of this thesis and recommendations for future work.

Chapter 2

Standard Analysis Methods

Determining the induced power losses in a helicopter is not experimentally possible, because the induced power component cannot be separated from the other components that form the total rotor shaft power. Thus, several methods have been developed to estimate the induced power. For a given thrust, lift distributions which require less power are more efficient. The analysis tools presented here will allow this efficiency to be quantified.

Induced power losses are fundamentally a result of downwash at the rotor disk. At each blade section the downwash changes the local effective angle of attack, causing a portion of the force generated by the blade to be directed perpendicularly to the desired direction of lift. The perpendicular portion of the force is induced drag, and it causes induced power losses.

Before further discussing the calculation of the induced power, a section of this chapter is devoted to helicopter terminology. Then, three methods for analyzing a rotor's induced power are presented in order of increasing complexity. They are: momentum analysis, spanwise loading analysis, and near wake analysis. The last method, near wake analysis, generally relies on a downwash model from a vortex lattice code. This is the subject of the last section in the chapter. It will be shown that none of the standard methods for analyzing the induced power can be extended to yield an optimal rotor lift distribution.

2.1 Terminology

Standard helicopter vocabulary and symbology often do not correspond to the analogous terms usually associated with fixed wing aircraft. Also, most terms such as velocity are normalized and nondimensionalized, so they deserve attention. The important variables to define are a rotor's orientation, geometry, and motion.

A Cartesian coordinate system is attached to the center of the rotor hub, *i.e.*, the rotor's axis. The z coordinate axis points upward. The x and y axes lie in the plane of the rotor, with x pointing rearward and y to the right.

Blade azimuthal positions, as viewed from above, are measured by angular position, ψ, from the x axis; $\psi = 0°$ points rearward and $\psi = 90°$ points to the right, etc. American, single-rotor helicopters generally have rotors turning counter-clockwise, with angular velocity denoted Ω. The region from $\psi = 0°$ to $\psi = 180°$ is called the advancing side, while $\psi = 180°$ to $\psi = 360°$ is called the retreating side. The rotor position can also be described in terms of quadrants. The first quadrant denotes the blade positions between $\psi = 0°$ and $\psi = 90°$; the second denotes blade positions from $\psi = 90°$ and $\psi = 180°$, etc.

The blade's radius is R. Radial position along a blade, r, can be normalized as $\bar{r} = r/R$. Thus, $\bar{r}$ varies from $\bar{r} = 0$ at the hub to $\bar{r} = 1$ at the blade tip and $\bar{r} > 1$ for points beyond the rotor blades. The solidity, σ, is the ratio of total blade area (for all blades) to the area of the unit disk, $A = \pi R^2$.

The velocity of the rotor (*i.e.*, the helicopter) is measured from the frame of a viewer sitting at the rotor hub, or, equivalently, in the helicopter cabin. In steady, level, forward flight, the velocity has a rearward component, V_x. It also has a downward component, V_z, because the flow passing through the rotor is pushed downwards and because the rotor disk is tilted forward to produce thrust that will overcome the drag. These velocities can be nondimensionalized by the rotor tip speed. The forward advance ratio is defined as $\mu = V_x/\Omega R$, and the vertical advance ratio is defined as $\lambda = -V_z/\Omega R$. Note that these velocities refer to the motion of the helicopter, and not to the local velocities seen by a blade section, which will be examined in Section 2.4.

2.2 Momentum Analysis

The simplest method for determining the induced power is momentum theory. Its simplicity comes from the assumption that the induced flow at the rotor disk has a uniform profile. In determining the rotor's thrust and power, no attempt is made to determine details of the lift distribution, making this analysis unsuitable for optimization purposes.

Momentum theory predicts that far upstream from the rotor, the velocity is purely horizontal. By the time it reaches the rotor disk, the flow has attained a downward velocity component of w. A jump in pressure at the rotor disk delivers an impulse in the z direction to the flow. Far downstream from the rotor, the total pressure is assumed to return to its original upstream value. Bernoulli's theorem and conservation of mass show that this accelerates the fluid to an eventual downstream speed of $2w$. The thrust is equal to the rate of increase of the momentum in the fluid, so

$$T = 2\dot{m}w\,, \tag{2.1}$$

where w is the induced velocity at the rotor disk, and $\dot{m}$ is the mass flow rate. The induced power is equal to the force acting on the fluid times the velocity of the fluid, so that

$$P_{\mathrm{i}} = Tw\,. \tag{2.2}$$

Alternatively, for a disk in edgewise flight,

$$P_{\mathrm{i}} = D_{\mathrm{i}}V_x\,, \tag{2.3}$$

where D_{i} is the induced drag, and V_x is the helicopter's forward flight speed. A convenient expression for the mass flow rate, originally proposed by Glauert [9] is

$$\dot{m} = \rho A\sqrt{V_x^2 + w^2}\,, \tag{2.4}$$

in which ρ is the air density and A is the disk area. The flow that would produce this

mass flux is fictitious. The expression's utility comes from the fact that it reduces to more familiar forms at either end of the flight spectrum. At hover, the expression agrees with the momentum theory prediction for the mass flux through a propeller. Meanwhile, at typical helicopter forward flight speeds, V_x is much greater than w so the downwash term can be neglected. Then, the expression for the induced power can be reduced to the formula for the induced power of a minimum induced loss, fixed wing aircraft. At intermediate speeds, the formula has been shown to give acceptable results [35, Chapter 5].

Examining the high speed limit, Equations (2.1)–(2.4) can be combined to eliminate the induced velocity, so that

$$P_i = \frac{T^2}{2\rho A V_x} . \tag{2.5}$$

Furthermore, the induced power can be nondimensionalized, so that

$$\frac{C_P}{{C_T}^2} = \frac{1}{2\mu} , \tag{2.6}$$

where $C_P = P_i/(\rho A(\Omega R)^3)$ is the coefficient of power, and $C_T = T/(\rho A(\Omega R)^2)$ is the coefficient of thrust. Because Equation (2.6) represents the high speed limiting case, it cannot be applied when μ approaches zero. Also, the equation underpredicts the power required for a given level of thrust, but for speeds above $\mu = 0.1$, it gives reasonable estimates [15, Section 4-1].

Determining how much a rotor exceeds the value predicted by Equation (2.6) is beyond the capability of momentum theory. However, an induced loss factor, κ, can defined for this high speed limit, so that

$$\frac{C_P}{{C_T}^2} = \kappa \frac{1}{2\mu} . \tag{2.7}$$

For all real rotors, the loss factor must be greater than unity. Estimates for κ can be made by using a spanwise loading analysis or by making an exact calculation of the induced power.

2.3 Spanwise Loading Analysis

To estimate a rotor's induced loss factor, a more refined analysis can be made by examining the spanwise loading distribution. This is the method in which the induced drag for wings of arbitrary planform are compared to an elliptical planform wing. For a fixed wings, the spanwise elliptical loading represents the distribution of minimum induced loss [18, Section 6.6].

Integrating the lift distribution across the disk, in the flight path direction, yields the lift as a function of span location, $l = l(y)$, as shown in Figure 2-1. The distribution reaches a higher peak on the advancing blade side because of the higher dynamic pressure in that region. To counteract the rolling moment caused by the peak on the advancing side, the blade tips must carry a relatively heavy load on the retreating side.

The typical span loading distribution in Figure 2-1 can be compared to an elliptical lift distribution [11] by transforming it using

$$\theta \equiv \cos^{-1}(y/R)\,, \tag{2.8}$$

for a blade of radius R. This changes the spanwise loading distribution from $l(y)$ to $l(\theta)$. In particular, the *elliptical* distribution is converted to a half sine wave,

$$l_{\rm el}(\theta) = a_1 \sin\theta\,. \tag{2.9}$$

An arbitrary distribution has the series expansion

$$l(\theta) = \sum_{n=1}^{\infty} a_n \sin n\theta\,. \tag{2.10}$$

where a_n are the Fourier coefficients. The first coefficient, a_1, is proportional to the lift, and the second coefficient, a_2, is proportional to the rolling moment. For the elliptical planform, the total wing drag coefficient is proportional to the square of the

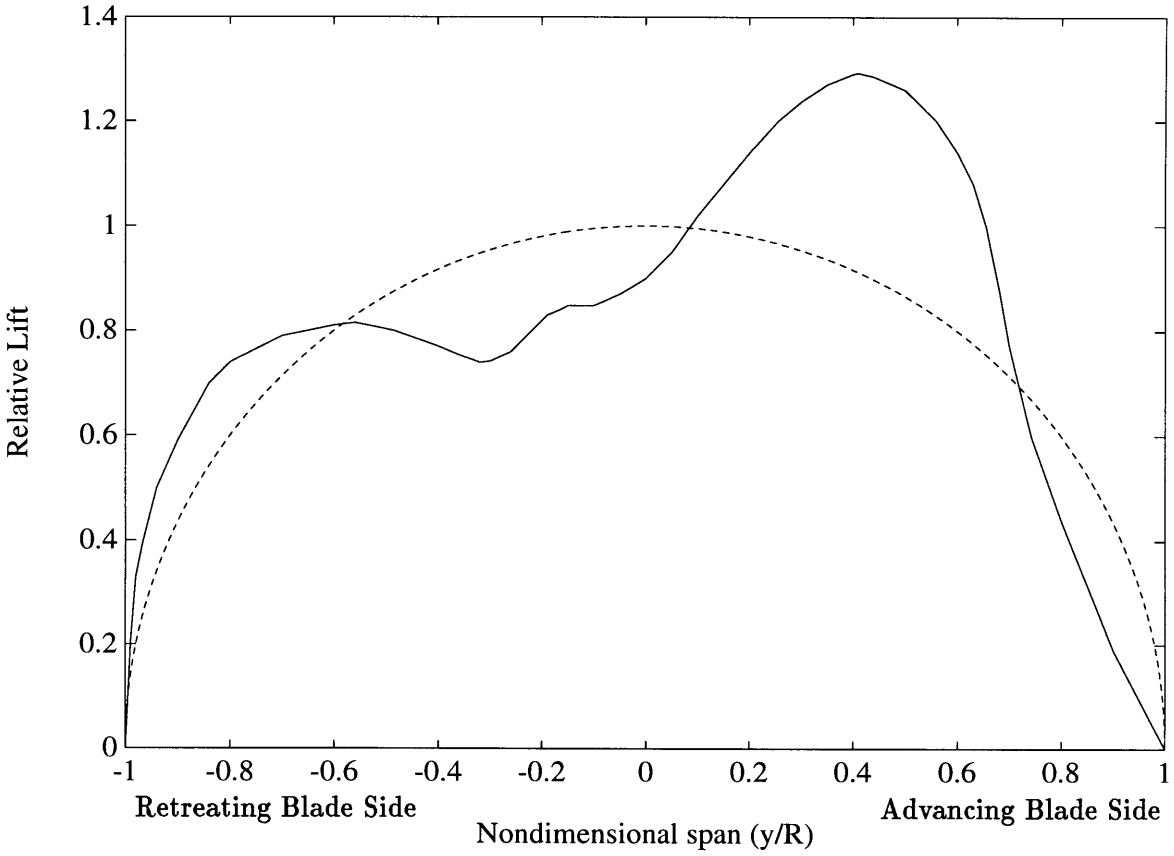

Figure 2-1: Spanwise loading of a typical rotor compared to an elliptical distribution. Flight conditions: $C_T/\sigma = 0.08; \mu = 0.25$; and rotor disk tilt angle, $\alpha_r = -12°$. The loss factor, κ, in this case is equal to 1.30. Adapted from Prouty [30].

total wing lift coefficient,

$$(C_{D_i})_{el} = \frac{C_{L_{el}}^2}{\pi \mathcal{AR}}, \tag{2.11}$$

where $\mathcal{AR}$ is the wing's aspect ratio. The drag of the arbitrary distribution in Equation (2.10) can also be computed. It can be shown that orthogonality of the trigonometric functions causes the wing drag coefficient to be proportional to the sum of the squares of the fourier coefficients, nA_n^2. Then, the ratio of the drag of an arbitrary loading to the ideal drag is

$$\kappa = \sum_{n=1}^{\infty} \frac{n a_n^2}{a_1^2}. \tag{2.12}$$

Recalling Equation (2.3) from momentum theory, Prouty [30] recognized that this

ratio is an estimate for the high speed, induced loss factor, κ, in Equation (2.7). It should be noted that κ is often written in terms of its reciprocal, $e = 1/\kappa$, the Oswald span loading efficiency.

Span loading analysis yields only an approximation for κ, because the integration operation does not account for the fore-aft position of variations in the flow. The point by point effects of downwash and lift on the power are ignored, so this analysis still neglects swirl losses and shed vorticity in the wake. Since the analysis only provides information on the optimal spanwise variation in lift, it cannot be used to optimize the full lift distribution over the rotor disk.

2.4 Near Wake Analysis

Analysis of a rotor's induced power requirements is most accurate if variations in the flow are taken into account. Momentum theory assumes that the flow is uniform, and spanwise loading only accounts for side to side variations. To fully capture the detail in the lift and wash distributions, the forces and wash at every location on the blades, at all azimuthal positions, must be examined, since these are the locations of the physical origin of induced power losses. This form of analysis is generally termed blade element analysis. However, the emphasis here is on the flowfield and the power calculation rather than on the blades and lift calculations, therefore, no blade flapping dynamics are included. Near wake analysis takes its name from the fact that the flow is sought at the rotor disk, in contrast to the far wake analysis, to be presented in Chapter 3, which examines the flow far away from the rotor.

For steady forward flight, the velocity at a blade section is derived from geometry. The velocity component in the plane of the rotor disk, in the tangent direction, is

$$U_T = V_x \sin\psi + \Omega r = \mu\Omega R \sin\psi + \Omega r \,, \tag{2.13}$$

and the radial component is

$$U_R = V_x \cos\psi = \mu\Omega R \cos\psi \,. \tag{2.14}$$

Lastly, the component perpendicular to the plane of the blades is

$$U_P = V_z = -\lambda \Omega R \,. \tag{2.15}$$

In vector form, the velocity at the blade can be written as

$$\begin{aligned} \boldsymbol{U} &= -U_T \hat{\boldsymbol{\psi}} + U_R \hat{\boldsymbol{r}} + U_P \hat{\boldsymbol{k}} && (2.16) \\ &= \left[(\mu R + r \sin\psi)\hat{\boldsymbol{\imath}} - (r \cos\psi)\hat{\boldsymbol{\jmath}} - \lambda R \hat{\boldsymbol{k}} \right] \Omega \,. && (2.17) \end{aligned}$$

Aerodynamic forces on a blade are calculated from the bound circulation, using the Kutta-Joukowski Theorem. The instantaneous force per unit span at a particular blade location is

$$\rho \boldsymbol{U}(r,\psi) \times \Gamma(r,\psi)\, \hat{\boldsymbol{r}} \,,$$

for air density ρ and bound circulation $\Gamma(r,\psi)$. To calculate the average force on the blade, the force per unit span is integrated along the blade; this quantity is then time averaged over each azimuthal position. Multiplying by the number of blades yields the total force on the rotor,

$$\begin{aligned} \boldsymbol{F} &= \frac{B}{2\pi} \int_0^{2\pi} \int_0^R \rho \boldsymbol{U} \times \Gamma \hat{\boldsymbol{r}} \, dr \, d\psi && (2.18) \\ &= H\hat{\boldsymbol{\imath}} + Y\hat{\boldsymbol{\jmath}} + T\hat{\boldsymbol{k}} \,. \end{aligned}$$

Normally, the largest component of this force is the thrust,

$$\begin{aligned} T &= \frac{B}{2\pi} \int_0^{2\pi} \int_0^R \rho \Gamma \, U_T \, dr \, d\psi \\ &= \frac{B}{2\pi} \int_0^{2\pi} \int_0^R \rho \Gamma \left(\mu \Omega R \, \sin\psi + \Omega r \right) dr \, d\psi \,. && (2.19) \end{aligned}$$

The other components, the net aft force and net side force, are

$$\begin{aligned} H &= \frac{B}{2\pi} \int_0^{2\pi} \int_0^R \rho \Gamma \, U_P \, \sin\psi \, dr \, d\psi \\ &= \frac{B}{2\pi} \int_0^{2\pi} \int_0^R \rho \Gamma \, \lambda \Omega R \, \sin\psi \, dr \, d\psi && (2.20) \end{aligned}$$

and

$$\begin{aligned} Y &= \frac{B}{2\pi}\int_0^{2\pi}\int_0^R \rho\Gamma\, U_P\, \cos\psi\, dr\, d\psi \\ &= \frac{B}{2\pi}\int_0^{2\pi}\int_0^R \rho\Gamma\, \lambda\Omega R\, \cos\psi\, dr\, d\psi\,. \end{aligned} \tag{2.21}$$

Similarly, the net moment on the helicopter due to aerodynamic forces is

$$\begin{aligned} \boldsymbol{M} &= \frac{B}{2\pi}\int_0^{2\pi}\int_0^R \rho\boldsymbol{r}\times(\boldsymbol{U}\times\Gamma\hat{\boldsymbol{r}})\, dr\, d\psi \\ &= M_x\hat{\boldsymbol{i}} + M_y\hat{\boldsymbol{j}} + Q\hat{\boldsymbol{k}}\,. \end{aligned} \tag{2.22}$$

The rolling and pitching components are seen to be

$$\begin{aligned} M_x &= \frac{B}{2\pi}\int_0^{2\pi}\int_0^R \rho\Gamma U_T\, r\sin\psi\, dr\, d\psi \\ &= \frac{B}{2\pi}\int_0^{2\pi}\int_0^R \rho\Gamma(\mu\Omega R\, \sin\psi + \Omega r)r\, \sin\psi\, dr\, d\psi \end{aligned} \tag{2.23}$$

and

$$\begin{aligned} M_y &= \frac{B}{2\pi}\int_0^{2\pi}\int_0^R \rho\Gamma U_T\, r\cos\psi\, dr\, d\psi \\ &= \frac{B}{2\pi}\int_0^{2\pi}\int_0^R \rho\Gamma(\mu\Omega R\, \sin\psi + \Omega r)r\, \cos\psi\, dr\, d\psi\,. \end{aligned} \tag{2.24}$$

The last component, the rotor shaft torque, is

$$\begin{aligned} Q &= -\frac{B}{2\pi}\int_0^{2\pi}\int_0^R \rho\Gamma U_P\, r\, dr\, d\psi \\ &= -\frac{B}{2\pi}\int_0^{2\pi}\int_0^R \rho\Gamma\lambda\Omega R r\, dr\, d\psi\,. \end{aligned} \tag{2.25}$$

Power calculations in near wake theory follow the methodology used for the calculation of the forces and moments. The incremental induced power required at each blade location can be computed as the product of the incremental lift with the induced wash at that location. Time averaging, using the formula for the lift per unit

span, and accounting for the number of blades yields

$$P_i = -\frac{B}{2\pi}\int_0^{2\pi}\int_0^R \rho\, \boldsymbol{w}\cdot(\boldsymbol{U}\times\Gamma\hat{\boldsymbol{r}})\, dr\, d\psi\,. \tag{2.26}$$

Unlike the spanwise loading calculation, this power calculation is not an approximation. It evaluates the particular quantities which physically cause the induced power: lift and downwash. The calculation fully accounts for their variation with respect to one another and their variation with position. In doing so, all complex phenomena, such as tip losses and shed vorticity, have inherently been taken into account.

Equation (2.26) can be used at all operating conditions, from hover to high speed flight. At the high speed limit, the equation can be used to calculate a coefficient of power and thus the induced loss factor of Equation (2.7). Of course, for accuracy, the calculation requires detailed knowledge of both the circulation and the wash distributions. In practice, if a circulation history is known, then a wash distribution can be predicted using a vortex lattice method or other similar computational techniques. In an experimental setting, the lift and, hence, the circulation, can be obtained with pressure sensors mounted on the blades. The induced velocity or the wake geometry can be measured using smoke trails, laser velicometry, or other flow visualization techniques.

2.5 Vortex Lattice Analysis

To calculate the induced power using Equation (2.26), the downwash at the rotor disk must be known. Unlike the assumption made in momentum theory, a real downwash distribution varies significantly over the rotor disk, with large velocities occurring at the rotor tips. The downwash has its origin in the wake of the rotor. As a rotor blades travels, it deposits a continuous sheet of vorticity, the wake sheet, which is a distribution of infinitesimal strength horseshoe vortices. The vortex sheet induces a flow at nearby points and, in particular, at the rotor disk.

In the absence of experimental data on rotor flowfields, computational routines

have been developed to calculate the flow from an assumed circulation history. The most common of these methods is the vortex lattice type, which models the rotor wake as a discrete mesh of vortex filaments. The vortex lines emanate from the blades, in both the perpendicular and radial directions, and convect down, away from the rotor disk. Each vortex filament induces a flow around it, and the total induced velocity at the rotor disk, summed from all of the filaments, is the desired downwash. According to the Biot-Savart law [18, page 48], an infinitesimal vortex segment, with strength Γ, oriented along $\boldsymbol{ds}$ induces a velocity field

$$\boldsymbol{dv} = \Gamma \frac{\boldsymbol{ds} \times \boldsymbol{P}}{4\pi |\boldsymbol{P}|^3} , \tag{2.27}$$

where $\boldsymbol{P}$ is a position vector from the vortex segment to the point where the increment in velocity, $\boldsymbol{dv}$, is evaluated.

In general, then, the induced velocity will be a function of the entire circulation history, which could be time varying. However, in steady flight, the circulation can be assumed to be periodic in time. Then, using a wake which is discretized into N horseshoe vortices, the downwash calculated at N control points on the rotor disk is a linear function of the circulation over the rotor disk

$$\boldsymbol{w} = \boldsymbol{W}\boldsymbol{\Gamma} , \tag{2.28}$$

where $\boldsymbol{w}$, and $\boldsymbol{\Gamma}$ are $N \times 1$ vectors, and $\boldsymbol{W}$ is an $N \times N$ matrix of influence coefficients calculated from the Biot-Savart law.

The accuracy of the method depends on the geometry chosen to represent the wake. The first successful vortex lattice analyses used a rigid wake, in which the vortex segments were fixed in space and their location specified, using momentum theory, prior to the velocity calculations [28]. Since then, more sophisticated analyses have been developed using a free wake, in which the filaments convect due to the induced velocity field in addition to the momentum contribution [5].

Furthermore, a fundamental problem arises because the wake has been approximated as a discrete set of finite strength vortex lines. The wake most closely repre-

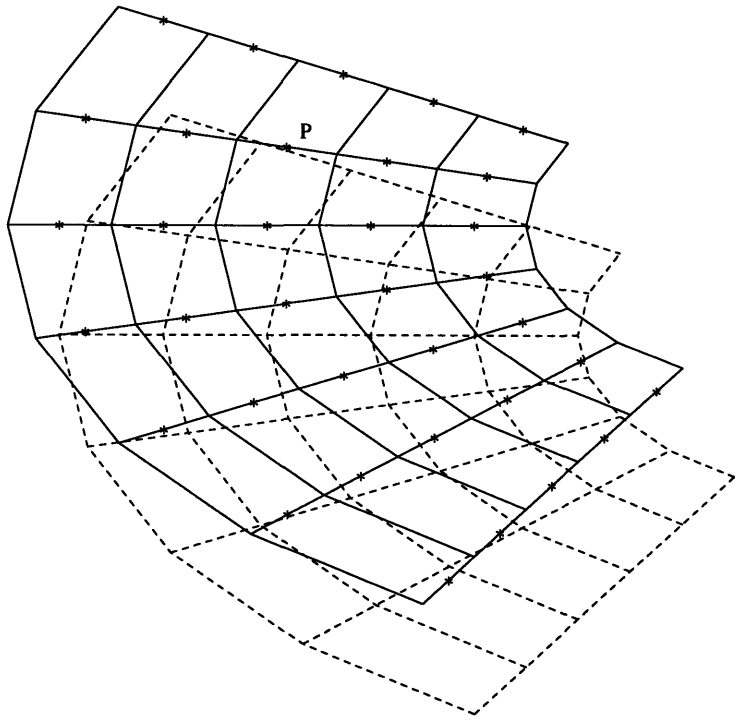

Figure 2-2: The encounter problem. The solid lines are the mesh of vortex segments most recently emitted by the blade. The dotted lines are vortex filaments left by the previous blade passage. Each control point is represented by an asterisk (*). The control point labelled P is close to a vortex line from the previous wake.

sents a continuous sheet of distributed vorticity, which induces a continuous velocity field. However, according to the Biot-Savart law, the induced velocity due to a finite strength filament varies with the inverse square of the distance from the filament center. Thus the velocity tends toward infinity when one calculates the velocity near a segment. In reality, downwash velocities are approximately one order of magnitude smaller than the rotor's forward speed. Though strong vortices are emitted from the blade tips, high induced velocities are prevented by the viscosity in the fluid. To combat the numerical difficulty of using finite strength vortices, vortex cores have been used to simulate viscous effects and keep the induced velocities finite [15, pages 536–543]. Unfortunately, very little is known about how large actual vortex core sizes should be, and the choice of the core size can significantly affect results.

The issue manifests itself most clearly in the *encounter problem.* The velocity field

is only calculated at a discrete set of arbitrarily chosen control points. Due to the geometry of the wake, some of the control points may lie close to a vortex filament, as in Figure 2-2. In this case, the induced velocity calculated at point P could be higher than is physically realizable. Even if a core radius is present, the induced velocity is still strongly dependent on distance to a vortex segment. Thus, while the velocity field should be smooth and continuous (except across a vortex sheet), it can may appear to vary in both magnitude and direction between closely spaced or adjacent control points. Fortunately, occurrences of the encounter problem are random, and not many points should be affected, so its effects on a power calculation are usually slight.

In theory, after selecting a wake geometry and using a vortex lattice code to calculate the influence coefficient matrix, $\boldsymbol{W}$, Equation (2.26) could be used to find the circulation distribution which required the minimum power. However, if the encounter problem introduced noise to the velocity calculations, then this would strongly affect the optimization. The optimization would adjust the circulation distribution to make use of the anomalous entries in the $\boldsymbol{W}$ matrix. This would be enough to make the influence coefficient matrix unsuitable for optimization purposes. Therefore, near wake analysis cannot be used to find a minimum induced loss lift distribution for a rotor.

Chapter 3

Far Wake Theory and Minimum Induced Loss Conditions

Minimum induced loss (m.i.l.) lift distributions are already known for fixed wings and propellers. The m.i.l. conditions for a rotor will be derived in this chapter. It will be shown that a set of common, fundamental principles, here referred to as *far wake theory*, govern the optimal solutions for all three systems: wings, propellers, and rotors.

Far wake theory hinges on the recognition that the thrust at the lifting system (*e.g.*, at the rotor disk) is proportional to the momentum in the wake. Also, the induced power of the system is equal to the rate at which energy is added to the flow in the far wake. These principles can only be applied to inviscid, irrotational flow, and they make use of the Kutta-Joukowski theorem, which relates bound circulation to the force on a lifting line.

In the next section, the m.i.l. solutions for a wing and a propeller will be discussed in light of far wake theory. Then, in Section 3.2, far wake theory will be used to find the necessary conditions for the optimal rotor. However, far wake theory does not examine the aerodynamic characteristics of the object which created the wake, so it will not necessarily limit the solution to one which is physically realizable. Thus, the m.i.l. rotor problem must be extended to include constraints on the maximum allowable local lift at any point on a blade. This is done in the last part of this

chapter.

3.1 Optimized Induced Drag — Classical Cases

The first system for which far wake theory can be used to derive a minimum induced loss condition is the finite-span, fixed wing. Prandtl examined this system in the early part of the Twentieth Century and derived the famous elliptical lift distribution. The wake was modeled as an infinite number of infinitesimal strength horseshoe vortices distributed along the span of the wing. The vortices induced a downwash at the wing. This reduced the effective angle of attack, tilted the net aerodynamic force backwards slightly, and, thus, created *induced drag.* Using a spanwise loading analysis (see Section 2.3), Prandtl found an induced drag coefficient for a wing with an arbitrary circulation distribution. From this, he could show that the distribution for minimum induced losses is elliptical [18].

The elliptical wing solution can also be generated using far wake arguments. The lifting system is projected onto a conceptual plane, the Trefftz plane, which is perpendicular to the direction of flight [29, Section 27]. The problem is thereby converted to a question of finding the two-dimensional velocity potential which causes the minimum induced drag. Integral equations for the lift and drag can be derived in terms of the velocity potential in the far wake. Munk [23] minimizes the drag with respect to variations in the velocity potential. If the planar wake of the lifting line is regarded as a rigid body then this analysis leads to a significant geometric interpretation. The m.i.l. flow is identical to the flow due to a horizontal, two-dimensional flat plate moving downward with constant velocity in an incompressible, inviscid fluid, as viewed by an observer who is stationary with respect to fluid far from the plate. The perpendicular component of the flow at the wake sheet is constant.

Shortly afterwards, in 1919, Betz [6] described the necessary conditions to achieve the minimum induced power loss, at a given thrust and advance ratio, for a lightly loaded propeller. Betz's original analysis dealt with the limit of an infinite number of blades, but Prandtl, working with Betz, added an approximate correction factor

to handle a finite number of blades [29]. This introduced tip effects to the optimality condition, ensuring that the lift and circulation fell to zero at the blade tips. Later, in 1929, Goldstein developed an exact solution for the problem by using infinite series to solve the elliptic partial differential equations that govern the flow between the vortex sheets of two adjacent blades [12]. Glauert summarized most of this work in a book edited by Durand [10].

The assumption of light loading means that the wake neither contracts nor distorts as it moves away from the propeller. The wake sheet surface has the shape of a constant pitch screw, in which the screw helix angle, ϕ, is larger at the axis than at the outer radii (see Figure 3-1). Thus, the locus of points traced out by any point on the blade is an undistorted helix. Also, because of the light loading assumption, the wake sheet surface is periodic.

To develop the optimal solution, Betz examined the wake far downstream from the lifting system, as Munk had done with the fixed wing. Betz derived integral equations for the thrust and power in the far wake. Minimizing the power with respect to variations in the circulation yielded the condition that the flow had to be locally perpendicular to the wake surface. Using this flow, the optimal circulation at any radius was found by integrating the velocity around a circular path enclosing the propeller axis.

Betz referred to the m.i.l. propeller flow as the "rigid-wake condition," and gave it a geometric interpretation similar to that of the optimal wing: The wake sheet is conceptualized to be an impermeable, rigid body. Then, the optimal flow can be generated by the slow, axial translation of this rigid screw surface.

It should be noted that the term, "rigid-wake condition," can be misleading. Modern interpretations of the condition stress that, in order for the flow to move locally perpendicular to the surface, the fluid must move both axially and in the swirl direction. However, the flow does not undergo a rigid body rotation nor a rigid body translation. Figure 3-1, adapted from Larrabee [20], illustrates this. The wake appears to undergo a rigid body translation, with an *apparent* velocity v', but, in reality, the wake section moves at $v' \cos \phi$.

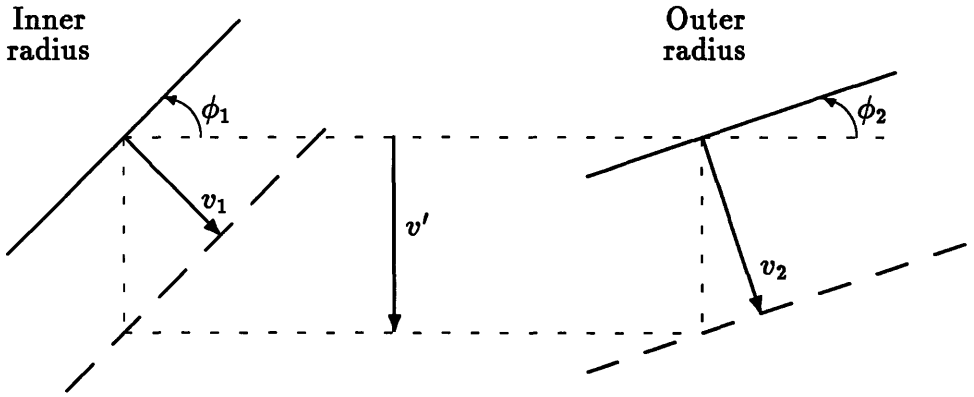

Figure 3-1: Flow in the wake of an optimal propeller. The helix angle, ϕ, changes with radius. From Larrabee and French [20].

As a practical matter, the applicability of these theories may seem limited by the assumption of light loading. However, experiments on hovering rotors (which are not lightly loaded) have indicated that the theories are robust [19]. In these experiments, a two bladed rotor, operating at blade loadings (C_T/σ) from approximately 0.04 to 0.11, was shown to have power requirements which closely matched those predicted by Goldstein's theory. Further evidence of the validity of the optimality conditions is seen in the fact that these methods represented state of the art in propeller design for years. Also, the theory has directed the design of optimal horizontal axis windmills [20].

3.2 Application to a Lightly Loaded Rotor

The most important concept used in the previous section was the idea of examining the lifting system in the far wake, rather than at the lifting surface. This concept will also be applied to rotorcraft. Although the far wake of a rotor is considerably more complex than that of a wing or a propeller, geometric considerations such as periodicity will allow the problem to be simplified. In addition, expressions for energy and forces in the wake will be derived which are equivalent to the kinetics derived for the near wake.

3.2.1 Geometry of the Far Wake

Analysis of the flow in the far wake is considerably simpler than analysis of the flow in the near wake. One reason is that the flow in the far wake is not complicated by interactions with the blade. Flow in the near wake is affected by the boundary layer at the blade and separation effects. These effects have dissipated by the time the flow reaches the far wake. Furthermore, typical rotor blade tip speeds are usually transonic, so a near wake analysis may have to account for compressibility in the flow. Fortunately, the induced velocities found in the far wake are approximately one order of magnitude smaller, so the flow can be assumed to be inviscid and irrotational. Of course, inviscid potential flows can be described by an elliptic field equation, *i.e.*, Laplace's equation, which makes this a familiar problem.

Other simplifications to the problem come from the geometry of the far wake structure and the flight conditions of the rotor. This analysis is limited to lightly loaded rotors, which, as in propeller analysis, means that contraction and distortion in the wake can be neglected. This yields the same wake geometry as the rigid wake in a vortex lattice analysis. The wake sheets for a lightly loaded, two bladed rotor are shown in Figure 3-2. In this document, the term, "wake sheets," will refer to the two-dimensional, curved surface that contacted the blades. Also, the term, "wake tube," refers to the volume of space containing the wake sheets and the space in between them, bounded by the radius of the blades. Finally, the term, "wake," is reserved for all of the volume of air that was affected by the passing of the rotor. This volume extends beyond the radius of the rotor. As shown in the figure, the wake sheets (and, hence, the entire wake) are periodic in the $\hat{\tau}$ direction. The shape of the wake sheets is a well-defined skewed helix and the wake tube is a well-defined skewed circular cylinder.

Note that objects in a potential flow affect the velocity field asymptotically out to infinity, so this implies that the wake includes *all* of the air behind and in front the rotor. Fortunately, the entire wake need not be examined. Given that the far wake is periodic, the induced velocity field and velocity potential must also be periodic. To evaluate performance of the rotor then, only one period of the wake needs to be

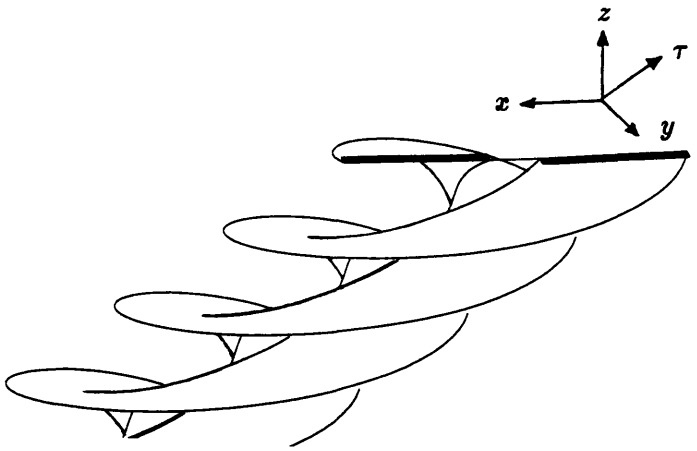

Figure 3-2: The wake sheets left by a two bladed, lightly loaded rotor. Note that the sheets are periodic.

considered. Furthermore, since the helicopter was assumed to be in steady flight, each individual blade experiences the same conditions at each azimuthal station. Thus, only a volume demarcated by two consecutive blade wake sheets for a single period is examined.

The reduced control volume, $\mathcal{V}$, for the two bladed rotor is shown in Figure 3-3. The control volume is bounded by a surface, $\mathcal{S}$. As shown in the figure, the surface $\mathcal{S}$ can be subdivided into an upper bounding surface, $\mathcal{S}_u$; a lower bounding surface, $\mathcal{S}_l$; two vertical planes, $\mathcal{S}_{2\pi}$ and $\mathcal{S}_0$; and an outer annular band, $\mathcal{S}_\infty$. The surfaces $\mathcal{S}_u$ and $\mathcal{S}_l$ are skewed helices and contain the wake sheets, one of which is labelled $\mathcal{W}$. The location of $\mathcal{S}_{2\pi}$ and $\mathcal{S}_0$ have been arbitrarily chosen to lie in the planes where the blade azimuth angle is 2π and 0, respectively. The surface $\mathcal{S}_\infty$ actually lies at a radius of infinity, where all effects of the rotor have asymptotically died out. Periodicity requires that the velocity potential at $\mathcal{S}_{2\pi}$ matches that at $\mathcal{S}_0$, and that the velocity potential of any point on $\mathcal{S}_l$ outside of the wake sheet is the same as that of the corresponding point on $\mathcal{S}_u$, lying in the $\hat{\tau}$ direction.

A further description could be useful. The volume $\mathcal{V}$ has the shape of a split washer, except that the washer is not skewed and has a hole in the middle. If multiple copies of $\mathcal{V}$ are stacked on top of each other, then a wake tube (for an infinite radius rotor) is formed.

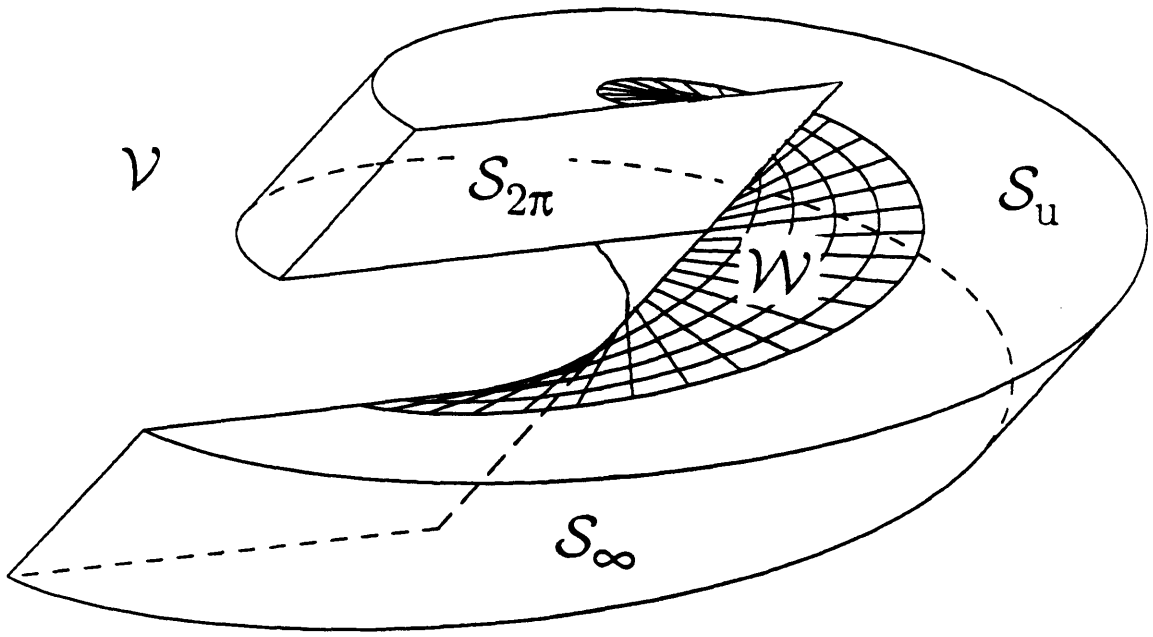

Figure 3-3: The control volume, $\mathcal{V}$. The control volume is enclosed by the surface $\mathcal{S}$, which is composed of the upper and lower surfaces, $\mathcal{S}_{\mathrm{u}}$ and $\mathcal{S}_{\mathrm{l}}$, the vertical planes $\mathcal{S}_0$ and $\mathcal{S}_{2\pi}$, and the outer bounding surface $\mathcal{S}_\infty$. The outer surface conceptually lies at an infinite radius. The surfaces $\mathcal{S}_0$ and $\mathcal{S}_{\mathrm{l}}$ are hidden from view.

Having discussed the structure of the wake, boundary conditions for the velocity potential can now be formally stated. First, recall that the velocity potential is defined in terms of the velocity,

$$\nabla\phi = \boldsymbol{v}\,. \tag{3.1}$$

To arrive at the first boundary condition, it is recognized that air which is infinitely far from the rotor is unaffected by its presence. Thus, that air is still and

$$\phi = \text{constant, on } \mathcal{S}_\infty.$$

For convenience, since the constant is arbitrary, it will be assumed to equal zero. Thus,

$$\phi = 0\,, \text{on } \mathcal{S}_\infty. \tag{3.2}$$

Secondly, as was mentioned earlier, certain boundaries of $\mathcal{V}$ which were introduced

to simplify the problem are artificial and denote areas where the solution repeats. This is true of any radial, vertical plane, so that

$$\phi\big|_{\mathcal{S}_0} = \phi\big|_{\mathcal{S}_{2\pi}} \ . \tag{3.3}$$

This notation is meant to indicate the velocity potential at every individual point on $\mathcal{S}_0$ is equal to the velocity potential at a particular, associated point on $\mathcal{S}_{2\pi}$. The wake is periodic in the $\hat{\tau}$ direction, so the point on $\mathcal{S}_{2\pi}$ associated with a point on $\mathcal{S}_0$ is found by moving in the $\hat{\tau}$ direction, for a distance equal to the inter wake sheet spacing, $2\pi R\sqrt{\mu^2+\lambda^2}$. This relationship applies to every point in the wake, not just those on the borders of $\mathcal{V}$. For instance, a point lying in between $\mathcal{S}_{\rm u}$ and $\mathcal{S}_{\rm l}$ is associated with a point in the $\hat{\tau}$ direction. However, that point is not in $\mathcal{V}$; it is in the volume demaracted by the succeeding blade wake sheet and $\mathcal{S}_{\rm u}$.

Lastly, to satisfy the conditions of irrotational and inviscid flow (as encompassed by Laplace's equation), the velocity potential must be continuous everywhere except at a singularity. The wake sheet, $\mathcal{W}$, is composed of distributed vortex filaments and is thus a singular surface. On $\mathcal{W}$, the velocity perpendicular to the sheet is continuous, but the velocity tangent to the sheet is not. It can be shown that this jump in the velocity potential at any point on the wake is equal to the bound circulation of that point in the wake [17, Section 2.7], [11, Chapter 5], so that

$$\phi\big|_{\mathcal{S}_{\rm u}} - \phi\big|_{\mathcal{S}_{\rm l}} = -\Gamma\big|_{\mathcal{W}} \ . \tag{3.4}$$

As in Equation(3.3), this notation indicates that ϕ should be evaluated at a point on $\mathcal{S}_{\rm u}$ and a particular associated point on $\mathcal{S}_{\rm l}$.

For points on $\mathcal{S}_{\rm u}$ and $\mathcal{S}_{\rm l}$ that are not part of the wake, the distinction between $\mathcal{S}_{\rm u}$ and $\mathcal{S}_{\rm l}$ is artificial and

$$\phi\big|_{\mathcal{S}_{\rm u}} = \phi\big|_{\mathcal{S}_{\rm l}} \ , \ \text{for} \begin{cases} (x,y,z) \notin \mathcal{W} \ , \\ (x,y,z) \in \mathcal{S}_{\rm u} \ . \end{cases} \tag{3.5}$$

The preceding four boundary conditions are referred to as *essential boundary conditions*, and any valid solution for this domain must fulfill these conditions. The essential boundary conditions are independent of any trim conditions or other physical requirements of the rotor.

3.2.2 Energy and Momentum in the Far Wake

Energy and momentum in the far wake are due to the passage of the rotor. The thrust at the rotor blades imparts momentum to the flow, which persists in the far wake. The rate of energy change in the far wake is equal to the power production at the rotor blades, *i.e.*, the induced power. In this section, expressions, in integral form, are derived for the forces, moments, and induced power. Although the integrals are taken over $\mathcal{V}$ and not the whole wake, periodicity implies that multiplying the integrals by the number of blades, B, will yield the total quantity for the whole rotor.

The total linear momentum in the control volume is

$$\begin{aligned} \boldsymbol{\xi} &= \int_{\mathcal{V}} \rho \boldsymbol{v} \, dV \\ &= \int_{\mathcal{V}} \rho \boldsymbol{\nabla}\phi \, dV \, . \end{aligned} \tag{3.6}$$

The divergence theorem [14, page 60] can be written in terms of the gradient of a scalar function (rather than the divergence of a vector function) as

$$\int_{\mathcal{V}} \boldsymbol{\nabla}\phi \, dV = \int_{\mathcal{S}} \phi \hat{\boldsymbol{n}} \, dA \, , \tag{3.7}$$

where $\hat{\boldsymbol{n}}$ is the outward pointing normal on $\mathcal{S}$. Applying this to the momentum integral yields

$$\boldsymbol{\xi} = \int_{\mathcal{S}} \rho\phi \, \hat{\boldsymbol{n}} \, dA \, . \tag{3.8}$$

This integral can be subdivided using the constitutive parts of $\mathcal{S}$, so that

$$\int_{\mathcal{S}} = \int_{\mathcal{S}_0} + \int_{\mathcal{S}_{2\pi}} + \int_{\mathcal{S}_\infty} + \int_{\mathcal{S}_\text{a}} + \int_{\mathcal{S}_\text{l}} \, . \tag{3.9}$$

Then, by applying the essential boundary conditions (equations (3.2)–(3.5)) and realizing that $\hat{\boldsymbol{n}}$ points in opposite directions on opposing faces of a surface, it is seen that the integrals over $\mathcal{S}_0$ and $\mathcal{S}_{2\pi}$ sum to zero. Also, the integral over $\mathcal{S}_\infty$ is identically zero. For the integrals over $\mathcal{S}_\mathrm{u}$ and $\mathcal{S}_\mathrm{l}$, only the portions over $\mathcal{W}$ will remain, leaving

$$\begin{aligned}\boldsymbol{\xi} &= \int_{\mathcal{S}_\mathrm{u}} \rho\phi\,\hat{\boldsymbol{n}}\,dA + \int_{\mathcal{S}_\mathrm{l}} \rho\phi\,\hat{\boldsymbol{n}}\,dA \\ &= \int_{\mathcal{W}} \rho\Delta\phi\,\hat{\boldsymbol{n}}\,dA \\ &= -\int_{\mathcal{W}} \rho\Gamma\,\hat{\boldsymbol{n}}\,dA\,. \end{aligned} \tag{3.10}$$

This reduction of a surface integral over $\mathcal{S}$ to a smaller surface integral over $\mathcal{W}$ will be used repeatedly in this chapter.

The average force exerted on the flow is equal to the momentum, $\boldsymbol{\xi}$, divided be the time over which the impulse was applied, *i.e.*, one period of the blade rotation, $2\pi/\Omega$. The average force on the rotor is equal and opposite to this, so

$$\boldsymbol{F} = -\frac{B\Omega}{2\pi}\boldsymbol{\xi} = \frac{B\Omega}{2\pi}\int_{\mathcal{W}} \rho\Gamma\,\hat{\boldsymbol{n}}\,dA\,. \tag{3.11}$$

The net moment on the rotor is

$$\boldsymbol{M} = \frac{B\Omega}{2\pi}\int_{\mathcal{W}} \rho\Gamma\,\boldsymbol{r}\times\hat{\boldsymbol{n}}\,dA\,. \tag{3.12}$$

The kinetic energy of the flow in $\mathcal{V}$ is

$$\begin{aligned}\mathrm{KE} &= \int_{\mathcal{V}} \frac{1}{2}\rho\,|\boldsymbol{v}|^2\,dV \\ &= \int_{\mathcal{V}} \frac{1}{2}\rho\,|\boldsymbol{\nabla}\phi|^2\,dV\,. \end{aligned} \tag{3.13}$$

For any function ϕ, it can be shown that

$$|\boldsymbol{\nabla}\phi|^2 = \boldsymbol{\nabla}\phi\cdot\boldsymbol{\nabla}\phi = \boldsymbol{\nabla}\cdot(\phi\,\boldsymbol{\nabla}\phi) - \phi\,\boldsymbol{\nabla}^2\phi\,. \tag{3.14}$$

In this case $\boldsymbol{\nabla}^2\phi = 0$, since incompressible potential flows satisfy Laplace's equation.

Therefore, applying equation (3.14) to equation (3.13) yields

$$\begin{aligned} \mathrm{KE} &= \int_{\mathcal{V}} \frac{1}{2}\rho \nabla \cdot (\phi \nabla \phi)\, dV \\ &= \int_{\mathcal{S}} \frac{1}{2}\rho \phi\, \nabla\phi \cdot \hat{\boldsymbol{n}}\, dA \quad \text{(by the divergence theorem)} \\ &= -\int_{\mathcal{W}} \frac{1}{2}\rho \Gamma\, \boldsymbol{v} \cdot \hat{\boldsymbol{n}}\, dA\,. \end{aligned} \tag{3.15}$$

Finally, the time averaged induced power is simply the kinetic energy divided by the period, so

$$P_{\mathrm{i}} = -\frac{B\Omega}{2\pi} \int_{\mathcal{W}} \frac{1}{2}\rho \Gamma\, \boldsymbol{v} \cdot \hat{\boldsymbol{n}}\, dA\,. \tag{3.16}$$

In forward flight, this quantity is positive, because the induced velocity, $\boldsymbol{v}$, points into the control volume over most of the top sheet, $\mathcal{W}$, so $\boldsymbol{v} \cdot \hat{\boldsymbol{n}}$ is usually negative.

Equations (3.11), (3.12), and (3.16) can be compared to their near wake counterparts, equations (2.18), (2.18), and (2.26). Although the equations may look dissimilar, each of the equations does yield the same result as its counterpart. The relation between the equations can be seen by realizing that the normal to the wake sheet will point in a direction perpendicular to both the velocity at the blade and the blade axis, *i.e.*, $(\boldsymbol{U} \times \hat{\boldsymbol{r}})$ is perpendicular to the sheet. Also, it can be shown that

$$\Omega\, \hat{\boldsymbol{n}}\, dA = \boldsymbol{U} \times \hat{\boldsymbol{r}}\, dr d\psi\,. \tag{3.17}$$

It should be noted that the double integral used in the *near* wake equations is a single spatial integral inside a single time averaging integral. This differs from the surface integral used in the *far* wake calculations.

In addition, the power calculations also seem to differ by a factor of $\frac{1}{2}$. This is because the net induced velocity flux in the far wake is twice that found in the near wake. This can be deduced for a rotor based on momentum arguments and it is analogous to the fact that the downwash in the Trefftz plane of a fixed wing is twice that at the wing and that the induced velocity in the far wake of a Betz-Prandtl/Goldstein propeller is twice that at the propeller. In those cases, $\boldsymbol{v}(r,\psi) = 2\boldsymbol{w}(r,\psi)$. It is not, however, the case for a rotor that at any given position (r,ψ) in

the far wake, the velocity is twice that of the corresponding location at the blades because of the loss of symmetry in the wake geometry.

Unlike the velocity field, the lift distribution in the far wake is exactly the same as that in the near field. Helmholtz's vorticity theorems ensure that the circulation in the far wake is equal to that left by the blade at the instant the blade passed by that point. Thus, knowledge of ϕ reveals the circulation at the rotor disk and, hence, the lift distribution at the rotor disk.

3.3 Far Wake Power Optimization

In this section, the necessary conditions for a rotor to achieve the minimum induced power loss are derived. The derivation relies on the assumption of light loading and the near wake analysis developed in Section 3.2.2. The optimization procedure is based on Munro's [24] analysis, which used variational principles. Expressions for the induced power, forces, and moments (which are functions of the velocity potential) are combined to form a cost functional that is minimized with respect to variations in the potential.

First, the optimization is performed for the case where there are no constraints on the maximum allowable local lift on a blade. This is referred to as the *unconstrained optimal* solution. Then, in Section 3.3.2, the optimization is repeated for the case when physical limits are placed on the local lift achieved by a blade. This solution is called the *constrained optimal* solution.

3.3.1 Unconstrained Optimization

The question that is to be examined is: For a given set of flight conditions, what is the lift distribution which will require the minimum induced power? Specifying the flight conditions requires picking a desired forward speed, thrust, rolling moment, and pitching moment. The flight conditions must be steady state or the far wake periodicity conditions would not be true. In level, forward flight, the required level of thrust is equal to the helicopter's weight. The helicopter also has no net pitching

and rolling moments. These conditions are enforced as constraints on the power minimization. The forward speed directly determines the shape of the wake. Therefore, it is implicitly enforced and does not require a constraint function. A cost function which contains the induced power and also the explicit constraints is

$$\Pi^{\mathrm{u}} = P_{\mathrm{i}} + \nu_T(T - T_{\mathrm{req}}) + \omega_x(M_x - M_{x\,\mathrm{req}}) + \omega_y(M_y - M_{y\,\mathrm{req}})\,. \tag{3.18}$$

Here, ν_T, ω_x, and ω_y are Lagrange multipliers. Also, $(\cdot)_{\mathrm{des}}$ denotes the valued required to keep the rotor in trim, and $(\cdot)^{\mathrm{u}}$ indicates that the maximum local lift is *un*constrained. The multipliers may be written in vector form as

$$\boldsymbol{\nu} = \nu_T \hat{\boldsymbol{k}} \tag{3.19}$$

and

$$\boldsymbol{\omega} = \omega_x \hat{\boldsymbol{\imath}} + \omega_y \hat{\boldsymbol{\jmath}}\,, \tag{3.20}$$

so that

$$\Pi^{\mathrm{u}} = P_{\mathrm{i}} + \boldsymbol{\nu} \cdot (\boldsymbol{F} - \boldsymbol{F}_{\mathrm{req}}) + \boldsymbol{\omega} \cdot (\boldsymbol{M} - \boldsymbol{M}_{\mathrm{req}})\,. \tag{3.21}$$

Using Equations (3.16), (3.11), and (3.12), this can be written in terms of ϕ and Γ as

$$\begin{aligned} \Pi^{\mathrm{u}} \;=\; & \frac{B\Omega}{2\pi} \int_{\mathcal{V}} \frac{\rho}{2} \left|\boldsymbol{\nabla}\phi\right|^2 dV + \frac{B\Omega}{2\pi} \int_{\mathcal{W}} \rho\Gamma(\boldsymbol{\nu} \cdot \hat{\boldsymbol{n}} + \boldsymbol{\omega} \cdot (\boldsymbol{r} \times \hat{\boldsymbol{n}}))\, dA \\ & - \nu_T T_{\mathrm{req}} - \omega_x M_{x\,\mathrm{req}} - \omega_y M_{y\,\mathrm{req}}\,. \end{aligned} \tag{3.22}$$

Taking the variation of Π^{u} with respect to Γ, ϕ, ν_T, ω_x, and ω_y yields

$$\begin{aligned} \delta\Pi^{\mathrm{u}} \;=\; & \frac{B\Omega}{2\pi} \int_{\mathcal{V}} \rho\, \boldsymbol{\nabla}\phi \cdot \delta\left(\boldsymbol{\nabla}\phi\right) dV \\ & + \frac{B\Omega}{2\pi} \int_{\mathcal{W}} \rho(\boldsymbol{\nu} \cdot \hat{\boldsymbol{n}} + \boldsymbol{\omega} \cdot (\boldsymbol{r} \times \hat{\boldsymbol{n}}))\delta\Gamma\, dA \\ & + (T - T_{\mathrm{req}})\delta\nu_T + (M_x - M_{x\,\mathrm{req}})\delta\omega_x + (M_y - M_{y\,\mathrm{req}})\delta\omega_y\,. \end{aligned} \tag{3.23}$$

The first term on the right hand side of Equation (3.23) is the first variation of

the induced power. For small variations in ϕ, this becomes

$$\delta P_{\mathrm{i}} = \frac{B\Omega}{2\pi} \int_{\mathcal{V}} \rho \, \boldsymbol{\nabla}\phi \cdot \boldsymbol{\nabla}\left(\delta\phi\right) \, dV \, . \tag{3.24}$$

Evaluating this term requires an integration by parts. The integration by parts formula is (see [14])

$$\int_{\mathcal{V}} \boldsymbol{u} \cdot \boldsymbol{\nabla} v \, dV = \int_{\mathcal{S}} v \, \boldsymbol{u} \cdot \hat{\boldsymbol{n}} \, dA - \int_{\mathcal{V}} \boldsymbol{\nabla} \cdot \boldsymbol{u} \, v \, dV \, . \tag{3.25}$$

In Equation (3.25), if $\boldsymbol{\nabla}\phi$ replaces $\boldsymbol{u}$, then $\boldsymbol{\nabla} \cdot \boldsymbol{u} = \nabla^2\phi$. Also, letting $\delta\phi$ replace v leads to

$$\delta P_{\mathrm{i}} = \frac{B\Omega}{2\pi} \int_{\mathcal{S}} \rho \, \boldsymbol{\nabla}\phi \cdot \hat{\boldsymbol{n}} \, \delta\phi \, dA - \frac{B\Omega}{2\pi} \int_{\mathcal{V}} \rho \, (\nabla^2\phi) \delta\phi \, dV \, . \tag{3.26}$$

As was done in Section 3.2.2, the essential boundary conditions can be applied to simplify the integral over $\mathcal{S}$. Note that the integral over $\mathcal{S}_\infty$ is zero, because $\delta\phi = 0$ there since ϕ is specified on that surface (see Equation (3.2)). Like before, the integrals over the remainder of $\mathcal{S}$ reduce to an integral over $\mathcal{W}$ alone, and

$$\delta P_{\mathrm{i}} = -\frac{B\Omega}{2\pi} \int_{\mathcal{W}} \rho \, \boldsymbol{\nabla}\phi \cdot \hat{\boldsymbol{n}} \, \delta\Gamma \, dA - \frac{B\Omega}{2\pi} \int_{\mathcal{V}} \rho \, (\nabla^2\phi) \delta\phi \, dV \, . \tag{3.27}$$

It is worthwhile to examine this equation before returning to the minimization of Π^{u}. Equation 3.27 alone could be used to minimize the induced power if trim conditions did not have to be enforced. The induced power can be minimized by making it stationary with respect to variations in the circulation and the potential. The first term on the right hand side of Equation (3.27) gives the *sensitivity* of the induced power to changes in the circulation. The sensitivity of any point on the disk is proportional to the induced velocity, $\boldsymbol{\nabla}\phi$, at the corresponding position *in the far wake.* As mentioned before, the circulation at a point in the wake is the same as the circulation at the corresponding position *at the rotor blades.* Also, the blade aerodynamics directly control the circulation (not the velocity potential). Thus, the far wake wash information could be useful when trying to physically control the induced power. The wash would show what portions of the lift distribution should

be changed to have the maximum affect on the induced power.

Returning to the minimization of the cost function, Equations (3.27) and (3.24) are substituted back into Equation (3.23) to yield

$$\begin{aligned}\delta\Pi^{u} &= -\frac{B\Omega}{2\pi}\int_{\mathcal{V}}\rho\,(\nabla^2\phi)\,\delta\phi\,dV \\ &\quad -\frac{B\Omega}{2\pi}\int_{\mathcal{W}}\rho\,[\boldsymbol{\nabla}\phi\cdot\hat{\boldsymbol{n}}-(\boldsymbol{\nu}\cdot\hat{\boldsymbol{n}}+\boldsymbol{\omega}\cdot(\boldsymbol{r}\times\hat{\boldsymbol{n}}))]\;\delta\Gamma\,dA \\ &\quad +\delta\nu_T(T-T_{\text{req}})+\delta\omega_x(M_x-M_{x\,\text{req}})+\delta\omega_y(M_y-M_{y\,\text{req}})\,. \qquad (3.28)\end{aligned}$$

The first order necessary condition for Π^{u} to be a minimum is that $\delta\Pi^{u}=0$ for all independent variations in Γ, ϕ, ν_T, ω_x, and ω_y. The second term of Equation (3.28) can be modified by recalling that $\boldsymbol{v}=\boldsymbol{\nabla}\phi$. Also, using a cyclic permutation, it can be shown that $\omega\cdot(\boldsymbol{r}\times\hat{\boldsymbol{n}})=(\omega\times\boldsymbol{r})\cdot\hat{\boldsymbol{n}}$. Then the necessary conditions can be written as

$$T = T_{\text{req}} \qquad (3.29)$$

$$M_x = M_{x\,\text{req}} \qquad (3.30)$$

$$M_y = M_{y\,\text{req}} \qquad (3.31)$$

$$\nabla^2\phi = 0 \qquad \text{in } \mathcal{V} \qquad (3.32)$$

$$\boldsymbol{v}\cdot\hat{\boldsymbol{n}} = (\boldsymbol{\nu}+\omega\times\boldsymbol{r})\cdot\hat{\boldsymbol{n}} \qquad \text{on } \mathcal{W}. \qquad (3.33)$$

Together with the essential boundary conditions on ϕ (Equations (3.2)–(3.5)), these conditions represent a complete description of the velocity potential for the unconstrained, minimum induced loss, lightly loaded rotor problem.

The first of the three necessary conditions require that the optimal solution achieve the desired thrust and trim conditions. Equation (3.32) requires that Laplace's equation be satisfied. This is satisfied since the flow is a potential flow. The last condition is the most interesting. It defines the relation between the optimal flow at the wake sheet and the shape of the sheet. The flow is effectively the same as a flow past an impermeable membrane (the wake sheet) which translates at a speed ν_T and shears at an angular rate $\boldsymbol{\omega}$. The effects of $\boldsymbol{\omega}$ is interpreted as a shearing, rather than a

rigid body rotation about the wake tube axis. This is because, for any element of the wake, its center of rotation is the point in the wake corresponding to the hub location at the time that the wake element was created.

It should be noted that Equation (3.33) does not by itself require that the wake sheet have the skewed, screw-like form that came from the light loading assumption. Instead, the information about the shape of the wake sheet is implied by $\hat{\boldsymbol{n}}$, which follows the shape of the sheet. Thus, the equation could be applied to wake sheets of other geometries, as long as the Lagrange multipliers of interest only have the components specified in Equations (3.19) and (3.20).

Also, the last condition is actually a generalization of Betz's solution for the minimum induced loss propeller. In the case of the propeller, only the thrust Lagrange multiplier is used and the condition reduces to

$$\boldsymbol{v} \cdot \hat{\boldsymbol{n}} = \boldsymbol{\nu} \cdot \hat{\boldsymbol{n}} = \nu_T \, \hat{\boldsymbol{k}} \cdot \hat{\boldsymbol{n}} \,, \tag{3.34}$$

where ν_T now equals v' shown in Figure 3-1.

3.3.2 Constrained Optimization

The optimality conditions for the rotor will now be extended to incorporate constraints for the maximum allowable local lift on a blade. As will be shown in Chapter 5, if these additional constraints are not imposed, then the optimal local lifts will be excessively high. Conventional airfoil technology would be unable to achieve the required lifts.

The lift constraints are effectively constraints on the local circulation. A relation between the local circulation and the local lift coefficient can be found by examining the lift at any blade section. For a two-dimensional blade section with a lift coefficient C_l and chord c, the lift is related to lifting line theory by

$$\rho U_\perp(r,\psi)\Gamma(r,\psi) = \frac{1}{2}\,\rho U_\perp^2(r,\psi) c\, C_l(r) \,, \tag{3.35}$$

where $U_\perp = \sqrt{U_T^2 + U_z^2}$ is the velocity normal to the lifting line and in the plane of the wake sheet. The maximum allowable circulation is therefore

$$\Gamma(r,\psi) \le \Gamma_{\max}(r,\psi) = \frac{1}{2} U_\perp(r,\psi) c\, C_{l_{\max}}(r)\,. \tag{3.36}$$

Unlike the previously imposed trim constraints, which dealt with integral quantities, the $C_{l_{\max}}$ constraint is imposed on individual points of the distribution. The new constraint can be added to the previous functional, Equation (3.18) using a Lagrange multiplier, $\vartheta(r,\psi)$, so that

$$\Pi = \Pi^u + \frac{B\Omega}{2\pi} \int_{\mathcal{W}} \vartheta(r,\psi)\,[\Gamma(r,\psi) - \Gamma_{\max}]\; dA\,. \tag{3.37}$$

Taking the variation of the new term with respect to Γ and ϑ produces

$$\frac{B\Omega}{2\pi} \int_{\mathcal{W}} \vartheta\, \delta\Gamma\, dA + \frac{B\Omega}{2\pi} \int_{\mathcal{W}} (\Gamma - \Gamma_{\max})\, \delta\vartheta\, dA\,. \tag{3.38}$$

The variation of the entire Π functional then becomes

$$\begin{aligned}
\delta\Pi \;=\; & -\frac{B\Omega}{2\pi} \int_{\mathcal{V}} \rho\,(\nabla^2\phi)\,\delta\phi\, dV \\
& + \frac{B\Omega}{2\pi} \int_{\mathcal{W}} (\Gamma - \Gamma_{\max})\,\delta\vartheta\, dA \\
& - \frac{B\Omega}{2\pi} \int_{\mathcal{W}} \rho\,[\boldsymbol{\nabla}\phi\cdot\hat{\boldsymbol{n}} - (\boldsymbol{\nu}\cdot\hat{\boldsymbol{n}} + \boldsymbol{\omega}\cdot(\boldsymbol{r}\times\hat{\boldsymbol{n}}) - \vartheta)]\;\delta\Gamma\, dA \\
& + \delta\nu_T(T - T_{\text{req}}) + \delta\omega_x(M_x - M_{x\,\text{req}}) + \delta\omega_y(M_y - M_{y\,\text{req}})\,.
\end{aligned} \tag{3.39}$$

Following the same reasoning used for the unconstrained optimization, the necessary conditions for the constrained optimal flow are therefore

$$T = T_{\text{req}} \tag{3.40}$$

$$M_x = M_{x\,\text{req}} \tag{3.41}$$

$$M_y = M_{y\,\text{req}} \tag{3.42}$$

$$\nabla^2\phi = 0 \qquad \text{in } \mathcal{V} \tag{3.43}$$

$$\boldsymbol{v} \cdot \hat{\boldsymbol{n}} = (\boldsymbol{\nu} + \omega \times \boldsymbol{r}) \cdot \hat{\boldsymbol{n}} + \vartheta \qquad \text{on } \mathcal{W}, \tag{3.44}$$

and

$$\begin{cases} \vartheta(r,\psi) \geq 0\,, \text{ if } \Gamma(r,\psi) = \Gamma_{\max}(r,\psi) \\ \vartheta(r,\psi) = 0\,, \text{ if } \Gamma(r,\psi) < \Gamma_{\max}(r,\psi)\,. \end{cases} \tag{3.45}$$

Equations (3.40)–(3.45), together with the boundary conditions (Equations (3.2)–(3.5)), completely define the velocity potential in the wake of a constrained, optimal, lightly loaded rotor.

There have been no changes to the first four necessary conditions. However, the $C_{l_{\max}}$ constraint has modified the flow conditions and put requirements on ϑ. The Lagrange multiplier, $\vartheta(r,\psi)$ is zero if the constraint is not active and it is a positive value if the circulation, $\Gamma(r,\psi)$, is on the constraint boundary. The exact value that $\vartheta(r,\psi)$ takes at any constrained location is the subject of Section 4.2.

Equation (3.44) describes the same flow as its unconstrained counterpart (Equation (3.33)) in the regions where the $C_{l_{\max}}$ constraints are not active. However, in the regions where the constraint is active, the speed of the flow normal to the wake sheet is *reduced* by the amount ϑ. This is due to the fact that $\boldsymbol{v} \cdot \hat{\boldsymbol{n}}$ is negative everywhere on the rotor disk except in the reverse flow region. Again, the optimal flow is the same as the flow past a moving, rigid, impermeable wake sheet. In the regions where the the $C_{l_{\max}}$ constraints are active, the membrane is distorted from its unconstrained form. Larger values of ϑ indicate greater deviations of the membrane from the unconstrained form.

Although the optimal rotor flow is more complicated than the minimum induced loss solutions for either the fixed wing of the propeller, the far wake theory provides a convenient, unified framework for analysis. The result is that, in all three cases, the theory yields a detailed description of the optimal flow and how that flow is exactly the same as a flow which is interacting with a moving, impermeable membrane.

Chapter 4

Implementation

The necessary conditions for the minimum induced loss rotor, Equations (3.40)–(3.45), require the solution of a three-dimensional field problem with boundary conditions given by Equations (3.2)–(3.5). It is worth noting that the reduction of the problem to its current form has only been made possible because the equations deal with energy principles in the far wake. If the wake were examined in the nearfield, the interaction of the flow with the blade would have to be modelled. Unfortunately, the time-varying wake shape of the nearfield could be so complicated as to render typical computational fluid dynamics (CFD) techniques useless. Because most helicopter analysts are primarily interested in blade aerodynamics, they examine near wake phenomena. Therefore, CFD codes used for more common fluids applications have not, in general, been applied to helicopter wakes.

An analytical solution or even a reasonable analytical approximation to the rotor problem is not possible, due to the complicated geometry of the wake. Fortunately, the far wake problem is tractable with existing numerical techniques. One common choice by aerodynamicists is to use a finite difference scheme for a numerical method. However, it can be difficult for a finite difference scheme to match both the correct natural (flow stipulations) and essential (farfield and periodicity stipulations) boundary conditions. A better choice seems to be the finite element method. A finite element technique would fully capture the variational principle imbedded in Equation (3.37), whereas the finite difference method would not. By using the finite element method,

the minimization technique and necessary conditions will be more completely satisfied by the discretized domain.

It will be seen that the *un*constrained optimization problem is easier to implement than the constrained problem. Therefore, the discretization of the model will be done in detail for only the unconstrained problem. Then, in Section 4.2, the discretized model will be extended to include the constraints on the allowable local lifts. Afterwards, there is a discussion about how the finite element formulation produces a straightforward calculation of the induced power. The calculation has the useful property that it always overbounds the exact answer. Then, in Section 4.4, the development of an accurate finite element mesh for the wake is discussed. This mesh will be used for the optimizations to be presented in Chapter 5. Lastly, the chapter contains a section on the computer requirements for running this numerical procedure.

4.1 Finite Element Formulation

In this section, a finite element approximation to the unconstrained problem will be developed. The discussion is only meant as a brief introduction to the finite element technique, to give uninitiated readers a look at how a continuous problem is converted to a discrete problem. For more detailed discussions, the reader is referred to any general finite element text, such as Hughes [14], Bathe [4], or Tong [41].

This finite element method is formulated from a variational principle, since that is how the problem was originally formed in Chapter 3. Conceptually, the finite element procedure for solving a field problem is to discretize a domain, then examine all possible potentials within the discretized domain which satisfy the essential boundary conditions. This reduces the set of variations, $\delta\phi$, which can be allowed. The functional, Π, is then minimized with respect to this allowable set of discretized variations.

After a discussion of the discretization, the next topic in this section deals with the application of the essential boundary conditions. Finally, a procedure to solve

the unconstrained optimal problem is explained.

4.1.1 Discretization

The first approximation made is to choose a finite, well-defined volume $\mathcal{V}_\mathrm{d}$ to represent $\mathcal{V}$. Obviously, $\mathcal{V}_\mathrm{d}$ will not have an infinite radius as $\mathcal{V}$ does. Therefore, the radius of $\mathcal{V}_\mathrm{d}$ must be sized such that the effects of the rotor have reached negligible levels before the outer boundary. Otherwise, the boundary will act like a fluid channel and modify the solution. Next, $\mathcal{V}_\mathrm{d}$ is subdivided into a set of M three-dimensional volumes, called elements. The elements are multifacted and each corner is called a node, which also serves as a corner for other adjacent elements. In doing this, the surface, $\mathcal{S}$, has also been approximated by the discretized surface $\mathcal{S}_\mathrm{d}$. Some nodes, the boundary nodes, lie on $\mathcal{S}_\mathrm{d}$ and the remainder lie in the interior of $\mathcal{V}_\mathrm{d}$. The elements are continuous in $\mathcal{V}_\mathrm{d}$, *i.e.*, there are no voids in $\mathcal{V}_\mathrm{d}$, and the elements conform to $\mathcal{S}_\mathrm{d}$ so that there are no elements lying partially on one side of $\mathcal{S}_\mathrm{d}$ and partially on the other side.

For the interior of a particular element, the velocity potential is interpolated from the potentials at the nodes of the element. The $N \times 1$ vector $\mathbf{\Phi}$ denotes the set of unknown potentials at each of the N nodes. If $\phi_m(x, y, z)$ is the value of the potential anywhere in the interior of element m, then

$$\phi_m(x, y, z) = \boldsymbol{H}_m(x, y, z)\mathbf{\Phi} \,. \tag{4.1}$$

Here, $\boldsymbol{H}_m$ is a $1 \times N$ matrix with interpolation functions at the locations corresponding to the nodes of element m, and zeros elsewhere. Interelement continuity is dependent on the order of the interpolating polynomials. For linear polynomials, the resulting ϕ functions are continuous across element boundaries but the derivatives are not. In general, the choice of the interpolation function greatly affects the accuracy of the solution.

In a similar fashion, the derivatives of ϕ are based on differentiating the $\boldsymbol{H}_m$ matrix to get

$$\boldsymbol{\nabla}\phi_m(x, y, z) = \boldsymbol{B}_m(x, y, z)\mathbf{\Phi} \,, \tag{4.2}$$

where $\boldsymbol{B}_m$ is a $3 \times N$ matrix of interpolation functions. The continuity of the $\boldsymbol{\nabla}\phi_m$ solution is thus seen to be one order lower than the potential solution.

Furthermore, recalling Equation (3.4), the circulation at any point on $\mathcal{W}_\mathrm{d}$ can be expressed as a linear function of the nodal potential,

$$\Gamma_m(x,y,z) = \boldsymbol{G}_m(x,y,z)\boldsymbol{\Phi}\,. \tag{4.3}$$

Here, $\boldsymbol{G}_m$ is a $1 \times N$ matrix of functions that differences the potential on opposite sides of $\mathcal{W}_\mathrm{d}$.

For convenience, each of Equations (4.1)–(4.3) can be rewritten in terms of $\boldsymbol{\Phi}_m$, a vector of the nodal potentials of element m only. Then

$$\phi_m(x,y,z) = \boldsymbol{H}\boldsymbol{\Phi}_m\,, \tag{4.4}$$

$$\boldsymbol{\nabla}\phi_m(x,y,z) = \boldsymbol{B}\boldsymbol{\Phi}_m\,, \tag{4.5}$$

and

$$\Gamma_m(x,y,z) = \boldsymbol{G}\boldsymbol{\Phi}_m\,, \tag{4.6}$$

where $\boldsymbol{H}$, $\boldsymbol{B}$, and $\boldsymbol{G}$ contain only the nonzero entries of the large interpolation matrices, $\boldsymbol{H}_m$, $\boldsymbol{B}_m$, and $\boldsymbol{G}_m$.

The functional Π^u can now be approximated in the discretized domain by a functional, $\Pi^\mathrm{u}_\mathrm{d}$. Integrals over $\mathcal{V}$ are replaced by summations of the integrals taken over the individual elements. Applying this to Equation (3.22) yields

$$\begin{aligned}\Pi^\mathrm{u}_\mathrm{d} = {} & \frac{1}{2}\mathcal{C}\sum_{m=1}^{M}\int_{\mathcal{V}_m}\frac{\rho}{2}\,|\boldsymbol{\nabla}\phi_m|^2\,dV \\ & + \mathcal{C}\sum_{m=1}^{M}\int_{\mathcal{W}_m}(\boldsymbol{\nu}\cdot\hat{\boldsymbol{n}}_m)\Gamma_m\,dA + \mathcal{C}\sum_{m=1}^{M}\int_{\mathcal{W}_m}[\boldsymbol{\omega}\cdot(\boldsymbol{r}\times\hat{\boldsymbol{n}}_m)]\,\Gamma_m\,dA \\ & - \nu_T T_{\,\mathrm{req}} - \omega_x M_{x\,\mathrm{req}} - \omega_y M_{y\,\mathrm{req}}\,,\end{aligned} \tag{4.7}$$

where $\mathcal{C} = \rho B\Omega/(2\pi)$, and $\hat{\boldsymbol{n}}_m$ is the unit outward normal to element m. This is converted from a function of continuous variables to a function of *nodal* potentials by

using Equations (4.4)–(4.6), so that

$$\begin{aligned}\Pi_{\mathrm{d}}^{\mathrm{u}} &= \frac{1}{2}\sum_{m=1}^{M}\int_{\mathcal{V}_m} \boldsymbol{\Phi}_m^T \boldsymbol{B}^T \boldsymbol{\mathcal{C}}\, \boldsymbol{B}\boldsymbol{\Phi}_m \, dV \\ &\quad + \sum_{m=1}^{M}\int_{\mathcal{W}_m} (\boldsymbol{\nu}\cdot\hat{\boldsymbol{n}}_m)\boldsymbol{\mathcal{C}}\, \boldsymbol{G}\boldsymbol{\Phi}_m \, dA + \sum_{m=1}^{M}\int_{\mathcal{W}_m} [\boldsymbol{\omega}\cdot(\boldsymbol{r}\times\hat{\boldsymbol{n}}_m)]\, \boldsymbol{\mathcal{C}}\, \boldsymbol{G}\boldsymbol{\Phi}_m \, dA \\ &\quad - \nu_T T_{\mathrm{req}} - \omega_x M_{x\,\mathrm{req}} - \omega_y M_{y\,\mathrm{req}} \,. \end{aligned} \tag{4.8}$$

Note that $\boldsymbol{\Phi}_m$ is a vector of constants, so it can be taken outside of the integrals. Before taking the variation of $\Pi_{\mathrm{d}}^{\mathrm{u}}$, it is easier to rewrite the equation using several newly-defined matrices:

$$\boldsymbol{K}_m = \int_{\mathcal{V}_m} \boldsymbol{B}_m^T \boldsymbol{\mathcal{C}}\, \boldsymbol{B}_m \, dV \,, \tag{4.9}$$

$$\boldsymbol{R}_{T_m}^T = \int_{\mathcal{W}_m} (\hat{\boldsymbol{k}}\cdot\hat{\boldsymbol{n}}_m)\boldsymbol{\mathcal{C}}\, \boldsymbol{G}_m \, dA \,, \tag{4.10}$$

$$\boldsymbol{R}_{x_m}^T = \int_{\mathcal{W}_m} \hat{\boldsymbol{\imath}}\cdot(\boldsymbol{r}\times\hat{\boldsymbol{n}}_m)\boldsymbol{\mathcal{C}}\, \boldsymbol{G}_m \, dA \,, \tag{4.11}$$

$$\boldsymbol{R}_{y_m}^T = \int_{\mathcal{W}_m} \hat{\boldsymbol{\jmath}}\cdot(\boldsymbol{r}\times\hat{\boldsymbol{n}}_m)\boldsymbol{\mathcal{C}}\, \boldsymbol{G}_m \, dA \,, \tag{4.12}$$

and

$$\boldsymbol{K} = \sum_{m=1}^{M} \boldsymbol{K}_m \,, \tag{4.13}$$

$$\boldsymbol{R}_T = \sum_{m=1}^{M} \boldsymbol{R}_{T_m} \,, \tag{4.14}$$

$$\boldsymbol{R}_x = \sum_{m=1}^{M} \boldsymbol{R}_{x_m} \,, \tag{4.15}$$

$$\boldsymbol{R}_y = \sum_{m=1}^{M} \boldsymbol{R}_{y_m} \,. \tag{4.16}$$

The stiffness matrix, $\boldsymbol{K}$, is symmetric with size $N \times N$, but it is very sparse since most entries of $\boldsymbol{B}$ are zero. The vectors, $\boldsymbol{R}_T$, $\boldsymbol{R}_x$, and $\boldsymbol{R}_y$, are of size $N \times 1$. For lack of a better name, they are referred to as "right hand side" vectors. They are usually written on the right had side of an equation (except in a canonical form).

Substituting these definitions to Equation (4.8) yields

$$\begin{aligned}\Pi_{\mathrm{d}}^{\mathrm{u}} &= \frac{1}{2}\boldsymbol{\Phi}^T\boldsymbol{K}\boldsymbol{\Phi} + \nu_T\left(\boldsymbol{R}_T{}^T\boldsymbol{\Phi} - T_{\,\mathrm{req}}\right) \\ &\quad + \omega_x\left(\boldsymbol{R}_x{}^T\boldsymbol{\Phi} - M_{x\,\mathrm{req}}\right) + \omega_y\left(\boldsymbol{R}_y{}^T\boldsymbol{\Phi} - M_{y\,\mathrm{req}}\right) . \end{aligned} \tag{4.17}$$

Taking the variation of $\Pi_{\mathrm{d}}^{\mathrm{u}}$ leads to a set of three scalar equations and one matrix equation,

$$\nu_T\boldsymbol{R}_T{}^T\boldsymbol{\Phi} = T_{\,\mathrm{req}} \tag{4.18}$$

$$\omega_x\boldsymbol{R}_x{}^T\boldsymbol{\Phi} = M_{x\,\mathrm{req}} \tag{4.19}$$

$$\omega_y\boldsymbol{R}_y{}^T\boldsymbol{\Phi} = M_{y\,\mathrm{req}} \tag{4.20}$$

$$\boldsymbol{K}\boldsymbol{\Phi} = -\nu_T\boldsymbol{R}_T - \omega_x\boldsymbol{R}_x - \omega_y\boldsymbol{R}_y \tag{4.21}$$

$$= \boldsymbol{R} . \tag{4.22}$$

These can be rewritten in a canonical form,

$$\begin{bmatrix} \boldsymbol{K} & \boldsymbol{R}_T & \boldsymbol{R}_x & \boldsymbol{R}_y \\ \boldsymbol{R}_T{}^T & 0 & 0 & 0 \\ \boldsymbol{R}_x{}^T & 0 & 0 & 0 \\ \boldsymbol{R}_y{}^T & 0 & 0 & 0 \end{bmatrix} \begin{Bmatrix} \boldsymbol{\Phi} \\ \nu_T \\ \omega_x \\ \omega_y \end{Bmatrix} = \begin{Bmatrix} 0 \\ T_{\,\mathrm{req}} \\ M_{x\,\mathrm{req}} \\ M_{y\,\mathrm{req}} \end{Bmatrix} . \tag{4.23}$$

Thus, the finite element discretization has reduced the minimization of the Π functional to the solution of a large set of first order, linear equations.

4.1.2 Boundary Conditions

Although they are not clearly displayed as in Equation (3.33), the natural boundary conditions have been implicitly incorporated into Equation (4.21) by the integrals that form the $\boldsymbol{R}$ vector. Thus, they will form part of the solution and need not be discussed further.

In contrast, the essential boundary conditions, Equations (3.2)–(3.5), have not yet

been discussed. By imposing the essential boundary conditions, the stiffness matrix becomes positive definite and thus full rank. In theory, then, Equation (4.22) has a unique solution and it can be solved.

The most obvious way of taking care of the essential boundary conditions is to condense out the known nodal potential values. If, for example, Φ at node 32 is known to equal $\bar{\Phi}$, then the equation corresponding to row 32 of $\boldsymbol{K}$ and $\boldsymbol{R}$ is superfluous. It is dropped from the equation set. Column 32 of $\boldsymbol{K}$ is then multiplied by $\bar{\Phi}$ and the information is subtracted from $\boldsymbol{R}$. Thus, if the potential is known at e nodes, then $\boldsymbol{K}$ is reduced to size $(N-e)\times(N-e)$.

Unfortunately, the condensation method requires a great deal of programming to implement. Instead, a penalty weighting method is employed. The cost functional is effectively augmented by weightings on squared quantities of the potential at the nodes with essential boundary conditions. If, again, Φ at node 32 is know to equal $\bar{\Phi}$, then

$$\Pi_{\mathrm{d}}^{\mathrm{u}} = \text{as before} \quad + \frac{1}{2}\left(\Phi_{32} - \bar{\Phi}\right)^T g\left(\Phi_{32} - \bar{\Phi}\right) ,$$

where g is a large scalar number such that $g \gg \max\{K_{ij}\}$. Now, instead of solving Equation (4.22), the solution is found by solving

$$\left(\boldsymbol{K} + \boldsymbol{\Delta K}_{\mathrm{BC}}\right)\boldsymbol{\Phi} = \boldsymbol{R} + \boldsymbol{\Delta R}_{\mathrm{BC}} ,$$

where $\boldsymbol{\Delta K}_{\mathrm{BC}}$ is a matrix of zeros except at location (32,32), which equals g, and $\boldsymbol{\Delta R}_{\mathrm{BC}}$ is a vector of zeros except for the 32nd entry, which equals $g\bar{\Phi}$. The weighting, g, is large enough to make the other elements in row 32 of $\boldsymbol{K}$ be negligible. Then, to an arbitrary numerical accuracy, $\Phi_{32} = \bar{\Phi}$.

This method is also used to enforce the periodicity boundary conditions. If node a is the same as node b, then $\frac{1}{2}(\Phi_a - \Phi_b)^T g(\Phi_a - \Phi_b)$ is added to the cost functional. The effect on $\boldsymbol{K}$ is that four entries are adjusted by g, while $\boldsymbol{R}$ is left alone. Effectively, the equation in row a then requires that $\Phi_a - \Phi_b \approx 0$, and row b requires that $-\Phi_a + \Phi_b \approx 0$.

4.1.3 Usage

When examining a solution found via the finite element method, it should be recognized that it has limitations. The finite element solution will not exactly solve Laplace's Equation (3.32). Laplace's equation, for an incompressible fluid flow, should be interpreted as a statement of continuity: At every point, the net fluid flux must be zero; there are no sources nor sinks. For the exact solution, this condition will hold at every point in $\mathcal{V}$ that is not on the wake sheet. For the finite element solution, this condition is successfully satisfied at every node not on $\mathcal{W}_\mathrm{d}$ and also, in an integral sense, by each individual element. However, for points inside the elements, the potential values must be interpolated, and they do not fulfill the continuity conditions.

As derived so far, the canonical form, Equation (4.23), can be used to solve the unconstrained optimal rotor problem. The equation would be solved directly (via LU decomposition or any other standard method) for the four unknowns (three independent Lagrange multipliers and one dependent velocity potential). However, this will not be possible once the maximum local lift constraints are introduced. Therefore, an alternate solution procedure is employed which can be used to solve the constrained problem. For the alternative procedure, Equation (4.21) will be solved three times. Each solution, for different, arbitrary thrust and moment conditions, will yield one third of the information necessary to solve for the correct Lagrange multipliers.

First, Equation (4.21) would be solved by setting $\nu_T = 1$, $\omega_x = 0$, and $\omega_y = 0$. This would yield a solution, $\mathbf{\Phi}_T$, and a set of generalized forces (thrust and moments) which are placed in a matrix of force coefficients: $T_{11} = T$, $T_{21} = M_x$, and $T_{31} = M_y$.

Second, Equation (4.21) would be solved by setting $\nu_T = 0$, $\omega_x = 1$, and $\omega_y = 0$. This would lead to a second solution, $\mathbf{\Phi}_x$, and a second set of generalized force coefficients. This procedure is repeated a third time. Combining the information from these three solutions produces a 3×3 matrix equation,

$$\begin{bmatrix} & & \\ & T_{ij} & \\ & & \end{bmatrix} \begin{Bmatrix} \nu_T \\ \omega_x \\ \omega_y \end{Bmatrix} = \begin{Bmatrix} T_{\,\mathrm{req}} \\ M_{x\,\mathrm{req}} \\ M_{y\,\mathrm{req}} \end{Bmatrix}, \tag{4.24}$$

where $[T_{ij}]$ is the matrix of force coefficients. This equation can then be solved for the correct Lagrange multipliers under any desired trim conditions. The final velocity potential is a linear combination of the three previous solutions

$$\mathbf{\Phi} = \nu_T \mathbf{\Phi}_T + \omega_x \mathbf{\Phi}_x + \omega_y \mathbf{\Phi}_y \,. \tag{4.25}$$

Given the nodal potential distribution, $\mathbf{\Phi}$, the circulation distribution can be found using Equation (3.4). Finally, the lift distribution can be found using the Kutta-Joukowski theorem.

4.2 Constrained Optimization of Rotor Circulation

The extension of the finite element program include the $C_{l_{\max}}$ constraints follows the discussion in Section 3.3.2. Recalling the Lagrange multiplier defined by Equation (3.45), this definition can be rewritten as

$$\vartheta \left(\Gamma - \Gamma_{\max} \right) = 0 \,. \tag{4.26}$$

The natural boundary condition, Equation (3.44), requires that the velocity and, hence, the circulation are a function of ϑ. This means that Equation (4.26) is actually a *quadratic* equation in ϑ. Nonlinear systems of equations of this size are not practical to solve directly. Instead, an iterative search procedure using augmented Lagrangians will be employed.

Using an iterative technique leads to a further task. Exactly which nodes need to be constrained must be determined with each iteration. The problem is not trivial. For example, if an unconstrained optimal solution has unrealistically high local lifts around $(\bar{r}, \psi) = (0.7, 270°)$, then that area should be constrained, *i.e.*, the lift pushed down in the next iteration. However, because a desired total level of thrust must be maintained, pushing down at $(0.7, 270°)$ will force other areas to compensate and

raise their local lifts. In this case, the solution for the second iteration would have a lower lift at $(0.7, 270°)$, but might have higher lifts at $(0.8, 250°)$ and $(0.8, 290°)$. If these two locations have local lifts which violate the $C_{l_{\max}}$ constraints, then they will be added to the constraint set for the next iteration. In addition, the first point, $(0.7, 270°)$, should be reexamined to ensure that it was not pushed down too far. If it was pushed down too far, then its constraint should be relaxed. Thus, the points in the constraint set change with each iteration. Augmented Lagrangians will provide the sensitivity information needed to update the constraint set every iteration.

Essentially, augmented Lagrangians combine some of the aspects of traditional Lagrange multipliers with penalty weighting methods. Consider a traditional Lagrange multiplier which is applied to a function, f, with an inequality constraint $f \leq f_{\max}$. The Lagrange multiplier is nonzero when the constraint is not violated ($f < f_{\max}$), and it equals zero when f is on the constraint boundary ($f = f_{\max}$). The Lagrange multiplier is not defined (or even considered) for the case of $f > f_{\max}$, because this is not a valid solution of the problem. In this respect, augmented Lagrangians differ from traditional Lagrange multipliers. Techniques using augmented Lagrangians are similar to penalty weighting methods. Functions in violation of their constraints approach their constraint boundaries, but *from the procscribed side.* Both penalty methods and procedures using augmented Lagrangians weight the square of the difference between a function and the constraint boundary, to bring the function closer to the boundary. However, augmented Lagrangians cause other terms to be added to the cost function. The additional terms will decrease the distance between the function and its constraint boundary with every iteration. Thus, final solutions using the augmented Lagrangian method *will* have points which are in violation of the constraints, but only by an arbitrarily small error.

Recall the cost functional used in the finite element discretization, Equation (4.17). For the constrained problem, this is augmented by several additional functions, so that

$$\Pi_{\mathrm{d}} = \Pi_{\mathrm{d}}^{\mathrm{u}} + \boldsymbol{\beta}^T \boldsymbol{A} \left(\boldsymbol{\Gamma} - \boldsymbol{\Gamma}_{\max} \right) + g_2 P_2 + g_3 P_3 \,, \tag{4.27}$$

and the new terms are to be defined. Here, g_2 and g_3 are positive valued penalty weights. The vector, $\boldsymbol{\beta}$ contains the augmented Lagranians, β_j, for each node j. Also, $\boldsymbol{A}$ is a diagonal matrix, whose entries are the average wake sheet surface areas of the elements around each node. Lastly, P_2, and P_3 are quadratic, scalar penalty functions.

So far, the constraint set has not been precisely defined. Points in the constraint set are those in violation of Equation (3.36). The set is subdivided into C_a and C_b, where

$$\begin{aligned} C_a &= \{j \mid \beta_j > 0\} \\ &= \text{the set of nodes that were previously} \\ &\quad \text{in the constraint set and will stay in constraint set,} \end{aligned} \tag{4.28}$$

and

$$\begin{aligned} C_b &= \left\{ j \,\middle|\, \beta_j = 0, \Gamma_j \geq \Gamma_{\max_j} \right\} \\ &= \text{the set of nodes that are being added} \\ &\quad \text{to the constraint set.} \end{aligned} \tag{4.29}$$

The penalty functions can now be precisely defined as,

$$P_2 = \sum_{j \in C_a} A_j \left(\Gamma_j - \Gamma_{\max_j} \right)^2 , \tag{4.30}$$

and

$$P_3 = \sum_{j \in C_b} A_j \left(\Gamma_j - \Gamma_{\max_j} \right)^2 . \tag{4.31}$$

It should be noted that this is an iterative procedure, so Equation (4.27) is implicitly the cost functional for the current iteration only. The variation of Π_{d} can be taken by substituting in the definitions for P_2 and P_3, and noting that w_2 and w_3 are

constants. This yields

$$\begin{aligned}\delta\Pi_{\mathrm{d}} &= \delta\Pi_{\mathrm{d}}^{\mathrm{u}} \\ &\quad + \sum_{j\in C_a}\left[\beta_j + 2g_2\left(\Gamma_j - \Gamma_{\max_j}\right)\right] A_j\,\delta\Gamma_j + \sum_{j\in C_a}\left(\Gamma_j - \Gamma_{\max_j}\right) A_j\,\delta\beta_j \\ &\quad + \sum_{j\in C_b} 2g_3\left(\Gamma_j - \Gamma_{\max_j}\right) A_j\,\delta\Gamma_j\,. \end{aligned} \tag{4.32}$$

Assuming that $g = g_2 = g_3$, then this can be simplified to a convenient matrix form

$$\begin{aligned}\delta\Pi_{\mathrm{d}} &= \delta\Pi_{\mathrm{d}}^{\mathrm{u}} + \delta\boldsymbol{\beta}^T\boldsymbol{A}\left(\boldsymbol{\Gamma} - \boldsymbol{\Gamma}_{\max}\right) \\ &\quad + \delta\boldsymbol{\Gamma}^T\boldsymbol{A}\left[\boldsymbol{\beta} + 2g\left(\boldsymbol{\Gamma} - \boldsymbol{\Gamma}_{\max}\right)\right]\,. \end{aligned} \tag{4.33}$$

Furthermore, recalling that $\boldsymbol{\Gamma} = \boldsymbol{G\Phi}$ and rearranging terms reveals that

$$\begin{aligned}\delta\Pi_{\mathrm{d}} &= \delta\Pi_{\mathrm{d}}^{\mathrm{u}} + \delta\boldsymbol{\beta}^T\boldsymbol{A}\left(\boldsymbol{\Gamma} - \boldsymbol{\Gamma}_{\max}\right) \\ &\quad + \delta\boldsymbol{\Phi}^T\boldsymbol{G}^T\boldsymbol{A}\left[\boldsymbol{\beta} - 2g\boldsymbol{\Gamma}_{\max}\right] + 2g\delta\boldsymbol{\Phi}^T\boldsymbol{G}^T\boldsymbol{AG\Phi}\,. \end{aligned} \tag{4.34}$$

As before, requiring that the first variation equals zero reveals a set of equations. In the canonical form, they are

$$\begin{bmatrix} \boldsymbol{K} + 2g\boldsymbol{G}^T\boldsymbol{AG} & \boldsymbol{R}_T & \boldsymbol{R}_x & \boldsymbol{R}_y \\ \boldsymbol{R}_T{}^T & 0 & 0 & 0 \\ \boldsymbol{R}_x{}^T & 0 & 0 & 0 \\ \boldsymbol{R}_y{}^T & 0 & 0 & 0 \end{bmatrix} \begin{Bmatrix} \boldsymbol{\Phi} \\ \nu_T \\ \omega_x \\ \omega_y \end{Bmatrix} = \begin{Bmatrix} \boldsymbol{G}^T\boldsymbol{A}\left[2g\boldsymbol{\Gamma}_{\max} - \boldsymbol{\beta}\right] \\ T_{\mathrm{req}} \\ M_{x\,\mathrm{req}} \\ M_{y\,\mathrm{req}} \end{Bmatrix}. \tag{4.35}$$

The additional equation found by requiring that $\delta\Pi_{\mathrm{d}} = 0$ independent of $\delta\boldsymbol{\beta}^T$ leads to conditions on each β_j identical to those on ϑ in Equation (3.45). These conditions will be fulfilled *a priori*, due to the definition of $\boldsymbol{\beta}$.

The trim conditions, Equations (4.18)–(4.20) remain as before, but it is clear that instead of solving Equation (4.22), a modified equation must be solved. Now

$$\left(\boldsymbol{K} + \boldsymbol{\Delta K}\right)\boldsymbol{\Phi} = \boldsymbol{R} + \boldsymbol{\Delta R}\,, \tag{4.36}$$

where

$$\boldsymbol{\Delta K} = 2g\boldsymbol{G}^T\boldsymbol{A}\boldsymbol{G}\,, \tag{4.37}$$

and

$$\boldsymbol{\Delta R} = 2g\boldsymbol{G}^T\boldsymbol{A}\boldsymbol{\Gamma}_{\max} - \boldsymbol{G}^{\mathbf{T}}\boldsymbol{A}\boldsymbol{\beta}\,. \tag{4.38}$$

Like the imposition of periodic essential boundary conditions, this causes the $\boldsymbol{\Delta K}$ matrix to have four nonzero entries and the $\boldsymbol{\Delta R}$ vector to have two nonzero entries for each actively constrained node. Say, for example, that node j was to be constrained and that $\phi_j - \phi_{j+J} = \Gamma_j$, then

$$[\boldsymbol{\Delta K}] = \begin{array}{r} \\ \text{row } j \rightarrow \\ \\ \text{row } j+J \rightarrow \\ \end{array} \begin{array}{c} \downarrow \text{column } j \qquad \downarrow \text{column } j+J \\ \left[\begin{array}{ccccc} & \vdots & & \vdots & \\ \cdots & 2gA_j & \cdots & -2gA_j & \cdots \\ & \vdots & & \vdots & \\ \cdots & -2gA_j & \cdots & 2gA_j & \cdots \\ & \vdots & & \vdots & \end{array}\right] \end{array}\,, \tag{4.39}$$

and

$$\{\boldsymbol{\Delta R}\} = \left\{\begin{array}{c} \vdots \\ 2gA_j\Gamma_{\max_j} - A_j\beta_j \\ \vdots \\ -2gA_j\Gamma_{\max_j} + A_j\beta_j \\ \vdots \end{array}\right\}\,. \tag{4.40}$$

The constrained optimal problem requires solving the set of Equations (4.35) for the unknowns $\boldsymbol{\Phi}$, ν_T, ω_x, ω_y, and now $\boldsymbol{\beta}$. The penalty weight, g, is a constant which is arbitrarily chosen beforehand such that $g > K_{ij\,\max}$. So far, no explanation has been given as to how C_a and C_b are found or as to how the augmented Lagrangians, β_j, are sized. This will become clear as the iterative procedure is explained.

The entire optimization routine has been implemented in a computer program known as CORC (Constrained Optimization of Rotor Circulation). Overall, it consists of an iterative constraint update procedure wrapped around the previously described

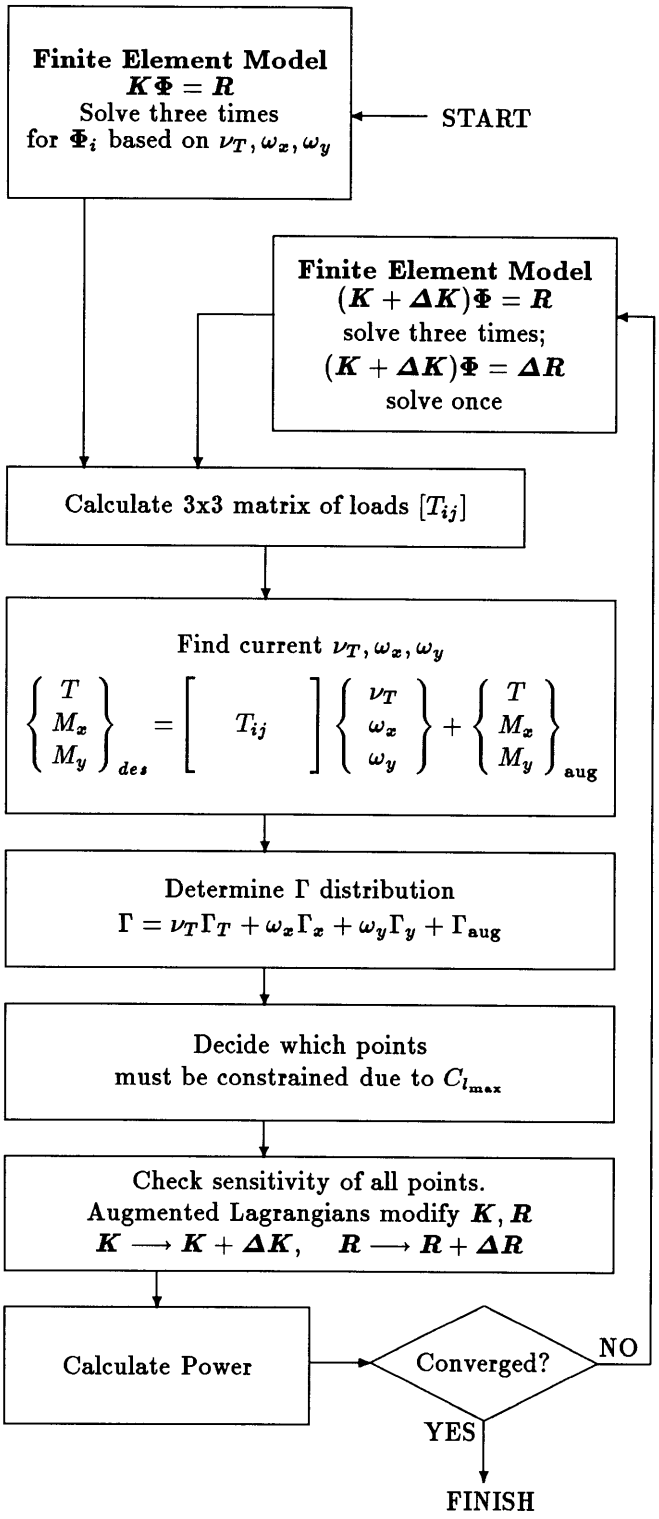

Figure 4-1: Flowchart of the CORC procedure.

finite element solver. As shown in the flowchart of Figure 4-1, the CORC routine begins by solving the unconstrained optimal problem. As previously discussed in Section 4.1.3, this yields a 3×3 matrix of loads, $[T_{ij}]$, which is used to solve for the three trim Lagrange multipliers. At this point, because it is only the initial iteration, all of the augmented Lagrangians, β_i, are set to zero, and all augmented terms (denoted $(\cdot)_{\text{aug}}$) are still set to zero. The unconstrained solution is then examined to see which points violate the $C_{l_{\max}}$ constraint. Points that violate the constraint are put into C_b. This new constraint set allows formation of a new cost functional, Π_{d}, a $\boldsymbol{\Delta K}$ matrix, and a $\boldsymbol{\Delta R}$ vector.

The procedure now wraps back to the finite element solver to begin the second iteration. As before, three solutions are required, corresponding to the three trim Lagrange multipliers. However, now a fourth solution is required for the effects of $\boldsymbol{\Delta R}$. The first three solutions can be thought of as homogeneous solutions and the fourth as a particular solution to the problem.

The first three equations to solve are of the form

$$(\boldsymbol{K} + \boldsymbol{\Delta K})\,\boldsymbol{\Phi} = -\nu_T \boldsymbol{R}_T - \omega_x \boldsymbol{R}_x - \omega_y \boldsymbol{R}_y\,, \tag{4.41}$$

and the fourth equation is

$$(\boldsymbol{K} + \boldsymbol{\Delta K})\,\boldsymbol{\Phi} = \boldsymbol{\Delta R}\,. \tag{4.42}$$

Of course, both Equations (4.41) and (4.42) must be numerically adjusted to impose the essential boundary conditions before solving (see Section 4.1.2). Equation (4.42) yields a set of forces and moments denoted as $\begin{bmatrix} T & M_x & M_y \end{bmatrix}^T_{\text{aug}}$.

After finding the four potential solutions, the updated circulation distribution is formed. This constrained solution is then checked against the $C_{l_{\max}}$ constraints. The sensitivity of points in C_a is checked to see whether the constraints should be further tightened or released. This is done using the augmented Lagrangians, according to

the following rule:

$$\beta_j^{\text{new}} = \begin{cases} \beta_j^{\text{old}} + 2g\left(\Gamma_j - \Gamma_{\max_j}\right) , & \text{if } \beta_j^{\text{old}} + 2g\left(\Gamma_j - \Gamma_{\max_j}\right) > 0 \\ 0 , & \text{otherwise.} \end{cases} \tag{4.43}$$

When β_j is set to zero, node j is simultaneously released from the constraint set, that is, $j \notin (C_a \cup C_b)$.

At this point, the induced power is calculated. If the percentage change in the induced power since the previous iteration is below a certain tolerance, then the procedure is finished. Otherwise, the new $\boldsymbol{\Delta K}$ and $\boldsymbol{\Delta R}$ are calculated with the updated constraint set and the program loops back to the finite element solver for the next iteration.

4.3 Power Calculations

There are two ways to calculate the induced power given the optimal rotor circulation distribution. As discussed in Sections 2.4 and 2.5, a near wake analysis would first calculate the induced velocity at the disk using a separate vortex lattice code with equation (2.28) and then calculate the induced power using equation (2.26).

However, a far wake analysis provides an easier calculation because it does not require any separate program beyond what is already incorporated into the finite element code. Recalling the derivation of the far wake induced power calculation in Section 3.2.2, it is evident that accurate knowledge of the velocity potential *gradient* is needed. Fortunately, that is exactly what the finite element obtains with the interpolation functions in the matrix $\boldsymbol{B}$, *i.e.*, $\boldsymbol{\nabla}\phi_m = \boldsymbol{B}\boldsymbol{\Phi}_m$. In fact, this information is already implicitly calculated in the stiffness matrix (see equations (4.9) and (4.13)). The induced power from the finite element solution is seen to be

$$P_{\text{i}} = \frac{1}{2}\boldsymbol{\Phi}^T\boldsymbol{K}\boldsymbol{\Phi} . \tag{4.44}$$

This calculation is performed at the end of every iteration of the CORC routine.

It can be shown that, for the type of finite element analysis used here, the numerical stiffness matrix is always overly stiff [4, Section 4.2.5]. This follows from an examination of how the finite element solution converges as the number of elements in a model is increased. It also leads to an interesting conclusion that *the induced power calculated in* (4.44) *will always be higher than the exact answer.*

At first glance, the reader might expect that the induced power should converge from below the exact solution. A quick explanation for this can be found by drawing the analogy to a finite element (or a Rayleigh-Ritz) analysis for a static problem in elasticity. In the case of an elastic member subjected to a given load, a finite element analysis will underpredict the strain energy, because the member's stiffness is too high. However, if a given *displacement* is enforced, rather than a given load, then the calculated energy will be too great. In the case of the rotor, the problem is effectively one of applied displacement rather than applied load. The trim conditions require that a certain level of circulation be attained and this translates to a certain velocity potential, so it is ϕ that is effectively applied, rather than a given right hand side vector. Merely solving equation (4.22) or (4.36) with arbitrary trim Lagrange multipliers is equivalent to an applied force problem. However, using the Lagrange multipliers in equation (4.25) (or the constrained problem equivalent) to adjust the $\mathbf{\Phi}$ solutions makes it equivalent to a problem of applied displacement.

4.4 Model Geometry

In complicated finite element work, it is not unusual to spend more time refining and selecting the proper mesh than producing and analyzing results. The accuracy of the final results is entirely dependent upon choosing the geometry of the mesh to be fine enough to represent all important features in the system. Unfortunately, a trade-off must be made between accuracy and cost. For a model with N nodes, the $\boldsymbol{K}$ matrix size and hence the computational cost are proportional to N^3. This provides a strong incentive to be as selective as possible when choosing where and how to increase the number of nodes. Varying element size, location, and density is often referred to as h

refinement.

A second, but highly coupled, problem facing the analyst is the choice of element type. Element type is essentially determined by the order of the interpolating polynomials used within each element. Higher order elements possess more interelement continuity in their derivatives; they can also represent more complex shapes and solutions inside each element than can lower order elements. To represent an nth order polynomial interpolation function requires, essentially, $n+1$ nodes in each linear dimension of the element. Thus, when changing the order of an interpolation function, not only do the functions inside the $\boldsymbol{H}$ and $\boldsymbol{B}$ matrices change (see Section 4.1.1), but also the size of the matrices changes, making this a non-trivial programming decision. This type of analysis is usually referred to as p refinement.

As discussed in Section 3.2.1, the geometry of the control volume $\mathcal{V}_\mathrm{d}$ is a wide, skewed, helical ribbon with a small but finite thickness. For the flight conditions of interest, say $\mu = 0.25$, the angle between horizontal ($\hat{\boldsymbol{\imath}}$) and the wake translation direction ($\hat{\boldsymbol{\tau}}$) is approximately 172°. This causes large distortions in elements. Boundary elements at the top or bottom of the mesh are particularly affected by the skew. These are, of course, the elements which are directly used to calculate the circulation. Distortions in an element's shape cause it to be too stiff, thus making the power calculation inaccurate. Dealing with these skew effects is the primary difficulty faced in trying to solve the optimal rotor equations.

For the model implemented in the CORC routine, the boundary nodes on $\mathcal{W}_\mathrm{d}$ are placed in a logically rectangular array based on a radial and azimuthal coordinate system. Looking much like the spokes on a bicycle wheel, a radial spacing pattern for the nodes is chosen, then this pattern is laid down at each desired azimuth. The entire array repeats at each desired intervals in the $\hat{\boldsymbol{\tau}}$ direction.

There are several reasons for using this fixed nodal array. Most important is the need to enforce periodicity in the system. For instance, nodes on $\mathcal{S}_{\mathrm{d}_{2\pi}}$ must be in the same relative location as those on $\mathcal{S}_{\mathrm{d}_0}$ so that they can be set equal. This is particularly relevant to those points on the wake sheet surface. In order to calculate the bound circulation, Equation (3.4) must have the nodes in the same relative locations

on the rotor disk.

Aerodynamic considerations provide a second reason to keep the nodes in a regular array. On real blades, the radial lift and circulation should roll off to zero at the tips, proportional to $\sqrt{R-r}$. Correctly modeling a square root distribution with a piecewise continuous distribution is difficult because the slope must be infinite at the tips. An effective way to approximate it is to space the nodes in the cosine pattern of Equation (2.8). For rotors, this rolloff occurs both at the blade tip and at the blade root, so a cosine pattern is centered on the blade surface and nodal density increases toward the tip and root. In addition, the wake inside the root cutout and beyond the blade tips is also given a radial cosine distribution, with the nodal spacing continually increasing with the distance from the blade.

The final reason to use a regular nodal array is simplicity. The velocity potential is known most accurately at the nodes. Information for points inside an element must be interpolated so it is less accurate and should be avoided if possible. Having points on a regular (r, ψ) grid means that an *entire* radial lift distribution is known at discrete points in time, *i.e.*, at each given azimuthal station. This makes the evaluation of the near wake integrals (Section 2.4) simple and accurate.

Although having a regular array of nodes is highly desirable for analysis, it restricts the analyst's ability to refine the mesh for greater accuracy. Higher order elements are not significantly better at modeling highly skewed geometries than linear elements. Therefore, in the CORC program, only h refinement was investigated. Trilinear, hexahedral, isoparametric elements were used exclusively. Each element possessed 8 nodes, which meant that each $\boldsymbol{K}_m$ matrix had 64 nonzero elements and $\boldsymbol{R}_T$, $\boldsymbol{R}_x$, and $\boldsymbol{R}_y$ had 8 nonzero entries each. Also, trilinear implies that while the finite element velocity potential solution is continuous across elements, the velocity is discontinuous across the element boundaries.

In general, nodes must be concentrated where the potential is varying rapidly, or the solution will not be accurately represented. In physical terms, this implies that nodes should be concentrated where the potential gradient, and, hence, the kinetic energy, is expected to be large. For the rotor wake, clearly, the energy will be highest

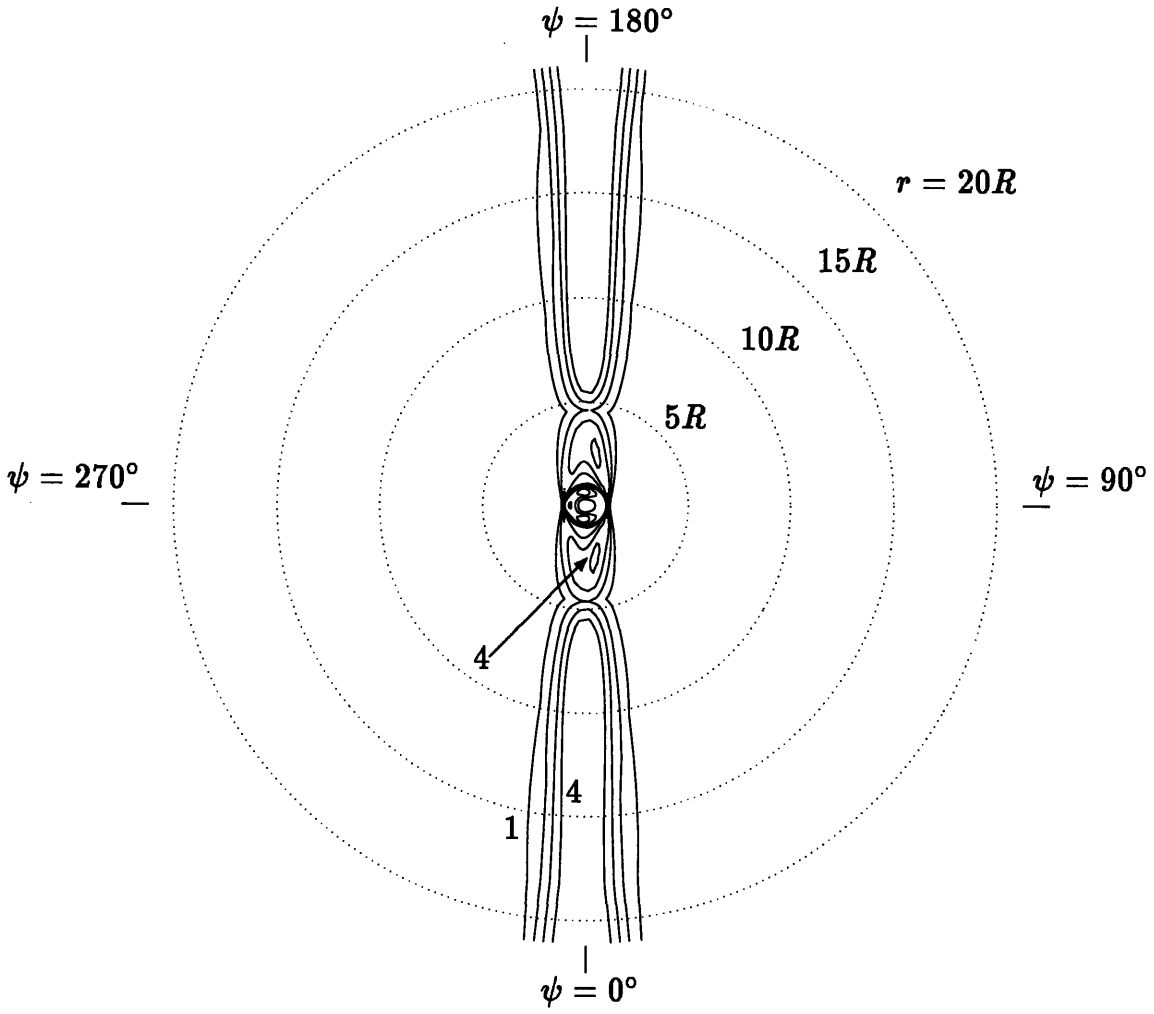

Figure 4-2: An approximate measure of how energy is distributed in the flow. Shown are contours of $\hat{E}(\frac{2\pi}{\Omega})^2/(\rho R^5)$ where $\hat{E} = \int_{\mathcal{S}_1}^{\mathcal{S}_u} \frac{1}{2}\mathbf{\Phi}^T \boldsymbol{K} \mathbf{\Phi}\, d\hat{\tau}$. Contour labels are $\times 10^8$.

at the wake sheet, particularly at the blade tips. A fine nodal density is achieved at the tips by using the previously described, radial cosine spacing. In addition, a cosine distribution is used in the $\hat{\tau}$ direction. This concentrates elements at the wake sheet surfaces. If the wake were not skewed (as in the case of vertical flight) then these steps would be enough to ensure an accurate solution.

Physically, the high skew angle arises because the helicopter is moving forward horizontally at a much greater rate than the wake is travelling downwards. Most of the energy in the flow which lies outside of the wake tube is concentrated in the fore and aft sections of the wake. Figure 4-2 is a contour plot of an approximate

energy measure in the flow. The model used to generate this figure is not considered reliable enough for power calculations, so specific values of the contour lines are not of particular importance. However, the plot is certainly useful for showing the general nature of the energy in the flow. The wake tube appears as a small circle piercing the plot in the center. The contour lines are very dark around the tube because of the high energy gradients there. The maximum contour level in the wake tube, other than at the blade tips, is 3.0. Notice how rapidly the relative energy level falls off to the left or right of the rotor's line of travel. Clearly, the plot demonstrates that, in a horizontal plane, the energy extends out fore and aft very far from the wake tube. Lastly, it should be noted that the discontinuities occurring near $r = 5R$ in the fore and aft regions are purely an artifact of the finite element mesh geometry.

To reduce the effects of the skew, distorted elements which would naturally have a significant amount of kinetic energy must be straightened out. One way to straighten out the elements in a particular region is to concentrate more nodes in that region. The new nodes can be added in such a way that the elements are less skewed. Following this line of reasoning, one method which was investigated, but eventually rendered unnecessary, was the use of a finer azimuthal spacing near 0° and 180°.

The most significant step taken to alleviate skew distortions was to modify the shape of $\mathcal{V}_\mathrm{d}$. As Figure 4-2 showed, the majority of the flow is concentrated in the fore and aft regions of the wake. If no steps are taken to alleviate the skew, then the flow encounters the face of the element on $\mathcal{S}_{\mathrm{d}_\mathrm{u}}$ at a highly oblique angle, making the calculation the flux across the surface inaccurate. However, if the control volume in the fore and aft regions is extended perpendicularly to the wake tube axis, $\hat{\boldsymbol{\tau}}$, then the faces of the elements will face directly into the predominant direction of the flow. Therefore, the surface of the control volume is made to bend away from the axis of the rotor blade immediately outside the blade radius. The angle at which the mesh bends away from the blade axis varies as $\cos\psi$, so the control volume is not modified at $\psi = 90°$ and $\psi = 270°$. The shape of $\mathcal{V}_\mathrm{d}$ lying inside the wake tube was not modified, because of the utility of the regular, rectangular array over $\mathcal{W}_\mathrm{d}$. A conceptual view of the new, discretized control volume is pictured in Figure 4-3. Here, the volume

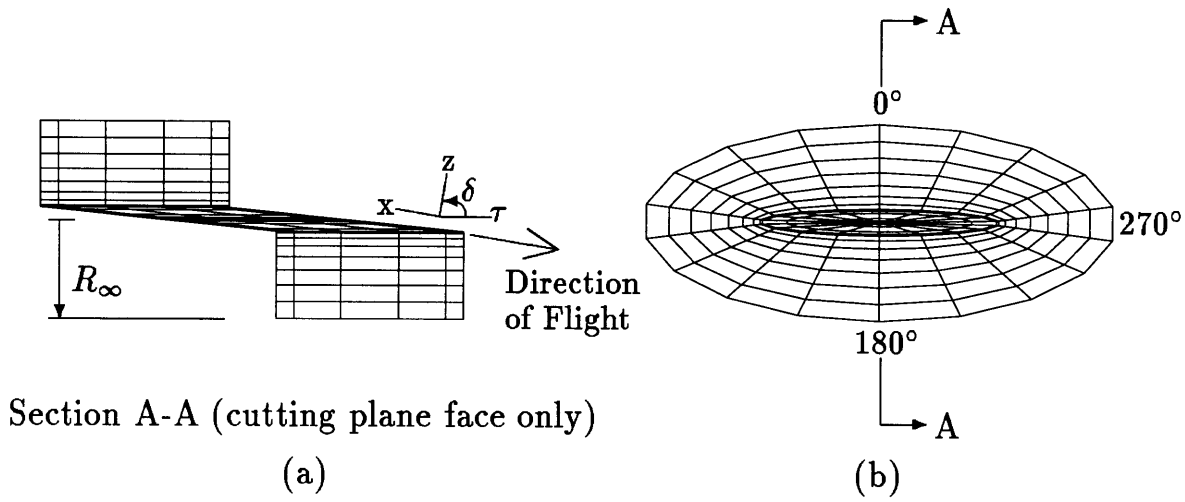

Figure 4-3: Anti-skew mesh. (a) right hand side, (b) front

corresponding to all the blade passages is drawn, rather than just the volume between two consecutive blades. In part (a) of the figure, the conceptual domain is seen from the helicopter's right side. The volume inside the wake tube is contained in the middle region, which appears to be a parallelogram from this perspective. Points outside the rotor disk, but still affected by the flow, surround the wake tube and prominently appear as rectangles. A view from above the rotor disk, looking along the flight path direction, is shown in figure (b). The domain looks like an elliptical cylinder. The rotor disk also appears elliptical because it is seen at an angle.

Use of this anti-skew mesh has the benefit of reducing the number of nodes needed for a given domain size, R_∞. If the mesh had not extended perpendicularly to $\hat{\tau}$, but had instead remained parallel to the rotor disk plane, the number of elements would have to increase by a factor of $1/\cos\delta$.

It should be noted that this change in geometry does not change any of the periodicity boundary conditions on ϕ. The surfaces $\mathcal{S}_{d_{2\pi}}$, $\mathcal{S}_{d_u}$, etc., still maintain their relations to one another and $\mathcal{V}_d$ can still conceptually stack like a split washer.

In practice, the anti-skew mesh proved to decrease solution time in the finite element routine by 25% or more compared to similarly sized meshes that did not bend the domain outside of the wake tube. This indicates that the new $\boldsymbol{K}$ matrix was much better conditioned. More importantly, the better conditioning is also manifested in

the power calculation, which showed a better than 3% decrease in computed induced power for a given set of flight conditions.

After extensive testing, the mesh settled upon for use in the CORC routine had 77 radial, 61 azimuthal, and 29 vertical nodes. The azimuthal positions were spaced evenly throughout the array. The radial distribution had 6 points inside the root cutout, 23 over the blade surfaces, and 48 nodes spread between the blade tip and R_∞. Along the y axis, R_∞ was set to $7.63R$, which was found to be significantly far enough away from the rotor that it did not affect the flow.

4.5 Computer Usage

The CORC routine was implemented in FORTRAN, on a Cray X-MP supercomputer. For the model size chosen, it required 21 megawords of memory, not including the linear algebra solver package. The solver package used was the Sparse Linear Algebra Package (SLAP) [34]. The SLAP routine mated well with the finite element program because it was designed for use with sparse, positive definite matrices. It employed a conjugate gradient method to solve Equation (4.36).

Each solution of the finite element routine took on the order of 28 minutes of system CPU time. Either three or four finite element solutions were required for each iteration of the CORC routine. The time required for finite element assembly, setting up and checking the constraints, etc. was negligible compared to the time required to solve the $N \times N$ system of equations. Convergence of the outer iterations was quick and usually took only 1 unconstrained iteration followed by 2 constrained iterations before a final solution was reached. More will be said about convergence and the performance of the augmented Lagrangians in Section 5.1.

Chapter 5

Results

The primary goal of this research is to find rotor lift distributions which will require the minimum induced losses. Now that the optimization theory and solution procedures have been discussed, several optimal distributions can be presented. They will be compared to the lift distribution for a typical, non-optimal rotor. Furthermore, a brief study of how the number of blades affects the optimal solution will be made.

Because the optimal solutions are generated from a numerical routine, and no analytical solutions for the optimal rotor exist, it is important to establish that the program functions properly before producing results. The program is checked against degenerate optimal cases, for which analytical results exist. Also, internal checks can be performed to make sure that the constraints are properly applied. This validation effort is the first topic of the chapter.

5.1 Validation of the Numerical Routine

The CORC computer routine consists of two entities. The first is the finite element routine; a demonstration that this component works means that all of the matrices discussed in Chapter 4 have been set up properly, the boundary conditions are applied correctly, and the mesh has the required accuracy. The second half of the CORC program is the constraint updating procedure; satisfactory elimination of the points in violation of the constraints effectively demonstrates that this procedure functions

properly.

5.1.1 Tests of the Finite Element Routine

In axial flight, the rotor experiences an axisymmetric velocity field, so there is no lift deficit due to a retreating side. Because of this, there is no need to apply the maximum local lift constraints and the finite element subroutines can be tested without the usual constraint update procedures. Also, in axial flight, the optimal rotor theory presented in Section 3.3.1 reduces to the classical case of a minimum induced loss propeller. This solution is well understood and can be numerically computed using Goldstein's [12] method. Physically, propellers differ from rotors in hover because propellers have a high axial advance speed compared to their wake displacement speed, while rotors have zero axial advance speed. A rotor in a vertical climb does have an axial advance rate, but not as high as is common for propellers. Nevertheless, in the far wake, the problems are equivalent if the wake geometry, as defined by the vertical advance ratio λ, and the desired thrust coefficient C_T are the same.

A test case was run for a four bladed rotor at a vertical advance ratio of $\lambda = 0.0775$. The Goldstein solution for the bound circulation on a blade is shown as the solid line in Figure 5-1. The finite element program was tested with meshes of two different nodal densities, the standard mesh derived in Section 4.4 and a mesh with identical geometry but using only every other node. The bound circulation for these cases is also plotted in Figure 5-1. The two finite element solutions lie virtually on top of each other and both are almost indistinguishable from the Goldstein solution.

A measure of efficiency was also computed for the three cases. In the limit of the rotor acting like a perfect actuator disk [15, Section 2.1]; momentum theory gives the relationship

$$\frac{C_P}{{C_T}^2} = \frac{1}{2\lambda} \,. \tag{5.1}$$

Real rotors can only approach the actuator disk limit, leading to the definition of an

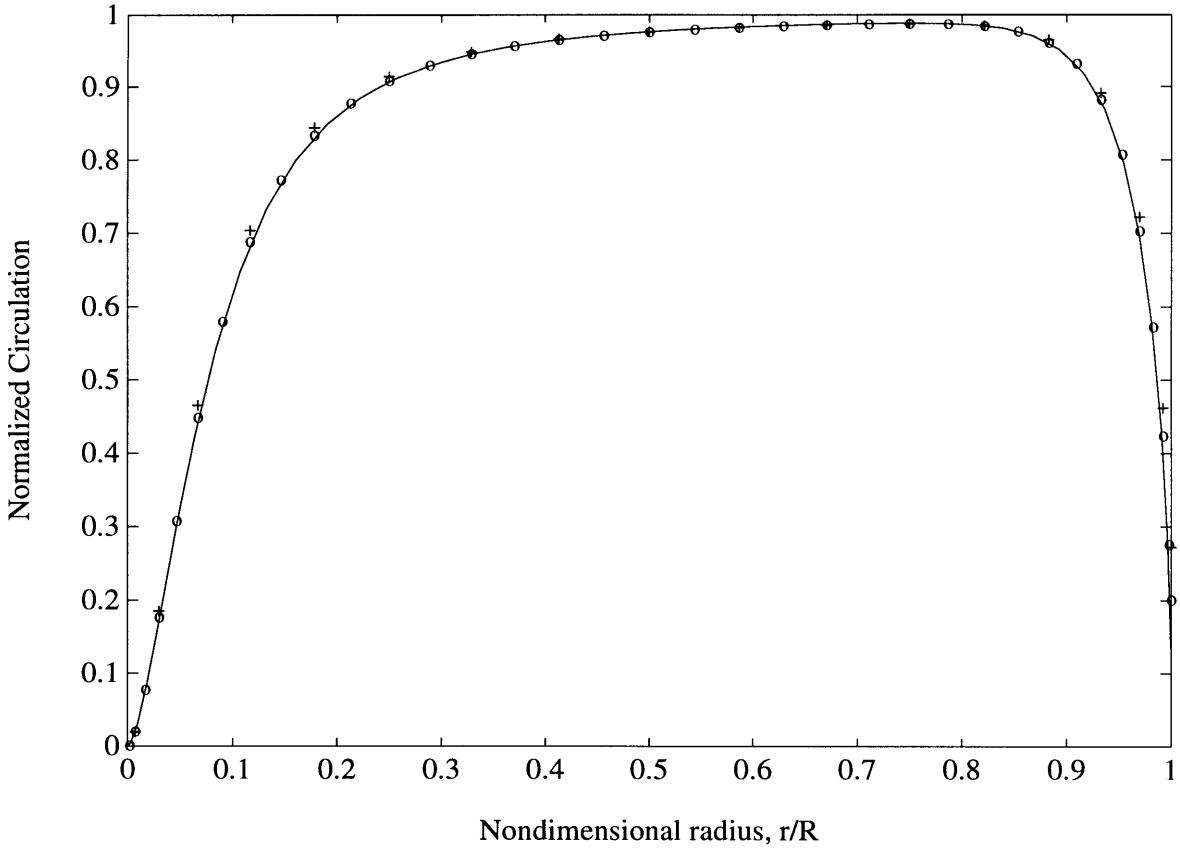

Figure 5-1: Axial Flight Circulation, $\Gamma B\Omega/(2\pi U\nu_T)$. — Goldstein solution; +, finite element solution using a $39 \times 31 \times 15$ computational mesh; o, finite element solution using a $77 \times 61 \times 29$ computational mesh.

induced loss factor, κ, which is greater than unity,

$$\frac{C_P}{{C_T}^2} = \kappa \frac{1}{2\lambda} \,. \tag{5.2}$$

The induced power at $C_T = 0.012$ for the finite element optimal rotor solutions is computed using two different methods. First a near wake calculation is performed using Equation (2.26). This requires the induced velocity at the disk, $w(r, \psi)$, which is calculated using a rigid wake vortex lattice code and the optimal rotor circulation distribution. Second, a far wake calculation is performed using Equation (4.44). These two calculations should yield the same result for a given circulation distribution.

Table 5.1: Finite Element Validation: Axial flight induced loss factors. $N = 4$, $\lambda = 0.2$.

	Loss factor, κ		
grid size	finite element	vortex lattice	Goldstein
$77 \times 61 \times 29$	1.086	1.067	1.067
$39 \times 31 \times 15$	1.077	1.067	1.067

The induced power for the exact Goldstein solution was also found using the vortex lattice program and near wake methods. The vortex lattice code could, by itself, reproduce Goldstein's circulation distribution when the code's wash influence coefficients were used in an optimization procedure. Therefore, its induced velocity calculation was deemed adequate for this limited study. A more exact way to calculate the induced power would be to examine Goldstein's method and isolate factors such as the induced velocity, but this degree of accuracy was not considered necessary. The induced loss factors for the Goldstein case and the finite element solutions are listed in Table 5.1.

All of the results in the table agree to within about 2%. The higher loss factor calculation found from the far wake methods is attributable to the fact that the mesh is slightly stiffer than the exact solution, and, as expected, the far wake solutions bound the answer from above (see Section 4.3). These particular far wake calculations exhibit one unusual discrepancy. The finer mesh is inherently less stiff than the coarser mesh and should predict a lower energy. Unfortunately, this is not the case, and could be a result of a lack of convergence in the solver during these particular runs.

Despite these irregularities, the power calculations and the circulation distributions of the two meshes are very similar. This indicates that the standard size finite element mesh adequately solves the minimum induced loss propeller problem.

5.1.2 Test of the Constraint Update Procedure

After the finite element procedure was validated, the iterative constraint update procedure was checked. For satisfactory performance of the constraint procedure, the

power calculation should converge without too many iterations and the augmented Lagrangians should settle to a stable set of values. Performance of the augmented Lagrangians is dependent upon a proper choice for the penalty weight, g, defined in Section 4.2. Although it was not discussed in Chapter 4, if convergence is too slow, then the penalty weight may need to be updated in a procedure similar to that used for the augmented Lagrangians [27].

As part of the CORC procedure, two types of convergence criteria are checked after each iteration. Each point in the constraint set is measured with two criteria:

$$\Delta_{1_j} = \left(\Gamma_j - \Gamma_{\max_j}\right) \frac{1}{\Omega R^2} \tag{5.3}$$

and

$$\Delta_{2_j} = \left(\Gamma_j - \Gamma_{\max_j}\right) \frac{1}{\Gamma_{\max_j}}, \tag{5.4}$$

where the factor of $1/(\Omega R^2)$ is merely used to nondimensionalize the first measure. Equation (5.3) measures how close a point is to its constraint boundary on an absolute scale. In contrast, Equation (5.4) measures how close a point is to its constraint boundary relative to the boundary value. For a solution which precisely meets the $C_{l_{\max}}$ constraints, then both Δ_1 and Δ_2 are zero everywhere on the disk. However, the iterative method employed allows the solution to violate the constraints by an arbitrarily small error.

For a given forward flight test case (to be discussed in detail in the next section), the convergence criteria are given in Table 5.2. The second column shows the induced power, calculated using Equation (4.44). The power increased with each iteration; it was effectively settled by the third iteration. This monotonic increase was found to be a characteristic of all the optimization runs.

The following columns in the table contain measures of the constraint violations. The values are the maximum deviations from the constraint boundary found anywhere on the disk, at the end of each iteration. Thus, they do not chart the progress of any particular point. The 3rd column displays the maximum value of Δ_1. The corresponding value of Δ_2 for the same point is given in the 4th column. Thus, these

Table 5.2: Constraint Update validation: convergence criteria for a typical, constrained local lift case. Average circulation over the disk is $\Gamma/(\Omega R^2)$=2.09e-2.

		Violation of Maximum Allowable Circulation			
		$j = \arg\max_j \Delta_{1_j}$		$j = \arg\max_j \Delta_{2_j}$	
iteration	C_P	Δ_{1_j}	Δ_{2_j}	Δ_{1_j}	Δ_{2_j}
1	3.80e-3	4.22e-2	6.6e+0	3.78e-2	1.7e+1
2	4.22e-3	2.49e-3	5.2e-2	2.03e-4	1.0e-2
3	4.22e-3	1.57e-4	4.0e-3	1.17e-4	8.2e-2

are the largest *absolute* violations of the constraints. The 5th (last) column of the table displays the value of the maximum Δ_2 found on the disk. The corresponding value of Δ_1 for this point is listed in the preceding column. These last two columns, then, are the largest *relative* violations of the constraints.

Both the absolute and the relative convergence measures demonstrate that the solution comes closer to satisfying the constraints with each iteration. In this case, convergence of the induced power calculations was considered complete after the third iteration. Although there is a point that is still 8.2% away from its constraint boundary, this can be considered insignificant, since the absolute violation (1.17e-4) is much smaller than the mean level of circulation.

Convergence in three iterations was typical of every constrained optimal rotor case tested, so it was deemed unnecessary to employ penalty weight updating. Given that the induced power calculation settled quickly and that the error in the constraints was small, it seemed clear that the constraint update procedure works.

5.2 Typical Forward Flight Optimization

Before an assessment can be made about the quality of an optimal rotor lift distribution, a baseline performance level must be established. This is presented next. Following that, optimal lift distributions from the CORC routine are discussed and

numerical performance measures are given.

5.2.1 Reference Lift Distribution

Flight conditions for the optimization tests were chosen to match those presented by Johnson [15, Chapter 13] and are listed in Table 5.3. A comprehensive rotor simulation, developed by Scully [33], was used to analyze a typical, non-optimal rotor at these flight conditions. The computer program used a vortex lattice to calculate the downwash at the rotor disk. This information was coupled to a blade dynamic model which introduced the effects of flapping, etc. to the system. There was no modeling of the fuselage's influence on the flow. At a disk loading of $C_T/\sigma = 0.12$, the case does not classify as light loading. Nevertheless, it was used because a detailed lift distribution was given in the reference. This data was discretized and analyzed so it could provide a clear baseline with which to evaluate the *optimal* rotor solutions.

The baseline lift distribution is plotted in Figure 5-2. Although it may not be apparent from the contours, the blade is stalled over a small region on the retreating side. Also note that the lift does not roll off to zero at the root and hub. Lift on real rotors characteristically falls off with a square root distribution at the tips. The behavior of the reference case is due to the fact that the vortex lattice emits a finite strength vortex filament from the tip and root. For a given C_T, the unrealistically high tip loading unloads the inner portions of the blade. This results in an overoptimistic efficiency estimate. When analyzing the spanwise loading efficiency of this

Table 5.3: Flight parameters of the reference case

Thrust coefficient	C_T	0.012
Forward advance ratio	μ	0.25
Number of blades	B	3
Rotor solidity	σ	0.1
Root cutout	$\bar{r}_c$	0.15
Linear blade twist	θ_{tw}	-8.0 deg
Nondimensional helicopter drag	f/A	0.015
Lock number	γ	8
Blade section lift curve slope	a	5.7

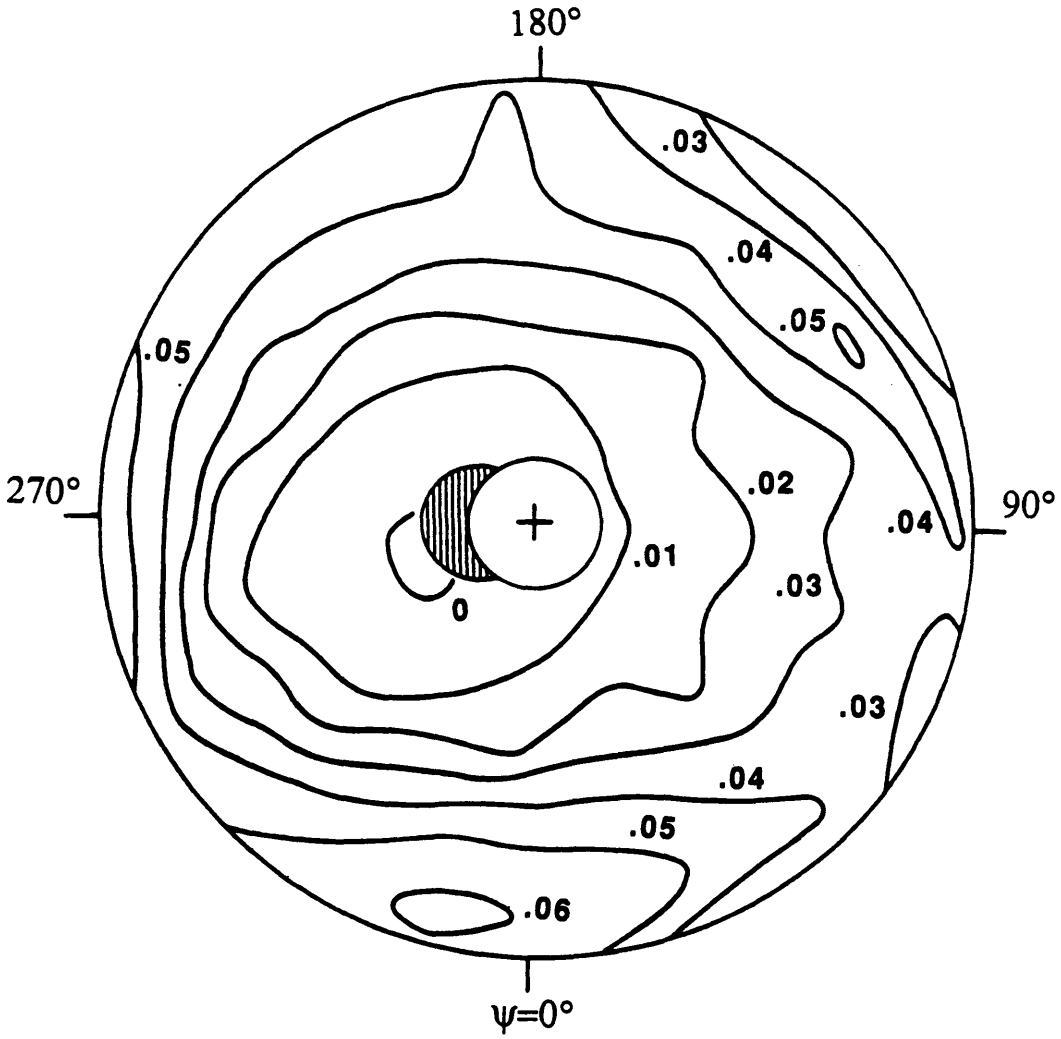

Figure 5-2: The reference lift distribution. $L/(\rho ac(\Omega R)^2)$. Flight parameters are listed in Table 5.3. Adapted from Figure 13-13 of Johnson [15] and used with permission.

distribution, as discussed in Section 2.3, this lack of tip rolloff may not necessarily be significant, because the analysis will smooth out such details in the flow. However, for induced power calculations, this could be significant. To calculate the power, the baseline lift distribution from approximately $0.2R < r < 0.95R$ was put into the CORC routine as a constraint. Using the standard sized mesh, the CORC routine outputted a distribution which matched the baseline between $0.2R$ and $0.95R$, but also rolled the lift off to zero at the tip and root. This modified reference distribution, rather than the original interpolated data, was used for induced power calculations.

5.2.2 Optimal Lift Distributions

Of the parameters listed in Table 5.3, the CORC routine utilizes only the first seven. The last two parameters specify blade structural properties and aerodynamic properties, which are not used. The fuselage drag coefficient gives the rotor tip path plane a slight angle, α_r, into the flow.

Although not discussed previously, *minimum* local lift coefficient constraints were put in place in exactly the same manner as the maximum local lift constraints, so that the rotor could not exert too great a downward force. Thus, in addition to the previously mentioned parameters, the CORC routine also requires specifications for the blade sectional lift coefficients, $C_{l_{\max}}$ and $C_{l_{\min}}$. Various levels of $C_{l_{\max}}$ were investigated, from $C_{l_{\max}} = 1.2$ to 1.5, which is the approximate maximum for a NACA 0012 symmetric, uncambered airfoil [1]. In all cases, $C_{l_{\min}}$ was set to the negative value of $C_{l_{\max}}$. Also, as an upper bound on the performance, the unconstrained solutions, in which $C_{l_{\max}}$ is effectively infinite, are also examined.

The maximum and minimum lift coefficients were taken to be constant along a blade, though they could have been made a function of position. Note that using constant sectional properties does not *a priori* specify the shape of the optimum rotor. The optimal lift distribution could imply that the blade should have varying radial properties, such as variable twist. This is certainly an available outcome in the solution space, as long as it does not violate the given local lift constraints.

The geometry of the far wake is specified by the vertical advance ratio, λ. Momentum theory [15, page 128] gives a relation between C_T and the net flux needed to achieve this loading,

$$\lambda = \frac{C_T}{2\sqrt{\mu^2 + (\mu \tan \alpha_r + \lambda)^2}} . \tag{5.5}$$

This formula can be solved iteratively, and in this case the solution converges to $\lambda = 0.024$. In addition to the inflow due to the momentum exchange, a geometric inflow of $\lambda = 0.01$ must be added in due to the tilt of the tip path plane (*i.e.*, the rotor disk) toward the flight path direction. Thus, the total inflow defining the wake's shape is $\lambda = 0.034$.

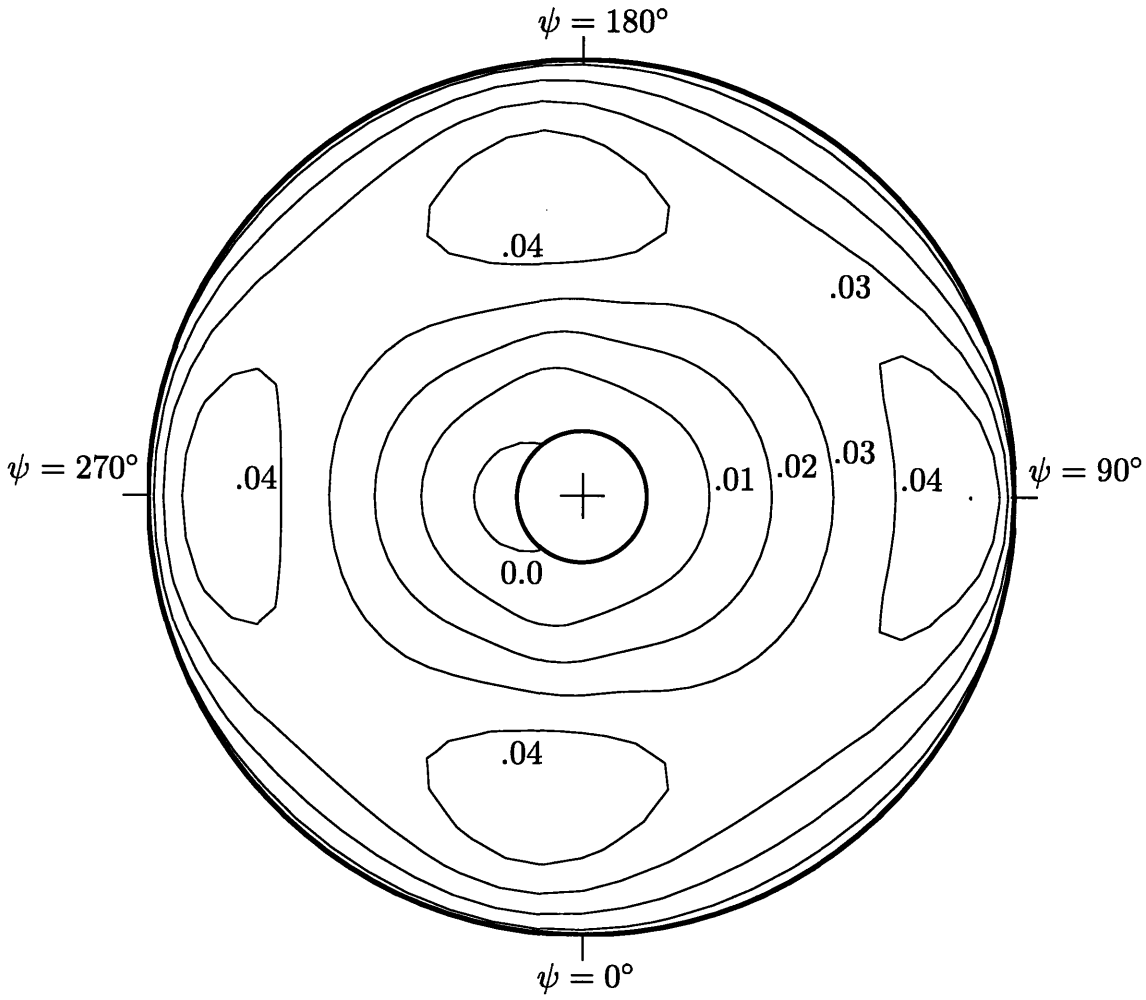

Figure 5-3: The optimal unconstrained lift distribution; $C_{l_{\max}} = \infty$. $L/(\rho ac(\Omega R)^2)$. Flight parameters are listed in Table 5.3.

Shown in Figure 5-3 is the unconstrained optimal lift distribution, i.e. $C_{l_{\max}} = \infty$. Several significant features of the distribution should be pointed out and compared with the reference distribution in Figure 5-2. First, the lift distribution rolls off with the expected square root behavior at the tip. This effect is commonly known as *tip losses.* Second, inboard of the tip, the optimal lift contours are smoother than those of the reference case. This indicates that much of the shed vorticity has been eliminated. As a result, the optimal lift distribution should exhibit less severe unsteady flow effects and should, therefore, be more efficient. Third, the optimal lift distribution is symmetric fore and aft. A symmetric lift (and, hence, a symmetric circulation) for forward flight is not an obvious solution. The explanation for this

phenomenon comes from looking at the far wake. At a position in the far wake, the wake extends downwards effectively for an infinite distance and upwards towards the helicopter for an effectively infinite distance. Thus, the wake is symmetric with respect to a 180° rotation about the y axis. The symmetry means that the circulation any point in the wake has a reciprocal influence on the induced velocity at any other point in the far wake.

This symmetry should not be interpreted to extend entirely to the induced wash. While the induced wash in the far wake is fore-aft symmetric, it is not symmetric in the near wake, *i.e.*, at the rotor disk. This is because at the rotor disk there is no wake extending above to allow for the reciprocal velocity induction. Therefore, the optimal solution dictates that the rotor must produce a symmetric lift distribution while flying through a non-symmetric induced velocity field.

Next, in Figure 5-4, the constrained optimal lift distribution is shown for a maximum and minimum lift coefficient of 1.2. Following that, the distribution for $C_{l_{\max}} = 1.5$ is plotted in Figure 5-5. Like the unconstrained case, both of these distributions roll off at the tips and are symmetric fore and aft.

On the whole, the two constrained optimal lift distributions look similar. However, the case with a lower $C_{l_{\max}}$ carries more lift toward the rotor tips and achieves higher peak lift values. Further tests have shown that all constrained optimal lift distributions resemble these two, with the lift contours shifting radially inwards or outwards depending on the level of the maximum allowable lift.

Furthermore, both constrained optimal lift distributions display a region on the retreating side where the contour lines form sectors of concentric circles. This is the region where the maximum lift coefficient constraints must be enforced. The constrained nodes are pinpointed exactly for the $C_{l_{\max}} = 1.5$ case in Figure 5-6. Lift in the marked region is at a maximum.

By closely examining the constrained region of Figure 5-4, it can be seen that the reference case has contours that are radially more inboard at each contour level. This means that the effective lift coefficient of the reference case is higher than 1.2. Further inspection reveals that the reference case has a lift coefficient closer to the

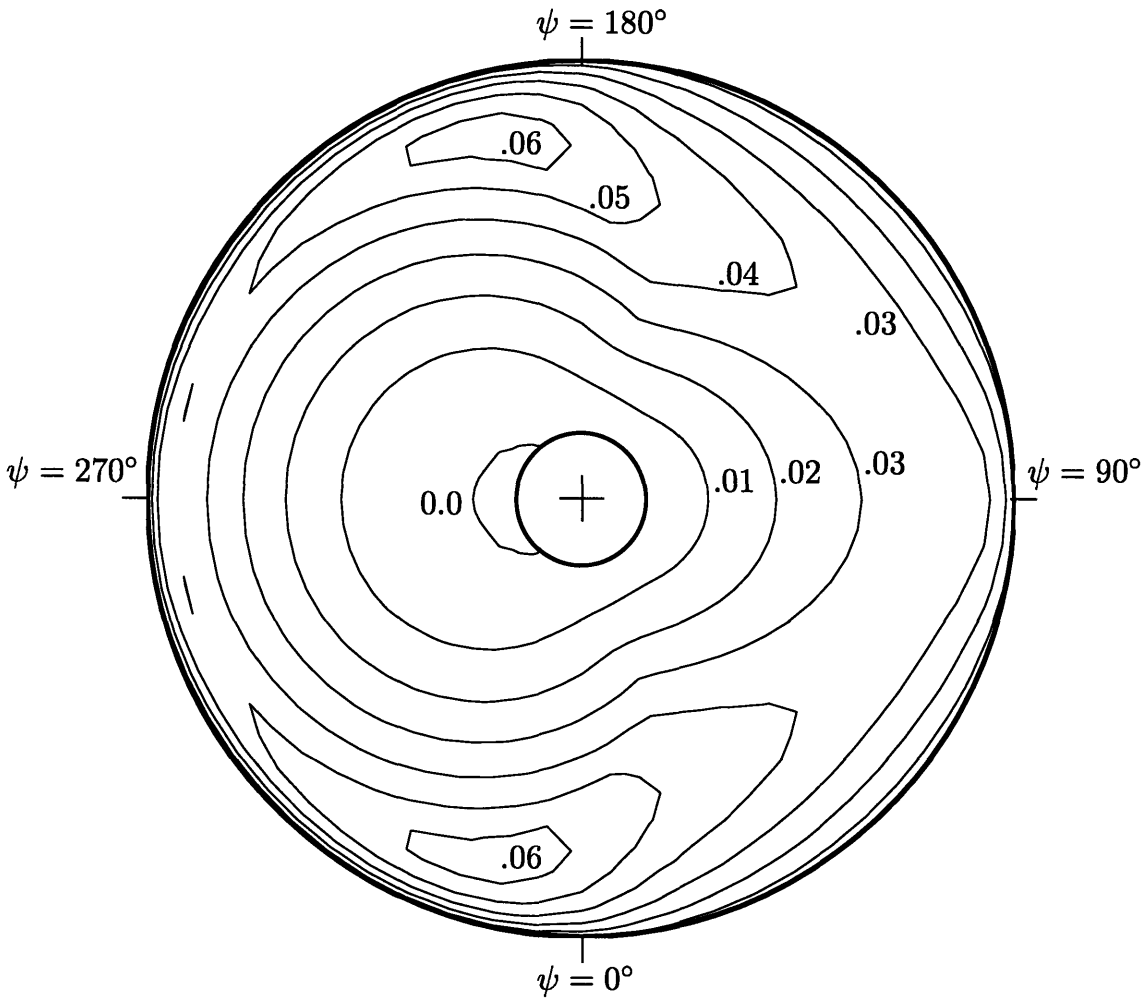

Figure 5-4: The optimal lift distribution with $C_{l_{\max}} = 1.2$. $L/(\rho ac(\Omega R)^2)$. Flight parameters are listed in Table 5.3.

optimal case with $C_{l_{\max}} = 1.5$.

Because the rotor must maintain a certain thrust, limiting the lift in the constrained region pushes that lift into the fore and aft regions. Specifically, the peaks in the lift distribution occur near $\psi = 200°$ and $\psi = 340°$. This is consistent with most findings concerning 2/rev control. Past research [3], [38] has predicted that 2/rev control could best improve performance by concentrating lift towards the fore and aft. In particular, a recent study by Nguyen and Chopra [25] predicted that the best 2/rev performance would be achieved by effecting pitch up in the first and third quadrants of the disk. Though the peak in the third quadrant seems to match the peak near $\psi = 340°$ in the optimal distribution, the 2/rev controller is forced to peak

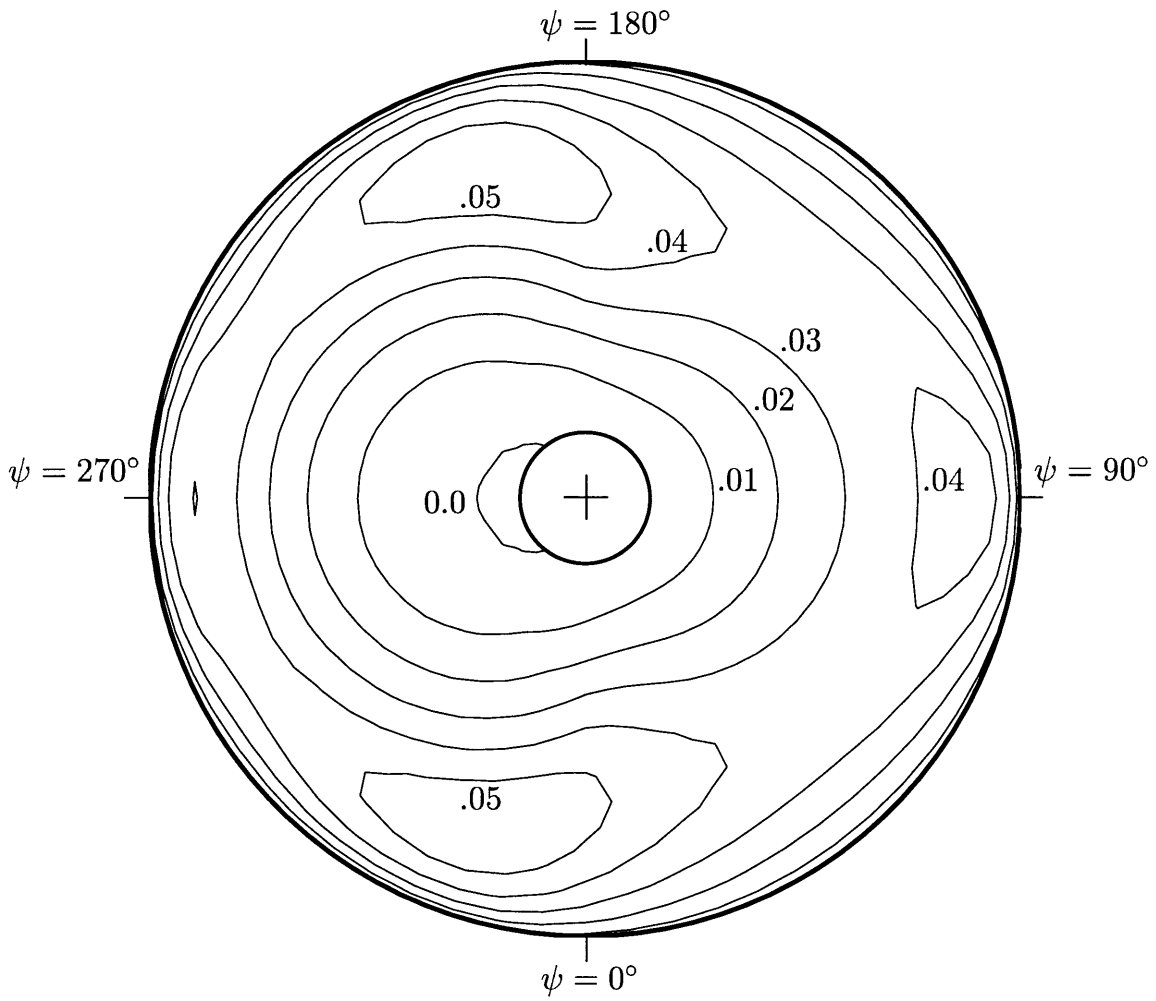

Figure 5-5: The optimal lift distribution with $C_{l_{\max}} = 1.5$. $L/(\rho ac(\Omega R)^2)$. Flight parameters are listed in Table 5.3.

in the first quadrant, which is after the peak predicted by the optimal. However, actuating the controller to achieve this second peak predicted by the optimal is not critical to performance, because, as the baseline distribution shows, typical helicopter lift distributions may already be near optimal in this region.

Further discussions of how a rotor could physically attain the optimal solution will be put off until Chapter 6. It should be realized that arbitrarily trying to match a particular lift contour will not necessarily provide performance enhancement. This is because the lift distributions do not explicitly contain the information about which regions of the disk are the most sensitive to power production. That information is contained in the far wake wash distribution.

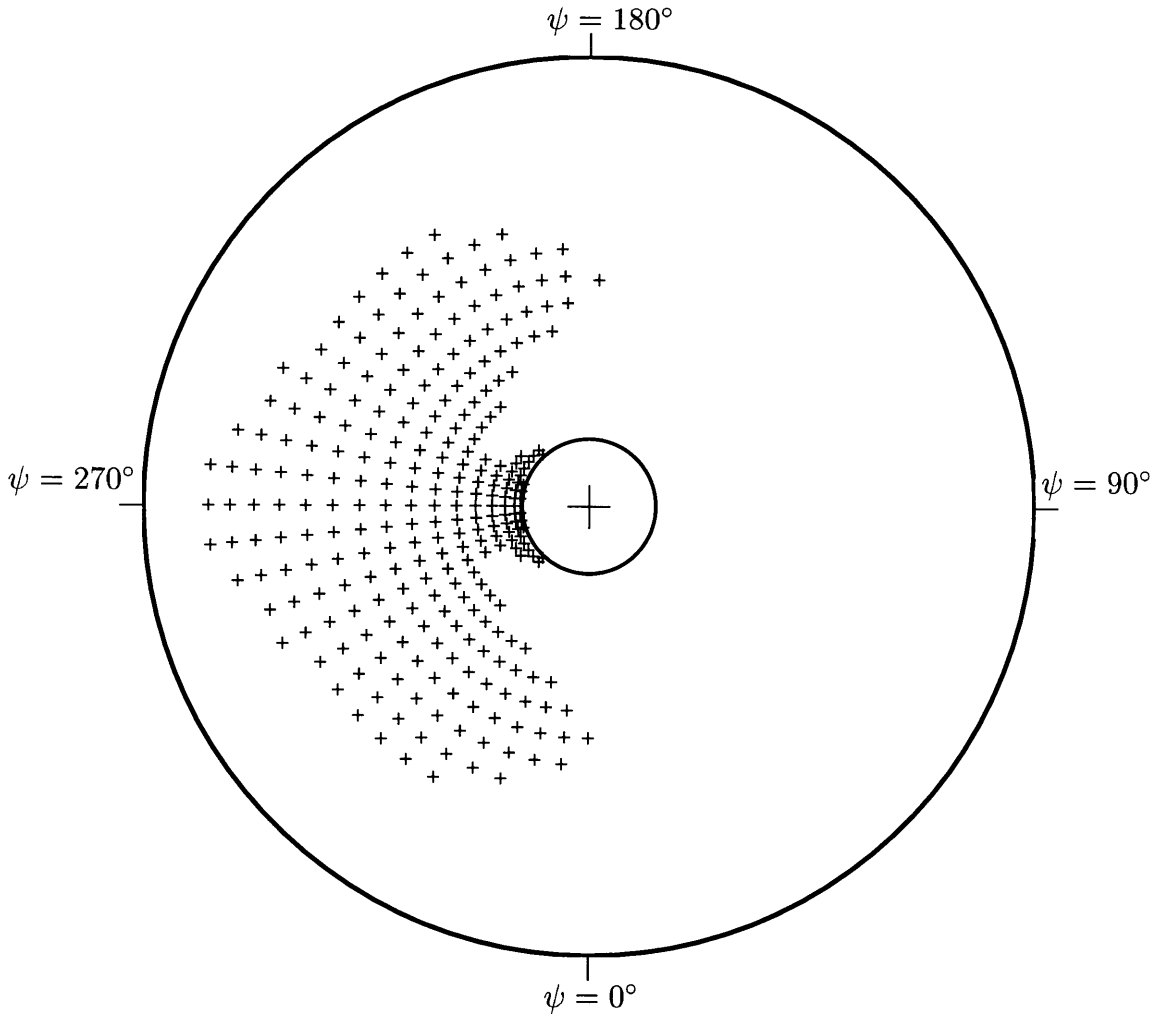

Figure 5-6: The constraint set for the lift distribution of Figure 5-5. A "+" means that the node is in set C_a or C_b. If no symbol appears, then the point is not in the constraint set.

5.2.3 Measures of Efficiency

In order to get a quantitative understanding of the advantages to using an optimal distribution, an efficiency can be calculated. Two different measures will now be checked. The first is the spanwise loading efficiency, and the second is the induced power.

Spanwise Loading

This analysis follows the procedures outlined in Section 2.3. As mentioned earlier, there is some question as to how the data for the reference case should be represented.

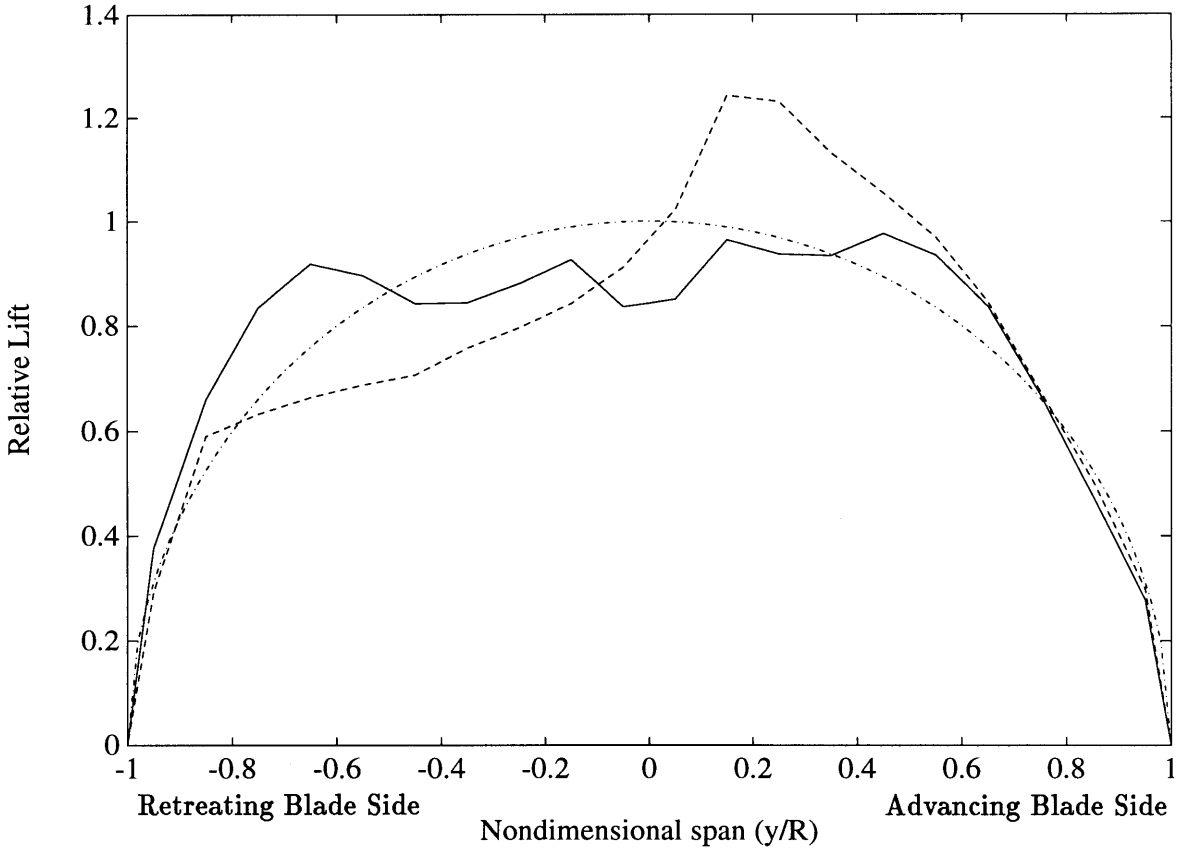

Figure 5-7: Spanwise loading for the reference case. —, reference case without tip losses as interpolated directly from Figure 5-2; – – –, reference case with tip losses as outputted by the CORC program; — · —, elliptical lift distribution.

The reference case can be modified to include tip rolloff, using the CORC routine, or it can be analyzed in its original interpolated form. Figure 5-7 shows the spanwise loading for both representations. The raw data is considerably noisier, but flatter, since it carries lift out to the tips. Also shown is the optimal fixed wing loading which is, of course, elliptical.

Next, in Figure 5-8, the spanwise loading distributions are shown for the optimal rotor with no constraints on the lift coefficients and the optimal rotor with the local lift coefficient constrained not to exceed 1.5. Both optimal spanwise loadings are noticeably closer to the elliptical distribution than the reference loadings, because lift is raised toward the center and decreased toward the tips. This spanwise view is

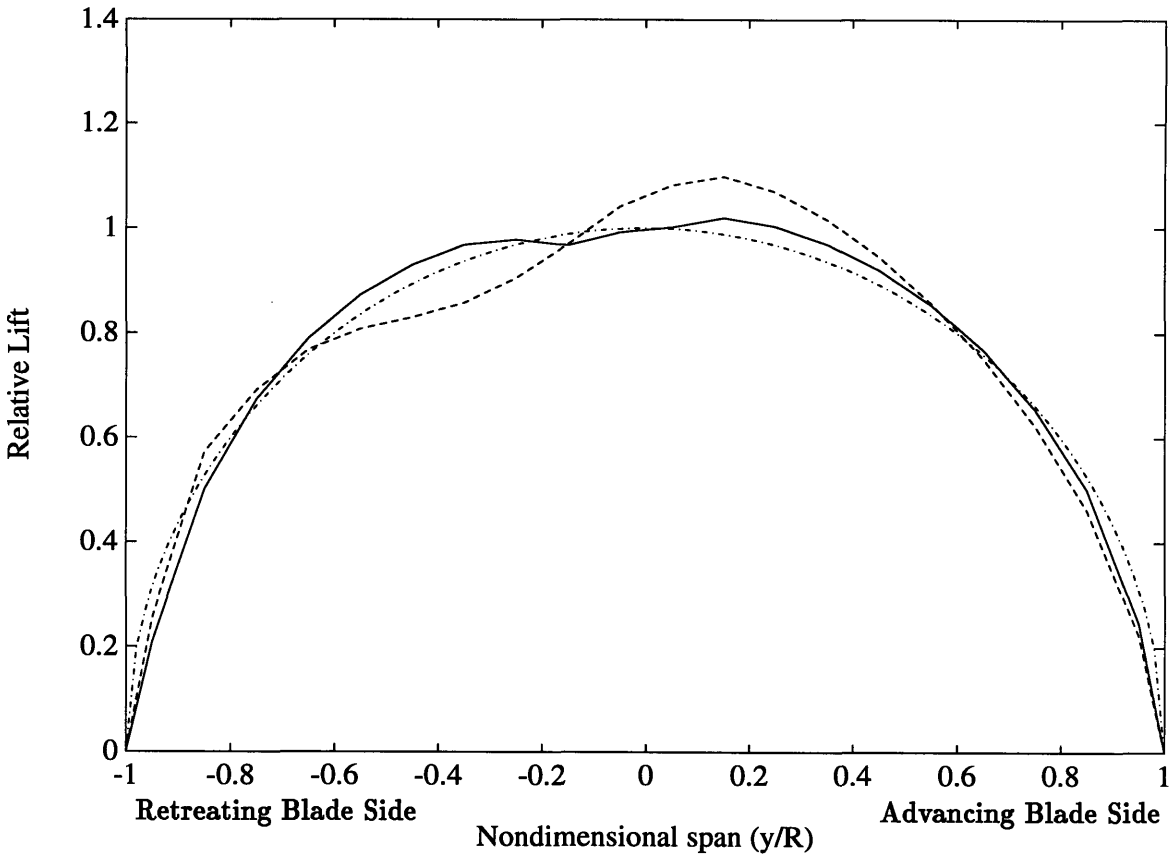

Figure 5-8: Spanwise loading for the optimal cases. —, optimal case with $C_{l_{\max}} = \infty$; – – –, optimal case with $C_{l_{\max}} = 1.5$; — · —, elliptical lift distribution.

consistent with the observation that the optimal loading distributions tend to shift the lift toward the fore and aft regions of the rotor disk.

Using Equation (2.12), span loading inefficiencies are calculated for each case and displayed in Table 5.4. The numerical results confirm the visual assessments made earlier. The reference case has a loss factor which is between 8% and 12% greater than unity, depending on whether or not tip losses are included. In contrast, the unconstrained optimal distribution is only 2% out of elliptical. As the maximum possible local lift is reduced, efficiency decreases, till at a maximum lift coefficient of 1.2, the optimal rotor is of comparable efficiency to the reference case.

Spanwise loading provides a straightforward visual means of comparing lift distributions, but its numerical analysis does not account for swirl losses nor for shed

Table 5.4: Loss factors computed from spanwise loading analysis.

	grid size	$C_{l_{\max}}$	Loss factor, κ
Baseline with tip losses	—	—	1.12
Baseline without tip losses	—	—	1.08
Optimal	$77 \times 61 \times 29$	1.2	1.11
Optimal	$77 \times 61 \times 29$	1.5	1.04
Optimal	$77 \times 61 \times 29$	∞	1.02

vorticity. A more selective, but complementary, comparison can be made by computing the induced power.

Induced Power

Induced power is the most valid and critical means of judging the merit of any rotor lift distribution. Because its calculation uses incremental information at every point on the rotor disk, it fully accounts for all of the effects of nonuniform inflow, swirl, tip losses, and shed vorticity. It was this quantity that was specifically minimized to produce the optimal distributions and, as such, is the major focus of this study.

The induced power can be computed using two methods, as was done for the finite element validation tests. First, is the the near wake analysis, using Equations (2.26) and (2.28) with a rigid wake vortex lattice code. The second method, Equation (4.44), uses the information from the finite element code alone. While the finite element power calculation is guaranteed to overbound the exact solution, no such fundamental relation governs the behavior of the vortex lattice power calculation.

For each rotor lift distribution, an induced loss factor κ was computed using Equation (2.7) and the results are compiled in Table 5.5. The finite element and vortex lattice induced power calculations agree well, to within 2–3%. The unconstrained optimal lift distribution is 21% to 25% more efficient than the reference case. As the maximum level of allowable local lift is lowered, lift is pushed from the retreating blade side into the fore and aft regions of the disk. Accordingly, the induced power increases with lower $C_{l_{\max}}$ settings. At a maximum lift coefficient of 1.5, which approximately matches the maximum lift coefficient of the reference case, the optimal is between

Table 5.5: Loss factors based on induced power

	grid size	$C_{l_{max}}$	Loss factor, κ	
			finite element	vortex lattice
Baseline	—	—	1.75[a]	1.70[a]
Optimal	$77 \times 61 \times 29$	1.2	1.68	1.72
Optimal	$77 \times 61 \times 29$	1.5	1.47	1.51
Optimal	$77 \times 61 \times 29$	∞	1.32	1.33

[a]Original baseline lift distribution was optimized inside of 20% span and from 95% span outwards to introduce tip losses.

11% and 16% more efficient.

It is possible that the CORC routine's standard finite element mesh could still be overly stiff (see Section 4.4), in which case the induced power readings would be too high. This does not seem to be the case for the results presented in Table 5.5, since the finite element and vortex lattice calculations match closely. However, even if the calculations for the induced power require adjustment, it will be a collective change. Thus, a relative ranking in efficiency would be the same. The percentage difference in loss factors clearly demonstrates the superiority of an optimal rotor distribution over the reference case.

5.3 Effects of the Number of Blades

When Betz [6] derived his original theory for the minimum induced loss propeller, he assumed that the propeller had an infinite number of blades. Prandtl recognized that this resulted in an overprediction of efficiency and introduced an approximate correction factor to account for any given number of blades. Efficiency decreased as the number of blades decreased because larger inter wake sheet spacings allowed more flow to interact with air outside the wake tube. These end effects caused tip losses. The brief numerical study described in this section examined the effects of the number of blades on the optimal rotor in forward flight.

Flight conditions for this study are the same as those shown in Table 5.3, except

that the number of blades is set to *four* instead of three. The solidity, σ, was held at its original value. It is important to note that solidity is a characterization of blade geometry, so it has no inherent effects in far wake theory. However, it does affect the constraints on the maximum allowable local lift coefficients, because the blade chord is defined as

$$c = \frac{\pi R^2}{BR}\sigma = \frac{\pi R}{B}\sigma \,. \tag{5.6}$$

Recall Equation (3.36), which sets the maximum allowable circulation levels. This means that, for a fixed radius, an increase from $B = 3$ to $B = 4$ results in a 25% decrease in $\Gamma_{\max}(r, \psi)$ everywhere on the disk. Thus, the lift constraints are *tighter* for a given level of $C_{l_{\max}}$. Of course, these changes to $\Gamma_{\max}$ are irrelevant to the unconstrained problem.

More fundamentally, the increase in the number of blades affects the geometry of the far wake. The control volume, $\mathcal{V}$, is thinner, *i.e.*, there is less space between adjoining wake sheets. Renewing the split washer analogy, stacking four of the new control volumes or three of the original control volumes would yield an ungapped, skewed cylinder with exactly the same dimensions.

Test runs were made using the standard $77 \times 61 \times 29$ mesh used earlier. The lift distributions for two levels of $C_{l_{\max}}$, are shown in Figures 5-9 and 5-10. The general character of any four bladed optimal distribution is similar to that with $B = 3$.

The maximum lift for the four bladed unconstrained case has dropped to 75% of its value for the three bladed case. Each blade is effectively unloaded by 25%, since four blades now do the work of three. However, the *plots* of the three and four bladed distributions do not appear significantly different because the lift has been normalized by the blade chord. For the cases with constraints on the maximum local lift, the blades are similarly unloaded, but the lift constraints have simultaneously been tightened. The net result is that the new distributions are constrained in approximately the same regions as the cases with three blades.

For a baseline efficiency measure, the reference distribution was again inputted to the CORC routine as a constraint, but four blades were used instead of three.

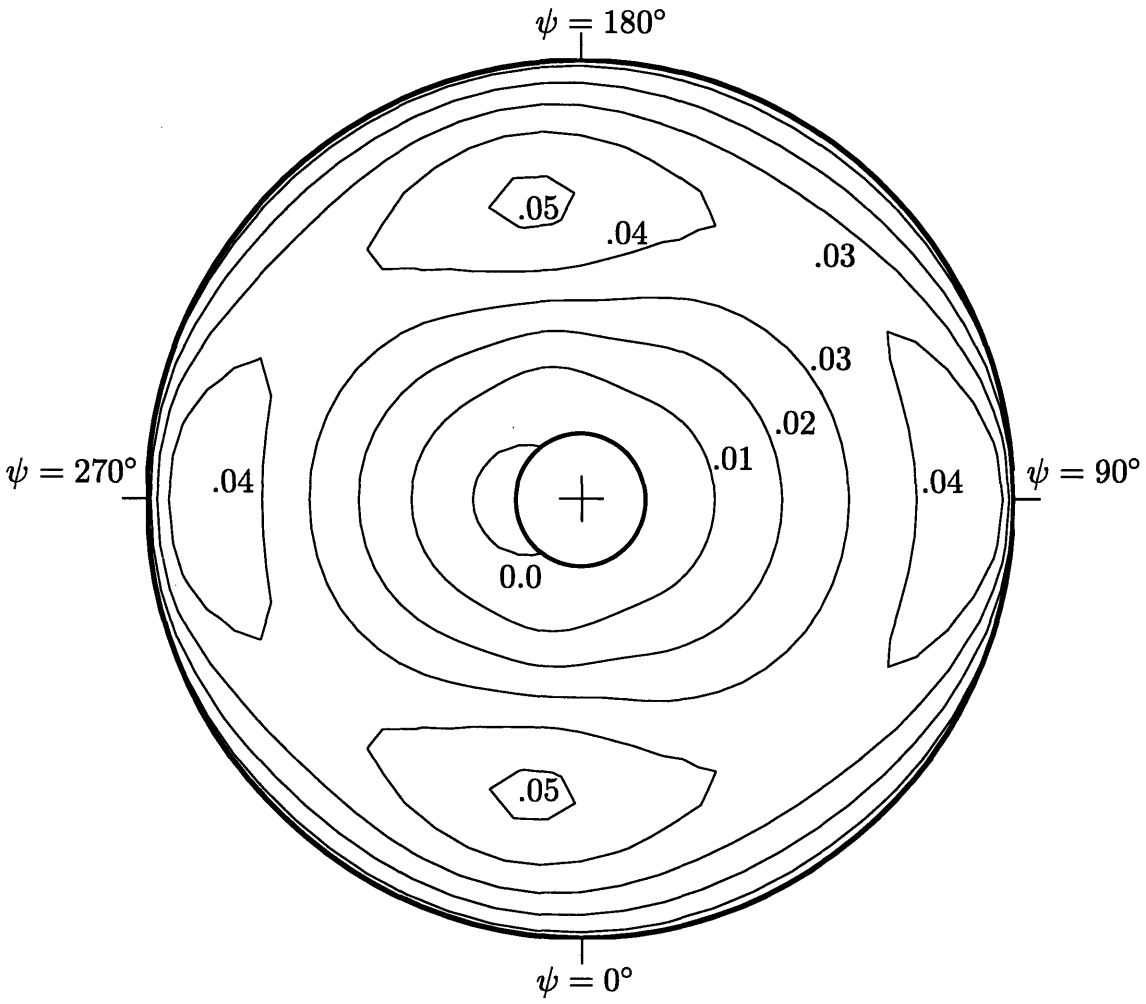

Figure 5-9: The four bladed optimal lift distribution with $C_{l_{\max}} = \infty$. $L/(\rho ac(\Omega R)^2)$. Flight parameters except for the number of blades are listed in Table 5.3.

Induced power loss factors and and spanwise loading loss factors were calculated for all of the cases and are displayed in Table 5.6. Some cases were run with a slightly different root cutout, but this was shown to have a negligible effect on the induced power.

Comparing the data for the four bladed cases to their three bladed counterparts in Table 5.5, it is evident that efficiency increases with the number of blades. The exact amount of change is difficult to specify because the spanwise loading analysis shows almost no change in efficiency, while the power analysis shows improvements ranging from 10% to 20% depending on the flight condition.

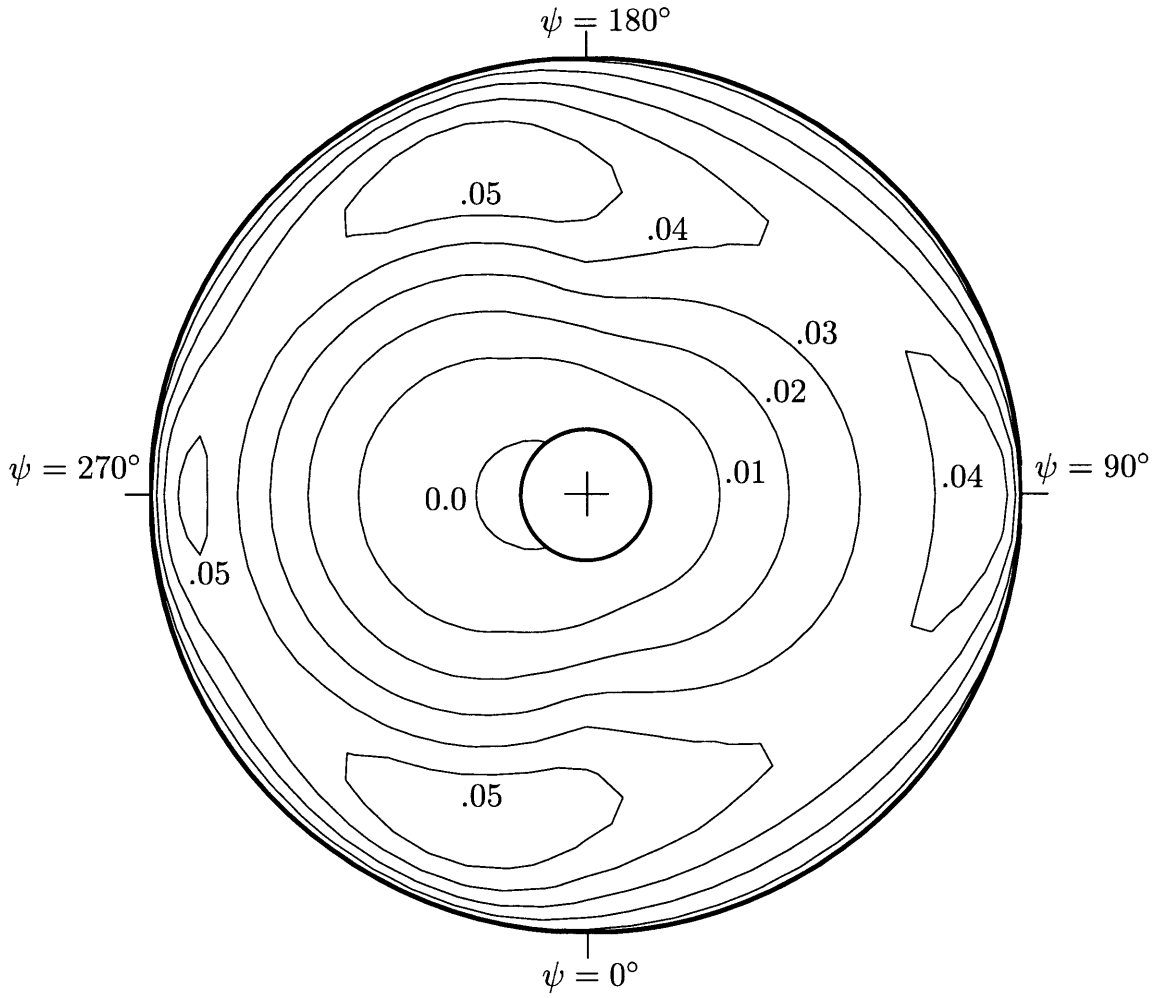

Figure 5-10: The four bladed optimal lift distribution with $C_{l_{\max}} = 1.5$. $L/(\rho ac(\Omega R)^2)$. Flight parameters except for the number of blades are listed in Table 5.3.

Table 5.6: Induced loss factors for the four bladed rotors

	grid size	$C_{L\max}$	Loss factor, κ		
			finite element	vortex lattice	spanwise loading
Baseline	—	—	1.50[a]	1.37[a]	1.08[b]
Optimal	$77 \times 61 \times 29$	1.2	1.49[c]	1.39[c]	1.08[c]
Optimal	$77 \times 61 \times 29$	1.5	1.30	1.24	1.03
Optimal	$77 \times 61 \times 29$	∞	1.23[c]	1.19	1.02

[a] Original baseline lift distribution was optimized inside of 20% span and from 95% span outwards to introduce tip losses.
[b] Original baseline lift unmodified.
[c] $\bar{r}_c = 0.20$

The four bladed cases show much wider discrepancies between the power calculated from the finite element method and from the vortex lattice method. This is probably due to a worsening stiffness problem in the finite element mesh. The change from three to four blades actually accentuates the skew in some elements of the retreating side, especially in the reverse flow region and near the boundaries of the constrained region. Although these areas should contain relatively low levels of energy, excessively stiff elements could still present problems. Thus, the vortex lattice power calculation is considered more reliable for the four bladed runs.

Chapter 6

Smart Rotor Performance

The results presented in the previous chapter clearly demonstrate that a typical helicopter achieves less than optimal efficiency. The lift distributions in Figures 5-3 and 5-5 provide a clear aerodynamic goal which must be attained to achieve the minimum induced power loss. However, so far, the aerodynamic optimization has provided no information on what would be the best choice of rotor technology to achieve these conditions. This chapter contains a brief investigation of the matter.

As discussed in the first chapter, higher harmonic swashplate control has been demonstrated to offer performance improvements over conventional rotors [36]. Of particular importance is 2/rev swashplate control, since this can raise the lift toward the fore and aft regions of the rotor disk and delay blade stall.

However, an examination of the lift contours in Chapter 5 reveals that considerable radial variations in the lift may be necessary for power reduction. One way to achieve this is with a *smart rotor*, in which independently actuated servoflaps are distributed over the radius of a blade. Flap deflection causes a change in the local lift at the flap, but also twists the blade by a significant amount, since the blades operate at speeds well past the aileron reversal speed [8]. This means that the servoflap can be thought of both as a *local* lift augmentation device and as a blade twist mechanism. A flap schedule which reduces the induced power must balance the effects of each of these philosophies.

In the next section, a rotor model for higher harmonic control (HHC) will be

selected. That model is developed in the Section 6.2. Then, a procedure is developed to obtain swashplate and servoflap deflection schedules to meet the optimal lift conditions. These results are discussed in the last section of this chapter.

6.1 HHC Model Selection

Modeling any lift control device is inherently more complicated than modeling the far wake, because of the complicated flow patterns in the near field of the rotor. This is due to several effects. First are the aerodynamic lags associated with Theodorsen's work [15, Section 10.2]. Changes in pitch or camber cause the blade to shed a vortex parallel to the blade. The wash caused by this vortex effectively reduces the effect of the camber change. Second are the blade flapping and pitching dynamics. Both of these motions change the velocity field encountered by the blades.

It was decided to investigate the effects of trailing-edge servoflaps by using the most sophisticated near wake analysis tools available to the author. Comprehensive rotor analysis codes have been written which include multiple degrees of freedom for each blade, and model the aerodynamics using a vortex lattice, Theodorsen-type lags, and dynamic stall effects. One such analysis program is the Boeing Helicopter Company's proprietary code, named C-60 [39]. This code was tested using a four-bladed H-34 rotor. Each blade was augmented with a single 20% chord, trailing-edge servoflap placed between $0.625R$ and $0.8625R$. The flaps could be given a harmonic input. This case is identical to a system investigated on C-60 by Fox [8].

The lift distributions of the four-bladed H-34 rotor were examined in a test without flap actuation and then in a test with 5 degrees of 4/rev flap actuation. In both cases, a conventional swashplate provided pitch inputs to maintain trim. At an advance ratio of $\mu = 0.39$ and a blade loading of $C_T/\sigma = 0.06$, it was found that the blades' torsional response looked very similar to a static aeroelastic response. As the flap pitched down, it increased the local lift near the flap location. However, the flap actuation also caused a nose down pitching moment, which was manifested as lower lift along the rest of the blade span. This effect, known as aileron reversal, is common

for rotors with trailing edge flaps. Most significantly, the blades' pitching motions were very close to being 180° out of phase with the prescribed 4/rev flap deflections. The blade pitching and blade flapping dynamics apparently had little effect on the thrust. Thus, the predominant effects of the flap could have been obtained using a static aeroelastic analysis.

The fact that the blades' response was not dominated by dynamic effects can be explained by recalling the frequency response of a single degree of freedom, second order, harmonic oscillator. Frequency response charts, based on analytical formulae, exist for these systems and give the amplitude ratio between output magnitude and input magnitude. To apply these charts to this system, it was calculated that the H-34 rotor had a natural frequency in torsion of about 7.6Ω. Also, the system was forced at a frequency of 4Ω, via the servoflap. The charts predict that dynamic effects would cause the input magnitude to be magnified by less than 40% over the static response. For a 3/rev input, this magnification drops to less than 19%, and for a 2/rev input it drops to less than 8%. Thus, a static aeroelastic analysis should give a response that is reasonably close to the dynamic response, for input frequencies below 4Ω.

Further studies of servoflap effectiveness could have been conducted using the C-60 program. However, analyzing the output from the program required several hours per test case. This expenditure of time was deemed unnecessary, since it would produce only a moderate increase in accuracy over a static analysis. Therefore a static aeroelastic model was developed for the rotor.

6.2 Static Aeroelastic Model

The key assumption in the development of the static model is that the velocity field can be determined from geometry. Blade flapping dynamics are not included, so the velocity at a blade is $\boldsymbol{U}$, which was defined in Section 2.4. Also, both the structural and aerodynamic theory employed is linear, so the effects of the flap and the swashplate can be superposed to the original system to calculate a net effect.

In linear aerodynamics, actuation of the flap downwards causes a nose down moment which is proportional to the flap deflection,

$$dM_\eta = \frac{1}{2}\rho \left|\boldsymbol{U}\right|^2 c^2 C_{M_\eta} \eta \,, \tag{6.1}$$

where η is the flap deflection in radians, dM_η is the moment per unit span and C_{M_η} is the flap's coefficient of moment. Integrating this quantity over the width of the flap yields the moment on the blade, inboard of the flap location. Beyond the flap location, the flap produces no moment. Of course, this moment produces a twist in the blade, which causes an additional angle of attack

$$\alpha(\tilde{r}) = -\int_0^{\tilde{r}} \frac{M_\eta}{GJ}\, dr \,, \tag{6.2}$$

where $\tilde{r}$ is any radial position inside the flap location, and GJ is the torsional rigidity, which can vary with r. For piecewise constant structural properties, the blade twist will be piecewise linear.

The effect of the flap on the lift is more subtle. The nominal lift on a blade section away from the flap is

$$l(r) = \frac{1}{2}\rho \left|\boldsymbol{U}\right|^2 ca\alpha \,, \tag{6.3}$$

and the nominal lift at a section of the flap is

$$l(r) = \frac{1}{2}\rho \left|\boldsymbol{U}\right|^2 c \left(a\alpha + C_{l_\eta}\eta\right) \,, \tag{6.4}$$

where C_{l_η} is the flap lift curve slope. However, use of the nominal values would lead to a discontinuous lift at the boundaries of the flap, which is unrealistic. In reality, the lift should undergo a continuous transition at the flap boundaries, and the lift over the flap will be less effective than predicted by Equation (6.4).

To approximate the continuous lift function due to a flap, a test was conducted with a fixed-wing, lifting line model. Using the spanwise Fourier analysis discussed in Section 2.3 (also see [18, Chapter 6]), the circulation distribution for a wing with a step function in its geometric angle of attack was calculated. It was found that the lift

made a smooth transition, taking approximately two chord lengths on either side of the jump in the blade angle to attain its final, nominal value. At approximately one chord length past the blade discontinuity, the lift was seen to reach only 88% of its nominal value. This lift transition effect was fitted with an arctangent function, which was then used to modify the nominal lift values given by Equations (6.3) and (6.4). It should be noted that the size of the transition region is logically defined in terms of the wing's chord and not the span, since even an infinite span wing would show the same transition effect.

A final modification was made to the nominal lift functions in Equations (6.3) and (6.4). Prandtl's tip loss function [29] was used to ensure that the lift fell smoothly to zero at the blade tips. This approximation was strictly meant only for propellers but it does ensure that the lift falls in the proper square root fashion.

Development of the model for swashplate actuation followed the previous discussion. However, the blade did not elastically twist due to a root input. Therefore, Equation (6.3) could be used to calculate the lift across the entire blade.

The basic structural properties used for the model came from the H-34 rotor. The rotor was modified to have only three blades; also the root cutout and chord were modified to more closely match the parameters of the reference rotor in Chapter 5 (see Table 5.3). The final blade characteristics for the aeroelastic model are listed in Tables 6.1 and 6.2. Note that the blade's natural frequency in torsion was kept at 7.6Ω.

The flap used in the model was sized to be 15% of the blade's chord. This was smaller than the 20% chord flap which was found effective for vibration control by Fox [8]. The flap had a nominal section lift curve slope of 3.3059 rad^{-1}, and a section pitching moment curve slope of 0.6417 rad^{-1}. The flaps could be located in any of thirteen bays, with the following radial boundaries (r/R) demarcating each available bay: 0.2800, 0.3450, 0.4100, 0.5250, 0.5750, 0.6250, 0.6800, 0.7300, 0.7700, 0.8050, 0.8375, 0.8625, 0.8875, 0.9125. These spacing locations were chosen because they matched the borders of the piecewise constant data available for the H-34's structural properties.

Table 6.1: Selected properties of the modified H-34 blade and flight conditions in the static aeroelastic model

Property	Value
Forward speed, V_x	163 ft/s
Rotational speed, Ω	222 RPM
Number of blades, B	3
Blade radius, R	28 ft
Blade chord, c	1.37 ft
Root cutout, $\bar{r}_c$	0.15
Section lift curve slope, a	5.73 rad^{-1}
Torsional natural frequency	7.6 Ω

Table 6.2: Torsional Rigidity of the H-34 Blade

location, r/R	GJ (lb in^2)
0.0357–0.0900	1.9000×10^8
0.0900–0.1300	5.8712×10^7
0.1300–0.1400	2.4890×10^7
0.1400–0.1500	2.0566×10^7
0.1500–0.2150	1.8960×10^7
0.2150–1.0000	1.8000×10^7

6.3 Flap Schedule Optimization

The original optimization of the induced power cost functional, with respect to variations in the velocity potential, the circulation, and trim Lagrange multipliers, was done in the far wake. It was shown, in Equation (3.27), that the sensitivity of the induced power to changes in the circulation is proportional to the far wake induced wash. It would be useful to incorporate this sensitivity information explicitly into the optimization of the control schedules. Unfortunately, this cannot be done because of practical limitations. In the finite element model, the far wake induced wash has one order lower continuity than the potential or circulation information. When calculating the power internally to the finite element code, the wash is never explicitly calculated. Instead, flux is calculated for element surfaces. However, if the induced velocity is desired as an output of the code, then the velocity at any point must be

calculated by averaging the flux of surrounding elements. This produces a wash distribution which is generally smooth, but has noticeable noise. Thus, the sensitivity of individual points on the lift distribution is subject to error and is not reliable for an optimization. With this in mind, the flap schedule optimization will be performed entirely in the near wake.

As mentioned previously, the aerodynamic and structural operators used in the aeroelastic model are linear. Therefore, the results of a flap input can be superposed to a baseline lift distribution, such as the reference case considered in Chapter 5.

Recalling Equation (3.35), the flap or swashplate input can also be related to the bound circulation on the blade. The induced power can then be calculated using near wake methods, Equation (2.26). This demonstrates that the power can be expressed as a quadratic function of the flap and swashplate inputs,

$$P_{\mathrm{i}} = \frac{B}{2\pi} \int_0^{2\pi} \int_0^R \rho \left(L_{\mathrm{ref}} + \boldsymbol{D}\,\boldsymbol{\eta}_{\mathrm{h}}\right) \boldsymbol{W} \left(\Gamma_{\mathrm{ref}} + \boldsymbol{E}\,\boldsymbol{\eta}_{\mathrm{h}}\right) dr\, d\psi \,, \tag{6.5}$$

where L_{ref} and Γ_{ref} are the lift and circulation of the reference distribution, and $\boldsymbol{D}$ and $\boldsymbol{E}$ are operators relating the harmonic input to lift and circulation, respectively. Also, $\boldsymbol{\eta}_{\mathrm{h}}$ is a vector of harmonic coefficients which contains a sine and cosine coefficient for each flap and swashplate harmonic. For example, given a 2/rev flap input,

$$\eta = \eta_{\mathrm{h}1} \cos 2\psi + \eta_{\mathrm{h}2} \sin 2\psi \,, \tag{6.6}$$

where η is the flap schedule in the azimuthal (*i.e.*, time) domain.

As in the previous optimizations, it is necessary that the helicopter remain in trim, so the net thrust, pitching moment, and rolling moments must be constrained. Also, constraints are placed on the maximum allowable flap deflections, $\eta(\psi) \leq \eta_{\mathrm{max}}(\psi)$. To achieve this, the harmonic coefficients were directly constrained, and this constraint was adjusted until the time domain deflections met their requirements. This constraint is similar to the maximum local lift constraints used to form the constrained optimal rotor solution. The local lift constraint was not explicitly applied in this case, because the exact level where a flapped airfoil should stall is not well defined. Instead,

the maximum flap deflection constraints serve to limit the amount of lift that a flap can add. Also, the flap deflection constraints have physical importance because flap actuators, such as piezoelectrics, have a limited stroke length [37].

Therefore, a cost functional which includes the desired constraints is,

$$\begin{aligned} \Pi_{\mathrm{h}} &= P_{\mathrm{i}} + \nu_T(T - T_{\mathrm{req}}) + \omega_x(M_x - M_{x\,\mathrm{req}}) + \omega_y(M_y - M_{y\,\mathrm{req}}) \\ &\quad + \sum_{i=1}^{N_{\mathrm{h}}} (\eta_{\mathrm{h}i} - \eta_{\mathrm{h}i_{\max}})\, \varpi_i \,, \end{aligned} \tag{6.7}$$

where ϖ_i is a Lagrange multiplier on the flap deflection, and N_{h} is the number of harmonic coefficients. A Lagrange multiplier ϖ_i is zero if $\eta_{\mathrm{h}i} < \eta_{\mathrm{h}i_{\max}}$, for all ψ, and it is greater than zero if $\eta_{\mathrm{h}i} = \eta_{\mathrm{h}i_{\max}}$.

The minimization of the functional in Equation (6.7) could be done using the augmented Lagrangian technique discussed in Chapter 4. However, the number of design variables in this problem is much smaller than the original number of design variables (N). Now the number of design variables is equal to twice the number of flaps times the number of desired flap harmonics plus twice the number of desired swashplate harmonics. The problem is small enough that it can be solved using a quadratic optimization routine in the Matlab [13] computer software package.

It should be noted that this optimization relies on using the influence coefficient matrix, $\boldsymbol{W}$, from a vortex lattice simulation. These coefficients may contain random noise due to the encounter problem (see Section 2.5). Fortunately, in this calculation, the noise should not invalidate the optimization. In Equation (6.7), the design variables are harmonic coefficients, rather than the circulation at points on the disk. If one attempts to optimize the circulation at all points on the rotor disk, the optimization will take advantage of each anomaly in the $\boldsymbol{W}$ matrix. In contrast, when optimizing harmonic coefficients, the lift due to the flap is fitted over the *entire* distribution, not just a single point. Thus, spurious entries in the influence coefficient matrix have much less effect.

6.4 Results from the Aeroelastic Model

A variety of flap arrangements and swashplate inputs were compared to try and characterize their effects on the power production. Not surprisingly, it was found that the more control degrees of freedom available, the more optimal was the new distribution.

Swashplate control with 0, 1, and 2/rev harmonics were tested alone and in combination with servoflap inputs. Harmonic input to the servoflaps was limited to 1, 2, and 3/rev harmonics, in order to stay within the valid operating range of the static aeroelastic model. It was decided to test only two configurations of blades with servoflaps. The first configuration utilized a single, short flap between $0.8875R$ and $0.9125R$. A second configuration had a independent flap in each of the 13 bays available between $0.28R$ and $0.9125R$. No flaps were placed beyond $0.9125R$ for two reasons. First, the lift distribution rolls off at the blade tips so the exact shape of the tip distribution is difficult to model. Real flaps operating close to the blade tips will be strongly affected by three-dimensional effects. Second, the dynamic pressure is higher at the tips than at the root, requiring more energy to deflect the flaps. Actuation devices such as piezoelectrics have a finite energy capacity and will not necessarily be able to fully deflect at typical blade tip velocities.

A list of the significant cases is compiled in Table 6.3. In all of the cases shown here, the maximum flap or swashplate deflection was set to 7 degrees. The relative performance of each of the systems is displayed in the last column. Also shown is the loss factor for the reference case of Chapter 5. As the results indicate, adding additional control authority by increasing the number of actuators improves performance. The best case tested decreased the power required by 4% from the reference case.

Case 3, with one flap and 2/rev swashplate control, will be examined in detail. The swashplate and flap schedules are plotted in Figure 6-1. Surprisingly, the flap schedule is primarily 3/rev rather than 2/rev. The swashplate is predominantly 2/rev in frequency with amplitude modulation provided by the 1/rev input. It is interesting to examine how the swashplate and flap controls are used by the optimization. For

Table 6.3: Performance of the tested rotor systems

case number	Number of flaps	Flap Harmonics	Swashplate Harmonics	Loss Factor κ
ref	0	none	0	1.37
1	1	1,2,3	none	1.36
2	0	none	1,2	1.33
3	1	1,2,3	1,2	1.32
4	13	1,2,3	1,2	1.31

instance, in the half quadrant past 90°, the flap and swashplate controls are working in conjunction to raise the lift over the blade. The flap is pitched up, which causes a nose up moment on the blade; meanwhile, the swashplate command is also nose up. In contrast, in the the 60° region from approximately approximately 260° to 320°, the flap and swashplate issue competing pitch commands to shape the lift on the blade. Specifically, the swashplate issues a pitch-up command to raise the lift. However, the flap deflection causes a nose down pitch, which reduces the swashplate's effect, especially near the blade tip.

The lift distribution due to just the flap and swashplate inputs is plotted in Figure 6-2. Over most of the distribution, the local lift the flap is not distinct from the rest of the blade. It is only visible from approximately 120° to 170° as a slight bowing in the contour. This indicates that the flap is primarily used as a moment (*i.e.*, *twist*) actuator rather than a local lift adjustment device. The flap used in this example is less than 3% of the blade span, which is very small. A larger flap would cause a greater twisting moment for any given deflection. It is likely, therefore, that further performance enhancement could be made with a single flap if the flap were larger than the case tested here. Similarly, Fox [8, Section 5.3] investigated the effect of servoflap size on vibration control. An analytical study found that doubling the flap size near $r = .90R$ resulted in approximately a 60% increase in authority.

Finally, the net lift distribution was obtained by superimposing the lift of the control inputs onto that of the reference case. It is plotted in Figure 6-3. Comparing this to the constrained optimal case in Figure 5-5, it is seen that the controls have

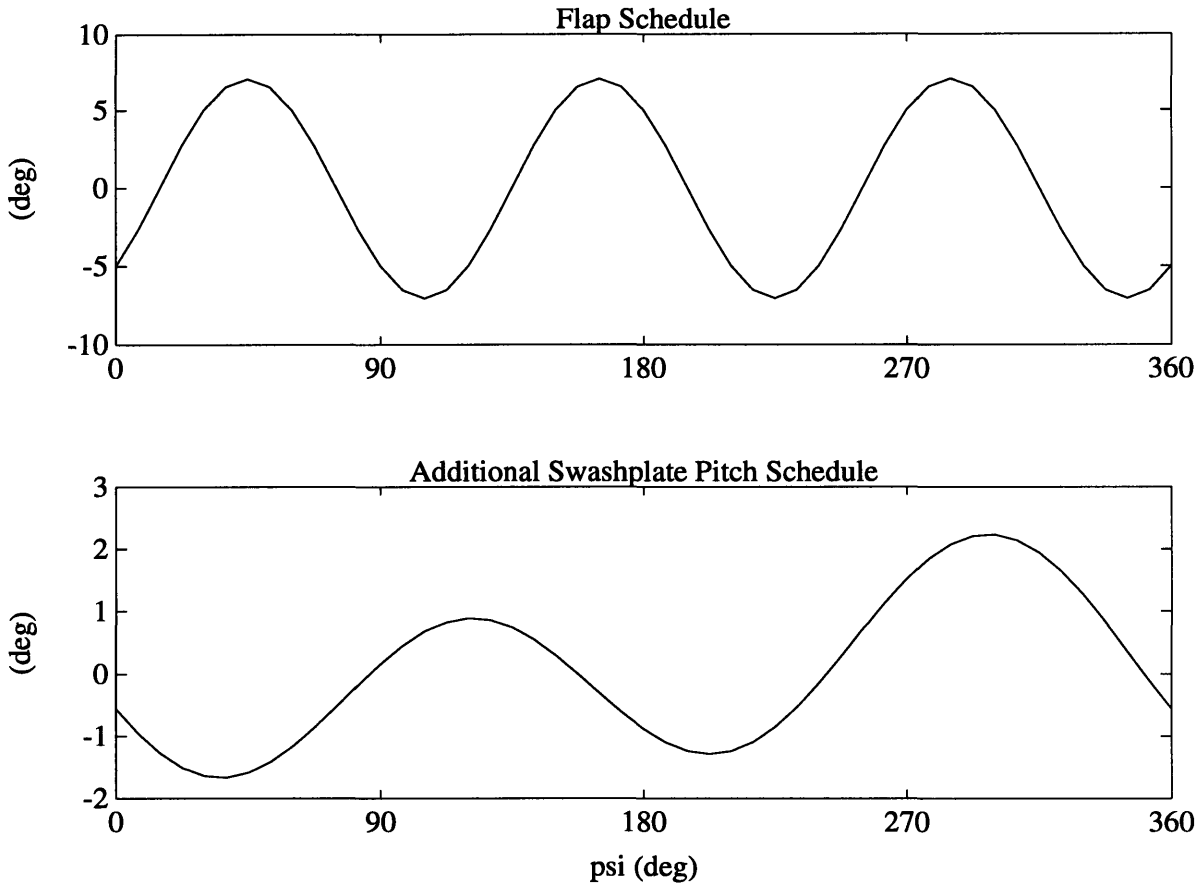

Figure 6-1: Actuation schedules for the swashplate and single flap of case 3, Table 6.3. The flap deflection is positive trailing-edge down, while the swashplate is positive nose up.

pushed the lift towards the optimal distribution, especially near 90° and 270°. However, overall, much of the character of the lift distribution appears unchanged from the original reference case. This indicates that subtle changes in lift profile can have a significant effect (3% decrease) on the power required. The lift distributions for the other flap and swashplate HHC cases have similar appearances.

It is apparent that more control authority is needed to fully achieve the optimal lift distribution of Figure 5-5. The increase in efficiency of a flap and swashplate HHC system over a pure swashplate HHC system is clearly evident by comparing cases 2 and 3. However, both the flap system and swashplate system need harmonic inputs greater than 3/rev to be more effective. To get an indication of how effective an *arbitrary* level of control authority would be for performance improvement, a further test

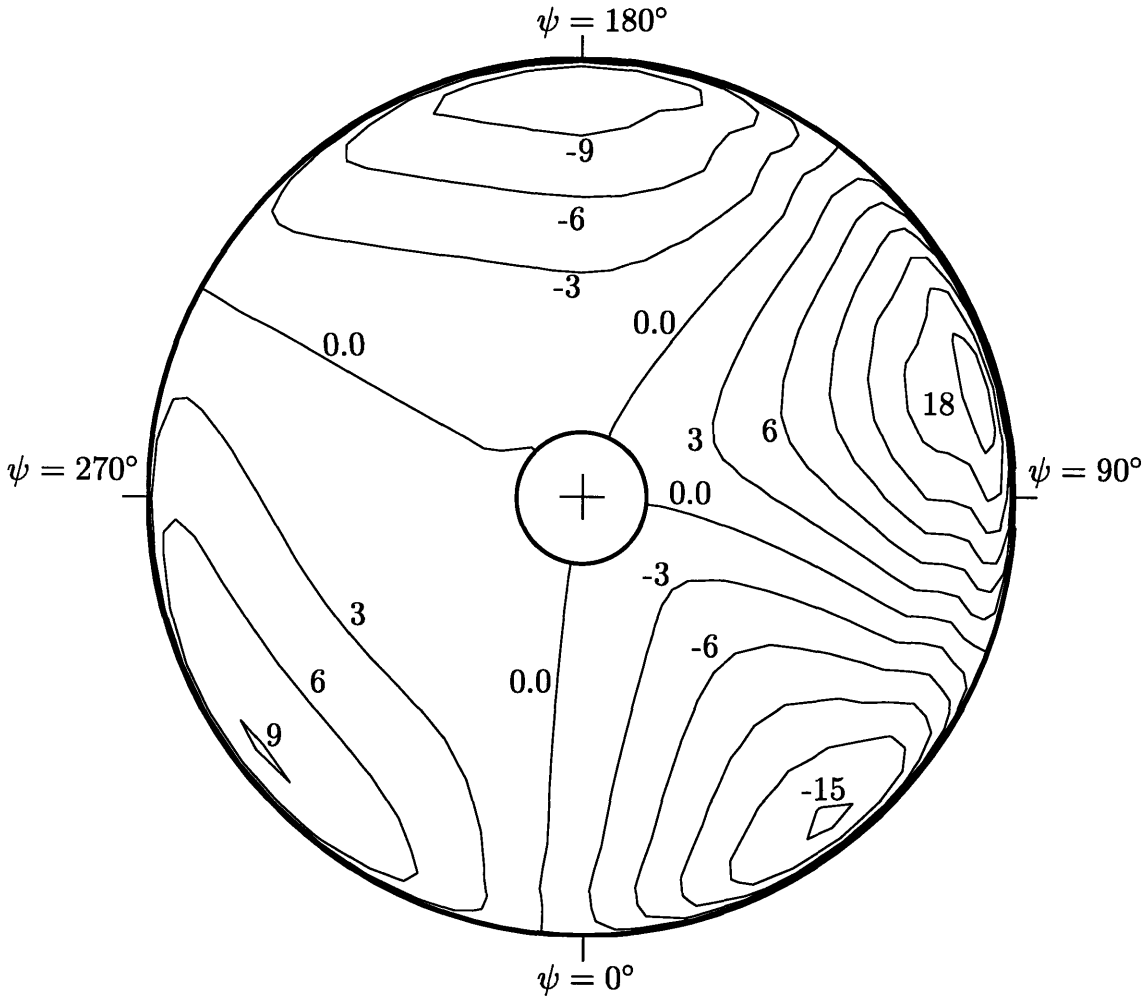

Figure 6-2: Lift from the flap and swashplate of case 3, Table 6.3. $L/(\rho ac(\Omega R)^2)$. Contour intervals are 0.003, labels are $\times 10^3$.

was conducted. A model with 13 non-harmonic flaps and non-harmonic swashplate control was fitted to the *lift* difference between the optimal case with $C_{l_{\max}} = 1.5$ and the reference case. Power was not minimized; instead, only the lift was fitted. The flaps could change position arbitrarily quickly between each discretized azimuthal position. Effectively, this meant that the flaps and swashplate could operate at 24/rev. These high authority lift distributions matched the constrained *optimal* lift distributions very closely. A rough calculation, based on the level of the error in the fit of the lift distribution, indicated that the high authority case would achieve efficiencies 9% better than the reference case. Of course, this test cannot be considered as accurate as the previously discussed cases, since the harmonic content of the controls is too

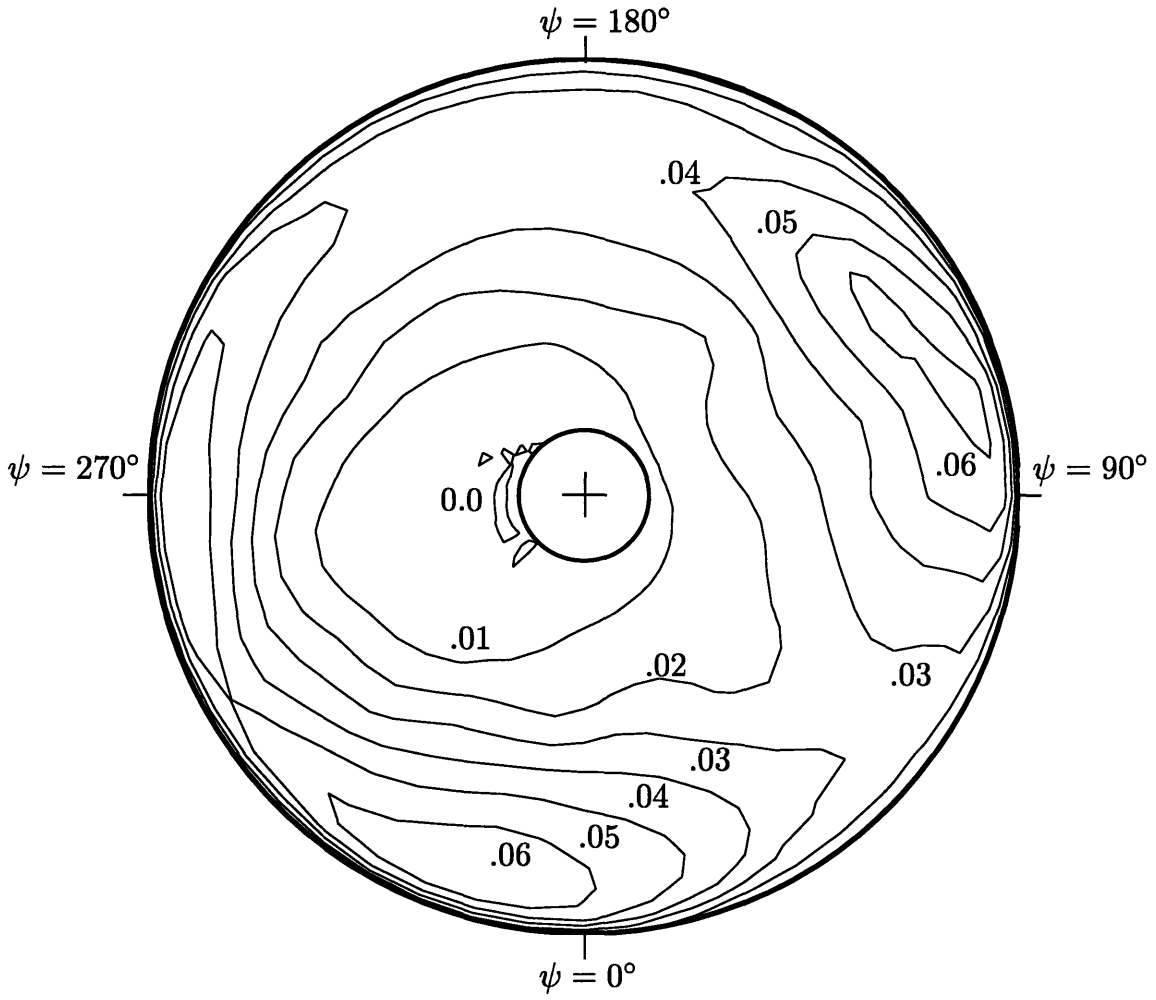

Figure 6-3: Net lift from the reference case modified by the HHC flap and swashplate actuation of case 3, Table 6.3. $L/(\rho ac(\Omega R)^2)$. Flight parameters are listed in Table 5.3.

high to make a static analysis truly valid. However, it does confirm the utility of harmonic inputs with greater than a 3/rev frequency. Even more effective, would be generalized, non-harmonic inputs.

To analyze the effectiveness of generalized, non-harmonic inputs, a dynamic analysis is needed. This could be done with a comprehensive analysis program, such as C60. An impulsive input could be given to the flap at a given azimuth. The resulting lift distribution would then be differenced with a baseline distribution to isolate the effects due to the additional control inputs. This would then be repeated at series of azimuthal locations. Next, the resulting data would be compiled in a flap influence

coefficient matrix, which would give the lift at any location due to a flap deflection at any azimuth. Of course, a separate series of tests would have to be run for the effects of a different sized flap or the effects of a flap at a different radial location. Also, the data would depend on the flight conditions such as the forward speed and the thrust coefficient.

Chapter 7

Conclusions

This chapter begins with a summary of the analysis contained in this document. It also highlights the most significant results. The work completed on the optimal rotor problem should be viewed as a step toward improving the performance of actual helicopters. Therefore, guidelines for further research on helicopter efficiency conclude the chapter. The proposed research makes direct use of the optimal rotor solution.

7.1 Summary and Conclusions

The goal of this research has been to produce forward-flight, helicopter lift distributions which require the minimum induced power loss. This thesis contains the results of this investigation as well as a discussion of the theoretical model used to optimize the lift distributions.

Chapter 2 surveys standard methods used to compute the induced power of a helicopter. Two of the methods, momentum theory and spanwise loading, only estimate the induced power, so they cannot be used to optimize a lift distribution. A third method, here referred to as near wake analysis, yields expressions which exactly compute the induced power. However, the method is numerically unreliable due to its usage of vortex lattice-type downwash models. Therefore, it is also unsuitable for optimization purposes.

A different method must be found to produce the optimal lift distribution. A

procedure is described in Chapter 3 which follows an analysis done by Munro [24]. Strictly speaking, the analysis is restricted to lightly loaded rotors. However, experiments on hovering rotors indicate that the analysis may have a broader applicability. The method examines momentum and kinetic energy in the far wake and relates these to the thrust and induced power of the rotor. The induced power is minimized with respect to variations in the bound circulation, subject to trim requirements on the rotor. It is recognized that this is fundamentally the same technique that can be used to derive the minimum induced loss (m.i.l.) conditions for a fixed wing or a lightly loaded propeller. In all three cases, the energy and momentum must be examined far from the lifting system. Also, the theory leads to a geometric interpretation of the optimal flow in the far wake. In this document, the analysis technique is referred to as *far wake theory.*

Optimization using far wake theory leads to lift distributions which are not physically achievable for a rotor. Real rotors fly through an axisymmetric velocity field and would not be able to generate enough lift on their retreating blade side. The optimization is therefore modified to include constraints on the maximum allowable local lift anywhere on a rotor blade.

This type of optimization is not common in helicopter research. Typical efforts, such as multidisciplinary design optimization (MDO), seek to find the minimum helicopter power for a given set of blade parameters. MDO presupposes that the helicopter must use particular types of hardware. This optimization, using far wake theory, is based solely on the aerodynamics alone. It results in lift distributions which can be used to select the rotor technology which is most appropriate for enhancing performance.

Because of the complex geometry of the far wake, the optimal rotor problem cannot be solved analytically. A numerical solution procedure is described in Chapter 4. The optimization theory uses variational principles, so a finite element method solution is formulated by analyzing the same cost function. The extension of the optimization to include the constraints on the maximum allowable local lift is done using augmented Lagrangians. The procedure was implemented in a computer program known as

CORC, on a CRAY X-MP supercomputer.

The energy in the rotor wake was shown to be concentrated in a narrow, skewed cylinder. For typical forward flight speeds, this cylinder is highly skewed and has the appearance of a flat ribbon, rather than a tube. This energy distribution is difficult to model accurately with a regularly-spaced finite element mesh. For this research, a regularly-spaced mesh is employed, and the skew problem is accounted for by modifying the shape of the finite element domain. However, it could be that the mesh is still overly stiff for a model of this size. In this case, the problem can be solved by using a mesh with an unstructured spacing. Also, it should be noted that energy calculations using the finite element method will always overpredict the true energy in the wake.

The results of the CORC program are presented in Chapter 5. First the program's functionality is validated. Then, the optimization of a typical, forward flight, lift distribution is performed. Optimal solutions are generated for different levels of $C_{l_{\max}}$ and varying numbers of rotor blades. Then, the optimal lift distributions are compared to the lift distribution for a typical, non-optimal helicopter. It is found that:

1. For approximately the same maximum local lift coefficient, the optimal lift distribution is 11% to 16% more efficient than the reference distribution, at $C_T = 0.012$, and $\mu = 0.25$.

2. The optimal lift distributions concentrate lift toward the fore and aft regions of the rotor disk.

3. Constraining the optimal lift distributions to produce realistic lift coefficients causes the blades to achieve the maximum possible lift on the retreating side without stalling.

4. Achieving the optimal lift distribution requires a reduction in shed vorticity, which is manifested as less severe unsteady aerodynamic effects.

5. The efficiency of the optimal lift distributions increases as the level of $C_{l_{\max}}$

increases.

6. The efficiency of the optimal lift distributions increases as the number of blades increases.

It is recognized that producing the optimal lift distribution would require significant radial and azimuthal variations from the reference lift distribution. Chapter 6 examines the capabilities of a smart rotor to achieve the desired lift distribution. The smart rotor is assumed to consist of a swashplate and independently-actuated flaps distributed along the blade. The swashplate and flaps can be actuated at multiples of the blade rotation frequency. A static aeroelastic analysis predicts that a 4% reduction in induced power can be achieved with such a rotor.

In summary, the conditions to achieve the minimum induced losses with a lightly loaded rotor have been described in detail. Minimum induced loss, *i.e.*, optimal, lift distributions are derived by minimizing the induced power with respect to the bound circulation, subject to certain constraints. The procedure is a generalization of the analysis that Betz used to derive the solution for the minimum induced loss propeller. For the rotor, the optimization requires a numerical solution, which is performed here using finite elements and augmented Lagrangians. The optimal rotor lift distributions are between 11% and 16% more efficient than a typical rotor at an advance ratio of 0.25 and a thrust coefficient of 0.012. It appears that a rotor, augmented by multicyclic swashplate inputs and multicyclic servoflap inputs could partially achieve the optimal loading distribution.

7.2 Recommendations for Future Work

Further work on helicopter performance should follow two courses of action. The first course would involve refinement of the optimal rotor model. The second would require further analysis with the model, to be followed by experimental work.

One of the useful qualities of the optimal rotor model is that the optimization procedure can be expanded to include new constraints or physical effects. This merely

requires adding terms to the cost functional, Equation (3.37). For instance, to make the aerodynamics more realistic, a term could be included to account for rotor blade profile drag. Then, the optimization procedure would seek to minimize the combination of induced and profile power.

Profile power can be can be added to the cost functional because linear aerodynamics predicts that the sectional profile drag is proportional to the angle of attack, which is related to the circulation. The incremental profile power is equal to the profile drag dot multiplied with the velocity at the blade section. As was done in Section 2.4, the incremental power can be integrated to yield the average profile power,

$$P_{\mathrm{p}} = \frac{B}{2\pi} \int_0^{2\pi} \int_0^R \boldsymbol{U} \cdot \boldsymbol{D}_{\mathrm{p}} \, dr \, d\psi \,, \tag{7.1}$$

where $\boldsymbol{D}_{\mathrm{p}}$ is the profile drag, and P_{p} is the profile power. Furthermore, it is noted that $a\alpha$ is equal to C_l. This substitution can be made in Equation (3.35) to reveal that

$$\alpha = 2\frac{\Gamma}{Uca} \,. \tag{7.2}$$

The profile drag can be expressed in terms of the angle of attack by

$$D_{\mathrm{p}} = \frac{1}{2} \rho U^2 c \, C_{D_\alpha} \alpha \,, \tag{7.3}$$

where C_{D_α} is the sectional drag curve slope. Finally, substituting Equation (7.2) for α gives the relation between profile drag and the circulation,

$$D_{\mathrm{p}} = \rho U \frac{C_{D_\alpha}}{a} \Gamma \,. \tag{7.4}$$

The profile power is thus a linear function of the bound circulation, which is the design variable in the optimization. Profile drag is a viscous effect, coming from friction at the blade surfaces. As such, the calculation of profile power can only be performed in the near wake and is not considered in far wake theory.

The reader may wonder if other effects, such as wake rollup and contraction could be modeled. These factors have not been considered because they are only present

under heavy loading conditions. There does not seem to be a way to account for these wake distortions with the current analysis technique, because the optimization depends on wake periodicity. However, if the model were simplified to have an infinite number of blades, then it might be possible that *ad hoc* correction factors could be added to account for wake contraction. In other words, drawing the analogy to propellers, the current technique is an exact numerical solution, as is the Goldstein propeller solution. It is hypothesized that the rotor model could be simplified and a new solution derived which is analogous to Betz's original propeller solution. This would still require a numerical solution, because of the geometry of the skewed wake. The new solution could then be modified, as Theodorsen [40] did for Betz's solution, to include correction factors for wake contraction (also see [31], [32], and [45]).

The current analysis could be further enhanced by using an unstructured mesh in the finite element model. As discussed in Section 4.4, the numerical accuracy of the current mesh is limited by the skew problem. An unstructured mesh, using tetrahedral elements instead of hexahedral elements, could concentrate more nodes toward the edges of the wake sheet and the blade tips, thus improving solution accuracy. Within the past two years, commercial mesh generation programs have become available which allow the user to specify the surface mesh and then generate the interior geometry automatically. This would allow the model to retain the advantageous, regular grid over the wake sheet, yet have the accuracy of an unstructured grid.

The second route for future research uses the optimal rotor solution to work on the problem of actual helicopter performance. So far, the optimal rotor solution has been examined at a variety of $C_{l_{\max}}$ levels with a varying number of blades, for a fixed thrust and speed. Also, the possibility of achieving near-optimal performance with a smart rotor was briefly examined in Chapter 6. This investigation can be expanded. Further tests should be run to obtain performance data for the entire flight envelope (by varying μ and C_T). These cases have not been tested yet because reliable data for a typical helicopter's induced power is not readily available. This data is necessary to serve as a baseline performance measure. It is likely that the constrained optimal lift distributions would provide greater performance improvements at certain portions of

the flight envelope than at others. A single flight condition should be chosen where optimal distributions indicate that a large improvement can be made to the induced efficiency. Then, at the chosen flight condition, a series of computer analyses should be run to determine the effects of general, non-harmonic flap and swashplate inputs. As discussed in Chapter 6, this information can be used to generate flap and swashplate schedules to minimize the power.

The validity of such an analysis can only be evaluated in a *rotating* rotor test setup. An effort to develop scale models suitable for testing on rotating stands is currently underway at MIT. The models use piezoelectric-actuated, trailing-edge servoflaps, which can accept both multicyclic and general, non-harmonic control inputs. The design of an experiment to test the smart rotor must consider what, if any, sensing devices should be incorporated to the rotor feedback control system. Real-time flow and pressure data could be used to modify the flap and swashplate schedules as necessary. However, as the results of Chapter 6 demonstrated, the effects of multicyclic control are subtle, so initial control experiments will necessarily be open-loop.

Bibliography

[1] Abbot, I. H. and von Doenhoff, A. E., *Theory of Wing Sections*, Dover, New York, 1959, p. 462.

[2] Adelman, H. M. and Mantay, W. R., "Integrated Multidisciplinary Design Optimization of Rotorcraft," *Journal of Aircraft*, Vol. 28, No. 1, Jan. 1991, pp. 22–28.

[3] Arcidiacono, P. J., "Theoretical Performance of Helicopters Having Second and Higher Harmonic Feathering Control," *Journal of the American Helicopter Society*, Vol. 6, No. 2, April 1961, pp. 8–19.

[4] Bathe, K., *Finite Element Procedures in Engineering Analysis*, Prentice Hall, 1982.

[5] Berry, J. D., "A Multi-Element Vortex Lattice Method for Calculating the Geometry and Effects of a Helicopter Rotor Wake in Forward Flight," AIAA paper 88-0664, AIAA 26th Aerospace Science Meeting, Reno, NV, Jan. 11-14, 1988.

[6] Betz, A., "The Screw Propeller Having the Least Loss of Energy, with an Appendix by L. Prandtl," *Narchrichten der Kgl. Gesellshaft der Wissenschaft*, Math.-phys Class, Göttingen, 1919, p. 193.

[7] Chattopadhyay, A., Walsh, J. L., and Riley, M. F., "Integrated Aerodynamic Load/Dynamic Optimization of Helicopter Rotor Blades," *Journal of Aircraft*, Vol. 28, No. 1, Jan. 1991, pp. 58–65.

[8] Fox, M. E., "Blade Mounted Actuation for Helicopter Rotor Control," Master's thesis, Massachussets Institute of Technology, Dept. of Aeronautics and Astronautics, Cambridge, MA, June 1993.

[9] Glauert, H., "A General Theory of the Autogiro," Aeronautical Research Council, Reports and Memoranda 1377, Great Britain, Nov. 1926.

[10] Glauert, H., "Airplane Propellers," in *Aerodynamic Theory*, Division L, Vol. IV, W. F. Durand, ed., Springer, Berlin, 1935.

[11] Glauert, H., *The Elements of Aerofoil and Airscrew Theory*, Cambridge University Press, second edition, 1947.

[12] Goldstein, S., "On the Vortex Theory of Screw Propellors," *Proceedings of the Royal Society of London*, Vol. 123, Series A, 1929, pp. 440-465.

[13] Grace, A., "Matlab Optimization Toolbox," computer software, MathWorks, Inc., 1990.

[14] Hughes, T., *The Finite Element Method*, Prentice Hall, 1987.

[15] Johnson, W., *Helicopter Theory*, Princeton University Press, 1980.

[16] Kirkpatrick, D. G. and Barnes, D. R., "Development and Evolution of the Circulation Control Rotor," *36th Annual Forum*, American Helicopter Society, Washington, D.C., May 1980.

[17] Krasnov, N. F., *Aerodynamics*, Mir Publishers, 1985.

[18] Kuethe, A. M. and Chow, C., *Foundations of Aerodynamics*, John Wiley and Sons, New York, 1986.

[19] Landgrebe, A. J. and Cheney, M. C., Jr., "Rotor Wakes—Key to Performance Prediction," AGARD CP-111, Marseilles, France, Sept. 13-15, 1972, pp. 1–1 to 1–19.

[20] Larrabee, E. E. and French, S. E., "Minimum Induced Loss Windmills and Propellers," *Journal of Wind Engineering and Industrial Aerodynamics*, Vol. 15, Dec. 1983, pp. 317–327.

[21] Lemnios, A., "Full Scale Wind Tunnel Tests of a Controllable Twist Rotor," *32nd Annual Forum*, American Helicopter Society, Washington, D.C., May 1976.

[22] McCloud, J. L. III, "An Analytical Study of a Multicyclic Controllable Twist Rotor," *31st Annual Forum*, American Helicopter Society, Washington, D.C., May 1975.

[23] Munk, M. M., "The Mimimum Induced Drag of Aerofoils," in *Classical Aerodynamic Theory*, R.T. Jones, ed., NASA Reference Publication 1050, 1979. Originally NACA report no. 121, Munk's dissertation of 1919.

[24] Munro, D., "The Theory of the Lightly Loaded Propeller," unpublished manuscript, 1979.

[25] Nguyen, K. and Chopra, I., "Effects of Higher Harmonic Control on Rotor Performance and Control Loads," *Journal of Aircraft*, Vol. 29, No. 3, May-June 1992, pp. 336–342.

[26] Payne, P. R., "Higher Harmonic Rotor Control," *Aircraft Engineering*, Vol. 30, No. 354, Aug. 1958, pp. 222–226.

[27] Pierre, D. A. and Lowe, M. J., *Mathematical Programming via Augmented Lagrangians*, Addison Wesley, Reading, MA, 1975.

[28] Piziali, R. A. and Du Waldt, F. A., "A Method for Computing Rotary Wing Airload Distributions in Forward Flight," U.S. Army TCREC, TR 62-44, Nov. 1962.

[29] Prandtl, L., "Applications of Modern Hydrodynamics to Aeronautics," in *Classical Aerodynamic Theory*, R.T. Jones, ed., NASA Reference Publication 1050, 1979. Originally NACA report no. 116, translated ca. 1921.

[30] Prouty, R. W., "A Second Approximation to the Induced Drag of a Rotor in Forward Flight," *Journal of the American Helicopter Society*, Vol. 21, No. 3, July 1976, pp. 13–15.

[31] Ribner, H. S. and Foster, S. P. "Ideal Efficiency of Propellers: Theodorsen Revisited," *Journal of Aircraft*, Vol. 27, No. 9, September 1990, pp. 810–819.

[32] Schouten, G., "Theodorsen's Ideal Propeller Performance with Ambient Pressure in the Slipstream," *Journal of Aircraft*, Vol. 30, No. 3, May-June 1993, pp. 417–419.

[33] Scully, M. P., *Computation of Helicopter Rotor Wake Geometry and its Influence on Rotor Harmonic Airloads*, PhD thesis, Massachussets Institute of Technology, Dept. of Aeronautics and Astronautics, Cambridge, MA, 1975.

[34] Seager, M., "The Sparse Linear Algebra Package," computer software, Lawrence Livermore National Laboratory, 1986. Contact email: `netlib@ornl.gov` .

[35] Seddon, J., *Basic Helicopter Aerodynamics*, BSP Professional Books, Oxford, England, 1990.

[36] Shaw, J., Albion, N., Hanker, E. J., Jr., and Teal, R. S., "Higher Harmonic Control: Wind Tunnel Demonstration of Fully Effective Vibratory Hub Force Suppression," *Journal of the American Helicopter Society*, Vol. 34, No. 1, Jan. 1989, pp. 14–25.

[37] Spangler, R. L. and Hall, S. R., "Piezoelectric Actuators for Helicopter Rotor Control," *Proceedings of the 31st Structures, Structural Dynamics and Materials Conference*, Long Beach, CA, April 1990.

[38] Stewart, W., "Second Harmonic Control on the Helicopter Rotor," Aeronautical Research Council, Reports and Memoranda 2997, Great Britain, Aug. 1952.

[39] Tarzanin, F. J., "Prediction of Control Loads Due to Blade Stall," *Journal of the American Helicopter Society*, Vol. 17, No. 2, April 1972, pp. 33–46.

[40] Theodorsen, T., *Theory of Propellers*, McGraw-Hill, 1948.

[41] Tong, P. and Rossettos, J. N., *The Finite Element Method*, MIT Press, 1977.

[42] Weisbrich, A., Perley, R. and Howes, H., "Design Study of a Feedback Control System for the Multicyclic Flap System Rotor (MFS)," NASA CR-151960, 1977.

[43] Wilkerson, J. B., Reader, K. R., and Linck, D. W., "The Application of Circulation Control Aerodynamics to a Helicopter Rotor Model," *Journal of the American Helicopter Society*, Vol. 19, No. 2, April 1974, pp. 2–16.

[44] Wood, E. R., Powers, R. W., Cline, J. H., and Hammond, C. E., "On Developing and Flight Testing a Higher Harmonic Control System," *Journal of the American Helicopter Society*, Vol. 30, No. 1, Jan. 1985, pp. 3–20.

[45] Wu, J. C., Sigman, R. K., and Goorjian, P. M., "Optimum Performance of Hovering Rotors," NASA TM X-62,138, March 1972.